2009

A modular approach to high throughput microsystems

Pin-Chuan Chen
Louisiana State University and Agricultural and Mechanical College, danchuan@gmail.com

A MODULAR APPROACH TO HIGH THROUGHPUT MICROSYSTEMS

A Dissertation
Submitted to the Graduate Faculty of the
Louisiana State University and
Agricultural and Mechanical College
in partial fulfillment of the
requirements for the degree of
Doctor of Philosophy
in
Mechanical Engineering

by
Pin-Chuan Chen
B.S., National Cheng-Kung University, Taiwan, 2000
M.S., Louisiana State University, USA, 2006
May 2009

DEDICATION

To my parents, sister

my loving wife

and

my son, Michael Lucas Chen

ACKNOWLEDGEMENTS

Pursuing a Ph.D. was not my initial plan when I came to United States for my Master degree in Louisiana State University in 2002. The initial plan was to pursue dual Master degrees in engineering and business fields and began my career in industry. But working as a research assistant in campus for two to three years, I found myself like the work and life style of being a professor in a university. So I changed my plan and jumped into the Ph.D. program.

I have to thank many people who helped me achieve this Ph.D. degree in seven years from Master to Ph.D. in LSU. Without their help or guidance either directly or indirectly, I could not image how far my research would have gone until now. Deep appreciation goes to my major advisor, Dr. Michael C. Murphy, in these seven years; his support, guidance, philosophy, and patient deeply help and influence me both in my Ph.D. and my future career I believe. Same credits go to Dr. Dimitris E. Nikitopoulos and Dr. Steven A. Soper, who have supported me through my Master and Ph.D. programs in every aspect. I also want to appreciate Dr. Jin-Woo Choi, Dr. Todd Monroe, and Dr. Sunggook Park for their guidance in their expertise. I also show my gratitude to Dr. Michele Barbato kindly being my committee member.

In seven years, I also have learned a lot from my colleagues including post-docs and students. Dr. Daniel S. Park will the most appreciated person in my Ph.D. and it will be difficult for me to achieve my Ph.D. research plan without his passion, technique skills, and ideas. Dr. Matt Hupert, Dr. Maggie Witek, Dr. Hong Wang, and Miss Edith Chen, from chemistry department gave me detail instructions in this interdepartmental project and helped me find my way to finish chemistry/biochemistry experiment as an engineer. I also want to show my gratitude to my labmates, especially Dr. Byoung-Hee You and Dr. Namwon Kim. Their carefulness and patient as a senior member and a friend really help me through some difficult time during this Ph.D. program. Finally I want to thank those friends from other laboratories for

their kindness to help me finish this multiple-field project.

I also appreciate my close friends who are either studying in LSU or LSU alumui who made my life interesting during these 7 years, otherwise my life will be bored with academic routines. And I also learned a lot from their living and life experiences which helped me become a one who can face the life challenging with mature attitude and see things in different perspectives.

My family deserves the same credits as well. My parents have encouraged me though the entire studying period and I would not be able to achieve my Ph.D. or find the beauty of this world without their open-mind and support. My younger sister does not have any direct support to my Ph.D. either in professional or financial perspective, but I know she is always there when I need her support in any perspective and in any situation. There would not be an enough way to thank my loving wife, Chien-Pu Huang, for staying with me through my Ph.D. after marriage in Jan. 2005. I am lucky to have her appearance, being my life partner, and give me a most wonderful and warmest family. I am also fortunate to have my son's arriving in 2007 with fully satisfaction and pride of being a father. I appreciate the pleasure and atmosphere brought by my son, Michael L. Chen, to let go off my pressure during my Ph.D.

TABLE OF CONTENTS

LIST OF TABLES

LIST OF FIGURES

ABSTRACT

A modular high throughput microsystem was developed using microfabrication technology and nucleic acid analysis. The purpose of developing this microsystem is to identify acute infectious disease and prevent contagious outbreak in a matter of time. This microsystem included three major components, a reagent distribution device, a 96 CFPCR array, and a multi-zone thermal system, to efficiently amplify specific DNA fragments to determine the disease status or precisely pinpoint a disease from multiple patients.

Polymerase chain reaction (PCR) is the key component in the nucleic acid analysis for disease because it can be used to amplify interested DNA fragments by repeatedly thermal cycles. Temperature distribution is critical to the PCR reaction, and thermal management was studied; the approaches which reached good biochemical results were applied to the design of a 96 CFPCR array and a multi-zone thermal system. Protein adsorption is another issue when PCR is realized in a micro device because of the increased surface-to-volume ratio, which might terminate the biochemical reaction. A series of experiments were carried out to understand the protein adsorption in the microchannels with different geometries.

A disposable 96 CFPCR was designed and fabricated on a polycarbonate substrate by double-sided hot embossing and its requirement of multiple temperature zones was fulfilled by building a multi-zone thermal system. Their thermal performance was characterized by numerical simulations and validated by infrared camera experiments. To evenly distribute the analyte with reducing pipetting steps, a reagent distribution device was designed to assemble with the 96 CFPCR array by using passive alignment structures to perform a systematic performance. The passive alignment structures including three pairs of v-groove and hemisphere-tipped post was studied and modified to ensure a smooth passage for mass, momentum, and energy of chemical analyte.

Biochemical experiments demonstrated parallel amplifications of both identical and different DNA fragments from the multiple CFPCRs on the multi-zone thermal system, which implied the potential to detect acute infectious disease with acceleration, accuracy, specificity, and high throughput.

CHAPTER 1: INTRODUCTION

1.1 Motivation for Developing a Modular High Throughput Micro-Analysis System

Infectious diseases have threatened human health for centuries and are one of the top causes of death and disability worldwide [Morens et. Al, 2004]. Although research in medicine, biology, biochemistry, and engineering are exploring new medicines or new detection tools for acute infectious diseases, there are still no promising methodologies to completely eliminate the fear of infectious disease outbreaks. Micro/nano technology has been highlighted and developed as a next generation tool against acute infectious disease since it has the potential to miniaturize all of the equipment in a clinical-laboratory to a hand held device, create new approaches for detection and cure of infectious diseases, and ensures the safety and health of people in a faster, more reliable, and accurate way.

1.1.1 Challenge and Emergency of Infectious Diseases

Infectious diseases have been global killers throughout human history. The Black Death of the fourteen century and the influenza pandemic from 1918 to 1920 each took at least 50 million people [Kohn et al, 1998] [Johnson et al., 2002]. While humans have begun to study and accumulate knowledge about infectious diseases, with contributions from developments in science and technology, infectious diseases also have unfortunately evolved because of the host, antimicrobial resistance, or the environment.

The doctors and medical experts on the front line treating acute infectious diseases have to determine the correct type of pathogen or virus leading to the correct medical treatments based on the patients' symptoms and test results [Poon et al., 2003]. Moreover obtaining the correct information in a timely matter can lead to a decision that prevents an outbreak of an acute infectious disease. The most challenging question for a defense system against acute infectious

disease is the recognition of the pathogens or viruses' species, strains, virulence factors, and antimicrobial susceptibilities in a timely matter [Yang et al., 2004]. The emergency with acute infectious diseases is not only matter of time, but also due to the factor of space. After the industrial revolution, global interactions with any corner of the globe increased due to the development of convenient transportation. The possibility of a global outbreak of an acute infectious disease from a regional source increased and the isolation and rapid detection of infectious diseases became more critical.

Due to the blossoming of the molecular diagnostic approach, researchers have begun using nucleic acid technology for pathogen detection instead of using antibody-based detection. The polymerase chain reaction (PCR) is the fundamental technology in the diagnostic revolution due to its reliability, simple mechanism, sensitivity, and specificity. The power of PCR was successfully demonstrated in detecting several diseases such as *HIV, Chlamydia trachomatis, and M tuberculosis* by DNA sequence matching [Yang et al., 2004]. Normally detection of a single DNA fragment in a disease template is not enough to pinpoint the active status of a virus or a pathogen; parallel monitoring of other DNA fragments in the same template are required. This is the motivation behind developing a multiplex PCR. A parallel approach to monitoring antimicrobial resistance, monitoring the response of the pathogens and viruses to therapy, and quantitative measurement of the pathogen will help doctors make the correct treatment decisions and have more insight into unknown infectious diseases [Louie et al., 2000].

1.1.2 Current Detection Technology for Infectious Diseases

Currently, the most common way to detect an infectious disease relies on culture-based methods. The process is time consuming, usually from 2-3 days up to weeks, and the culturing and characterization of the pathogen bacteria is based on the empirical experience of the doctors

and medical technologists, which has the risk of false test results because of culture conditions. Pathogen samples are often collected from blood or specimens with invasive tools that expose medical technologists to the danger of infection, especially for acute infectious diseases, and make patients uncomfortable. At the same time, appropriate medical treatment may not be delivered to the patients if there is insufficient information. So a widely used, conservative, empirical approach is to start intravenous antibiotic therapy with a broad spectrum of antibiotics. This increases the rate of antimicrobial resistance and may lead to unnecessary hospitalization, increasing costs and demand for medical resources [SE et al., 2003].

Molecular diagnostic technology has developed rapidly for over 20 years and it has been moving from antibody detection in the culture-based approach to direct pathogen detection [Robertson et al., 2005]. Most of the developments are in nucleic acid technology; PCR is the key and fundamental technique. More nucleic acid technology products have been approved by the US Food and Drug Administration (FDA) and accepted for use in infectious disease detection. Those tools can offer speed, accuracy, specificity, reduced cost, and, more importantly, the capability to maintain public health [Robertson et al., 2005]. An example demonstrates the usefulness of molecular diagnostic technology against infectious disease. During the 2003 SARS outbreak, medical researchers tried to pinpoint the correct infectious pathogen and its characteristics in a short time. Different approaches were tried, one of them was nucleic acid technology. RNA was extracted from the samples collected from affected patients and reverse transcription was used to convert the RNAs into DNA fragments followed by a real-time PCR process. The real-time PCR delivered two important pieces of information to determine the status of the patients, one was the correctly amplified fragment converted from the RNA and also the initial concentration of the RNA based on the threshold cycle, the cycle number when amplicons

exceeded a certain concentration during amplification [Poon et al., 2003]. The overall process could be finished in 3-4 hours to pinpoint the genotype of pathogen, which was much faster than the cell culture-based detection which usually took a few days. Using nucleic acid technology can both accelerate the detection process and correctly pinpoint the disease source.

1.1.3 Ideas inside The Human Genome Project

An example of high throughput nucleic acid technology was the Human Genome Project (HGP) which began in 1990 and finished in 2003; the major goals were to identify all of the approximately 20,000 to 25,000 genes in human DNA, determine the sequences of the 3 billion base pairs that make up human DNA, and store the information in a database. All of the steps from the initial sample preparation, PCR amplification, sequencing, mapping, and detection were finished using a high throughput approach based on customizing robots and multiplexed instruments (Figure 1.1 and Figure 1.2), which allowed the Human Genomic Project to be completed two years ahead of schedule [Collins et al., 2003].

Figure 1.1: The automatic and high throughput laboratory for human genomic project [International Human Genome Sequencing Consortium, 2001].

Figure 1.2: The automatic and high throughput laboratory for human genomic project [Kalypsys,10420 Wateridge Circle,San Diego, CA 92121].

Based on the human genome project, a high throughput system would not be restricted to accelerating infectious disease detection, but also may shorten the time required to build a library or a reference database to identify an infectious disease. With the improvement in molecular diagnostic technology, this library can be built using genomic information plus clinical and empirical experience to increase the reliability of the library; accuracy and specificity can be approached in a shorter time compared to the current culture-based detection methodology. To obtain the genomic information for pathogens and viruses, a parallel analysis platform like the customized robots shown in Figure 1.2 should be used to increase the productivity and decrease the required time. Another benefit of using a parallel analysis platform is its cost-effectiveness. In the initial stage of HGP, the cost of a PCR reaction was $125 including the chemical reagents, equipment, dedicated space, personnel training, and labor. This was more expensive than culture-based methods [Louie et al., 2000]. When a well-developed high throughput platform became available in HGP, the cost of PCR was reduced to $9/reaction simply due to automation and a larger-scale platform [Yang et al., 2004].

The completion of the human genome project demonstrated several ideas and possibilities. Using nucleic acid technology in a high throughput approach against infectious disease can significantly reduce the detection time, while increasing the reliability and accuracy. The critical question will be how to miniaturize the high throughput system into a portable platform which can be used anywhere to help people identify the correct pathogen or virus without being limited by the physical environment.

1.1.4 A Microfluidic Point-of-Care System (POC), an Application of Microfluidic Technology

Development of microfluidic devices over the past two decades was boosted by the US Defense Advanced Research Projects Agency (DARPA) in 1990. The main purpose for supporting research in microfluidics was to build the capability for rapid disease diagnostics on the battlefield and help people in poor countries [Yager et al., 2006]. Bio-MEMS is one of the microfluidic technologies and it has several advantages over the conventional benchtop equipment such as lower reagent requirements, faster biochemical reactions on the micro scale, and reduced cost. The most anticipated potential for developing Bio-MEMS-based techniques is to shrink all of the necessary benchtop equipment for disease detection into a small footprint on a single substrate, called a point-of-care microsystem (POC).

> "Point-of-care (POC) testing is defined by the College of American Pathologists as analytical testing performed outside the central laboratory using a device or devices that can be easily transported to the vicinity of the patient" *[College of American Pathologists]*.

The maturation of nucleic acid technology and microfabrication techniques, such as real-time micro-PCR, further pushed the POC test for infectious disease detection closer to realization [Holland et al., 2005] [Janasek et al., 2006].

Figure 1.3 shows an example of a POC system with all of the necessary components to perform disease detection from sample preparation to final sample analysis [Liu et al., 2004]. A well developed POC device can be designed to detect a specific disease and used by the public without any special training. The requirements for a POC system are rapid reactions, simple to use, low cost, easily interpretable output, stable, and disposable [Yager et al., 2006]; those requirements are the directions researchers in the Bio-MEMS field are working toward. POC systems can help doctors and medical technologists identify a specific infectious disease in a short time, followed by the appropriate medical treatment for the patients and correct public health decisions to prevent any outbreak of disease. Once POC devices can be commercialized and approved by the FDA, mass production will make the cost of POC systems affordable and reduce the diagnosis time for patients. In addition, POC devices can also be operated as remote sensors to monitor patients far away from a hospital, and wireless technology can be combined with POCs to deliver the latest status of patients and transfer them to a doctor's office; making home-based care more accurate and affordable, especially for those with diseases or the elderly.

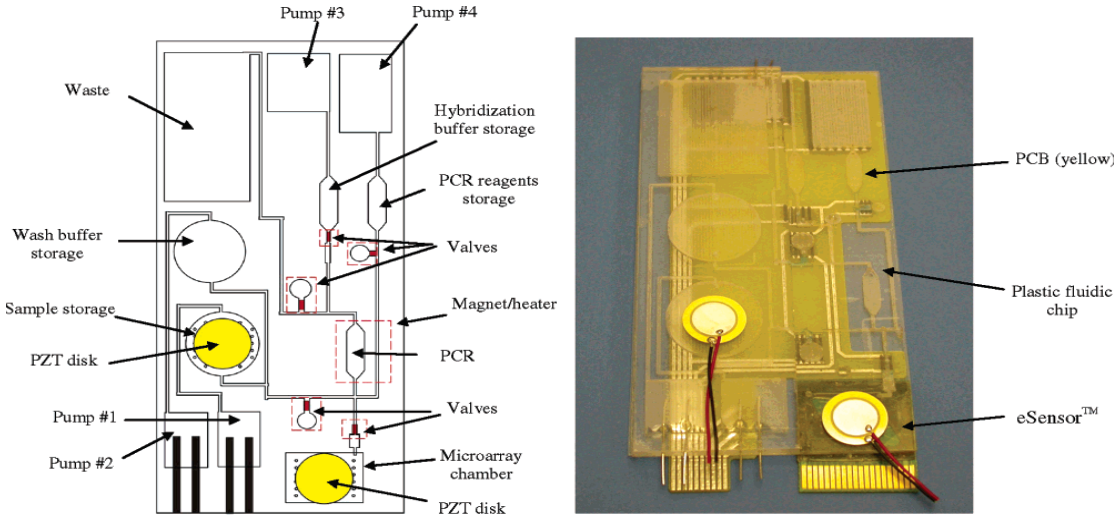

Figure 1.3: An integrated system from sample preparation to analysis [Liu et al., 2004].

POC systems can impact and improve many worldwide health issues. People easily travel around the world using every kind of transportation; this makes the world much closer with constant interaction. Any local infectious disease outbreak is a threat to the world as a result. Rapid and accurate detection is the best method of preventing infectious disease outbreaks. But the available equipment and medical technologists in poor countries are very limited; even fundamental supplies such as power, clean running water, and refrigeration are not good enough to supply a functioning medical laboratory. Figure 1.4 shows a typical laboratory in a mid-level healthcare center in the developing world [Yager et al., 2006]. From a statistical point of view, more than half of the deaths in poor countries and 5% of deaths in the rich countries are due to infectious diseases [Yager et al., 2006]. POC systems can help relieve the shortage of equipment and professional medical technologists since they are designed to be self-operated and powered. But this long term goal of POC medicine still has many challenges to overcome, such as packaging, storage, transportation, and interpretation of results in different regions.

Figure 1.4: Typical laboratories at a mid-level health care center [Yager et al.,2006].

1.1.5 Extension from a POC to a Portable High Throughput Microsystem

A POC device is designed to detect a specific disease with simple operation described in Section 1.1.4. The information obtained from a POC is technically a YES/NO which can be easier for users of all types in developing countries. To correctly indentify an acute infectious

disease and determine the best medical treatment requires parallel testing at different conditions. POC is a typical application of microfabrication technology and has demonstrated the usefulness of a portable microsystem. If the idea of POC can be realized in a high throughput approach, it will perfectly fit in the needs for a pioneering tool for use against infectious disease. Such high throughput microsystem will have all of the functional components in a portable format to pinpoint an infectious disease by parallel analysis of multiple samples in the shortest time possible.

1.2 Polymerase Chain Reaction (PCR), a Fundamental Component in a High Throughput Microsystem

A microsystem includes many components which are used for sample preparation, amplification, and detection, like the example shown in Figure 1.3. The challenge of integrating all of the components into a microfluidic system includes many aspects like the choice of substrate material, the driving mechanism, the development of each functional component, the interface between each component, and thermal design issues. To extend POC microsystems to a high throughput format, the interactions and interfacing between each component will be the most critical challenge.

To layout this portable high throughput microsystem, understanding the basic process for detecting infectious disease is necessary. Figure 1.5 shows the basic procedures for detecting an infectious disease using molecular diagnostics, nucleic acid technology including DNA and RNA detection. Amplification is the necessary step before detection and currently this step is realized mainly by the polymerase chain reaction (PCR), an enzymatic reaction to amplify the target DNA fragments. The advantages of PCR are its simple mechanism, reliability, and accuracy, and it can be realized by well mixing the PCR cocktail and well controlling the required temperatures. So PCR will be chosen as the first development platform toward the goal of a portable high

throughput microsystem and other functional components can be developed from this achievement.

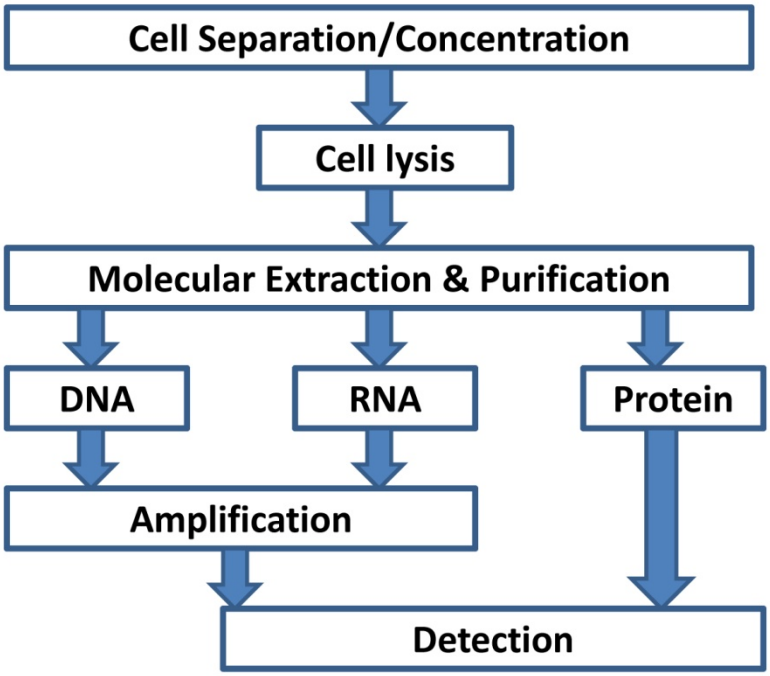

Figure 1.5: The general procedure for molecular diagnostics [Huang et al., 2002]

1.3 Components and Issues in Developing a High Throughput 96 CFPCR Array

A polycarbonate 96 CFPCR array was proposed as a first step toward a high throughput microsystem. Continuous flow polymerase chain reactor (CFPCR) was chosen as a single PCR unit in this high throughput format because it has the potential to significantly reduce the time required for amplification [Hashimoto et al., 2004] and its continuous flow interface is easier to combine with other functional microfluidic devices. To achieve the efficiency of loading samples in this multiple CFPCR array, a reagent delivery device will be designed and stacked on the top of the CFPCR array to evenly distribute the PCR cocktail into every single well. Several issues and approaches are discussed to realize this modular high throughput CFPCR array including microfabrication, thermal management, enzyme loss, passive alignment, and reagent distribution.

1.3.1 A UV-LIGA Mold Insert Approach for Reduced Biochemical Reagent Demand

Using microfabrication technology as a tool to miniaturize the physical size of a high throughput platform will save chemical reagents and costs. LIGA is a German acronym, which stands for LIthographie (lithography), Galvanoformung (electroplating), Abformung (molding); it is a technology based on deep X-Ray lithography, electroplating, and molding processes to fabricate a high aspect ratio microstructures [Madou, 2009]. Following the dimensions of a standard titer plate [SBS, 2004], each CFPCR device was limited in an area of 8 mm ×8 mm and the width of the microchannel was between 20 μm to 40 μm, the gap distance between two microchannels was also between 20 μm to 40 μm depending on the locations. Due to the small dimension of the microchannels, a UV-LIGA microfabrication technology was used to make the mold insert for embossing a polycarbonate 96 CFPCR array.

1.3.2 Enzyme Loss Evaluation in Microchannels

Many biochemical or chemical reactions require catalysis to overcome or lower the reaction energy barrier and initiate the primary reaction, Taq polymerase performs this role for the polymerase chain reaction (PCR). The adsorption of protein was ignored in convectional equipment since the surface-to-volume ratio was not dominant; a regular 200 μl centrifuge tube has a 1.2 $mm^2/\mu l$ surface-to-volume ratio. Once a chemical reactor is fabricated using microfabrication, the surface-to-volume ratio can become much larger, 53.3 $mm^2/\mu l$ in the example of the LSU CFPCR [Hashimoto et al., 2004], and surface phenomena are a factor in such small devices.

Enzyme adsorption is an issue in micro devices on any material substrate and it has been reported for over a decade [Shoffner et al, 1996]. In continuous flow devices, enzyme adsorption is more important due to the very high surface-to-volume ratio, which will play an important role

in the success of the reaction. Previous experimental results showed that enzyme adsorption was not a direct chemical reaction between the enzyme and microchannel surface [Erill et al., 2003] and left the question of enzyme loss in terms of the chance of contact between the enzyme and the microchannel walls. None of the enzyme loss experiments were realized in microchannels even though microfluidic or nanofluidic devices are the main reason to study enzyme adsorption phenomena. Different microchannels with different physical geometries were studied to elucidate the protein adsorption phenomena and mechanism in a laminar flow profile.

1.3.3 Thermal Management from a Micro Thermal Reactor to a High Throughput Microsystem

A Bio-MEMS device could experience coupled fields device such as mechanical, electrical, or thermal based on its application [DeVoe, 2003]. How to deliver the desired thermal performance in a thermal reactor without harming the functions of the other components is a challenge for a microsystem designer.

Thermodynamics and fluid dynamics are two important perspectives in microfluidic devices because they are closely related to the performance of the biochemical/chemical reactions. In a continuous flow thermal reactor, control of the desired temperatures in specific zones is extremely important since it will affect the time and performance of the chemical reactions. Chen studied the effects of temperature to a PCR reaction on a continuous flow platform and concluded that precise temperature control could significantly improve the performance of chemical reaction [Chen et al., 2008]. In a multiple PCR array, the thermal management became more challenging since multiple temperature zones had to be realized in a much smaller area. The thermal management technique in a modular high throughput CFPCR array would be complicated due to the heat transfer was no longer a two dimension problem. A

good design had to be realized to achieve the desired temperature zones at specific locations while avoiding thermal cross-talk and non-uniformity between components.

1.3.4 Passive Alignment Structures for a Modular Approached Microsystem

In a modular high throughput system, modularity gives the flexibility of combining different functional microfluidic devices together, but also increases the complexity of design, fabrication, and assembly. From the stand point of microfluidics, obtaining a smooth flow of a biochemical reagent is a challenge, particularly smooth transport of mass, momentum, and energy from device to device. A numerical simulation was carried out to access the analyte leakage in terms of the mismatch between components. A 13% mismatch of the interconnect diameter gives a significant dead volume of the reagent during transport; this might reduce the accuracy of reagent delivery, increase the chance of cross-contamination, and increase the chance of losing very low concentration of samples like human genomic DNA template or cancer cells [Rani et al., 2006]. Using a passive alignment structure is a convenient and cost effective method to achieve required the alignment between devices in a microfluidic system [You et al., 2006] [Chen et al., 2007].

1.3.5 Reagent Distribution Device

Typical reagent distribution systems are designed for daily use in a benchtop format to reduce the effort of loading, errors and contaminations from operators (Figure 1.6). Current robots and reagent distribution systems are not designed for portability, and high power is required to operate typical reagent distribution equipment. A new reagent distribution device is required for a portable microsystem with low power assumption and a friendly user interface.

The major purpose of the reagent distribution microfluidic device is to deliver the biochemical reagents to each well in a high throughput microfluidic platform. The design criteria

are good alignment from device to device, good thermal management to avoid thermal cross-talk, and the potential to extend from a purely reagent distribution device to a multi- function device.

Figure 1.6: Automatic pipetting workstation from Thermo Scientific Matrix PlateMate [Thermo Scientific, Hudson, NH]

1.4 Outline for The Dissertation

This dissertation describs the initial development of a high throughput microfluidic system in a modular approach including a polycarbonate 96 CFPCR array, a polycarbonate reagent distribution device, and a multi-zone thermal system. Chapter 1 describes the motivation, background, and challenge behind developing a microfluidic system in a modular approach against acute infectious diseases.

Chapter 2 focuses on studying key issues in developing a microfluidic device such as thermal management and enzyme adsorption. The study of thermal management emphasizes the precise temperature control of a polycarbonate CFPCR device and the experiments show discrete and uniform temperature distribution with well designed thermal management features. The experimental results of thermal management on a single microfluidic device were the fundamental technique guiding of the design thermal performance of a polycarbonate 96 CFPCR

array. In the study of enzyme adsorption phenomena, experiments were carried out to understand protein adsorption phenomena in different size of microchannels, which might provide insight to understand the flow behavior of macro molecules in a microchannel.

Chapter 3 to Chapter 5 focus on the development of a high throughput microfluidic system in a modular approach based on the needs and performance described in Chapter 1 and the experimental results described in Chapter 2.

Chapter 3 discusses the development of a polycarbonate 96 CFPCR array, moreover, the thermal and biochemical performance of a single CFPCR is discussed as well. Numerical simulations helped determine the physical dimensions of the cooling features of a CFPCR device to achieve the desired temperature distribution. The simulation is used to understand the temperature distribution of a single CFPCR device or a whole 96 CFPCR array. UV-LIGA fabrication of the mold insert for CFPCR array will be discussed in other publications [Park et al., 2008]. Several biochemical experiments in a single CFPCR device were realized to validate the appropriate design of this nanoliter CFPCR device.

Chapter 4 describes the development of a multi-zone thermal system which is used to support multiple microfluidic thermal reactors simultaneously on a single substrate like a polycarbonate 96 CFPCR array. Eighteen copper strips were used to realize a maximum of 288 steady-state temperature zones, which reduced the required number of real-time thermal controllers and heating units but maintained a flexibility of independent and partial heating locations on a single substrate. Finite element analysis (FEA) and an infrared camera were used to investigate the thermal performance of this multi-zone thermal system. Multiple amplifications of different DNA fragments were realized on either a column device or row device to demonstrate the capability of parallel amplification.

Chapter 5 focuses on the development of a reagent distribution device and the assembly between a reagent distribution device and a 96 CFPCR array. Passive alignment structures are a key component in the assembly and the idea was to use three pairs of hemisphere-tipped posts and V-grooves to create an exactly constrained alignment [You et al., 2006]. A passive alignment structure with a convex annular structure was studied [Chen et al., 2007] to improve the alignment performance demonstrated using the first generation passive alignment structures [You et al., 2006]. This alignment technique was applied to the 96 CFPCR array and the reagent distribution device to have a well aligned path for analyte to transfer from the reagent distribution device to a 96 CFPCR array.

Chapter 6 has conclusions which summarize the major achievements of this research, which included detailed study of a thermal management for a microfluidic device, successful development of a polycarbonate 96 CFPCR array, a multi-zone thermal system to support multiple thermal reactors, a improved passive alignment structure for aligning multiple microfluidic devices, and initial studies of enzyme adsorption in the microchannels and assembly between a 96 CFPCR array and a reagent distribution device. Based on the ultimate goal of a high throughput microfluidic system in a modular approach and the experience during the research training, Chapter 6 also addresses the future works which can upgrade the current microfluidic system and step forward to the ultimate goal.

Two Appendices were listed in the end of this dissertation. Appendix A described the general polymer fabrication process from a micromilled mold insert to a polymer device and Appendix B discusses a modified passive alignment structure which is an opposite case to the modified passive alignment structure described in Chapter 4. The experimental results gave more insight about the design of the passive alignment structures and helped understand the impact of

a convex/concave microstructure on the polymer filling phenomena during the embossing process.

CHAPTER 2: KEY ISSUES IN DEVELOPING A POLYMER-BASED CONTINUOUS FLOW THERMAL REACTOR

2.1 Introduction

A microfluidic thermal reactor is a product of microfabrication technology. Its main advantages are faster reaction times, reduced reagent volume, and a shorter diffusion lengths. The thermal reactor can be part of either a single target point of care system (POC) or a high throughput system.

Microfluidic polymerase chain reactors (PCRs) have been developed over the past decade for amplification of specific DNA fragments by repeatedly realizing three different temperatures and are typical examples of microfluidic thermal reactors. Conventional thermal cyclers for DNA amplification use metal blocks, due to the high thermal conductivity, to maintain a uniform temperature distribution around the DNA cocktail in a centrifuge tube. The different target temperatures are realized by changing the temperature of the block. The disadvantage of the convectional thermal cyclers is the large thermal capacitance of the metal holders resulting in a slow transition temperatures.

A continuous flow polymerase chain reactor (CFPCR) is an alternative idea for repeatedly heating and cooling the PCR cocktail. A microchannel is fabricated on a substrate to contain the DNA cocktail as it is driven through three discrete but uniform temperature zones. The DNA cocktail quickly reaches thermal equilibrium with the three temperature zones when the DNA cocktail passed through the temperature zones. The temperature uniformity in each temperature zone becomes a critical design parameter for either the thermal or the biochemical performance of a continuous flow PCR.

During the development of a micro CFPCR, two primary factors affecting successful amplification of DNA fragments were thermal management and enzyme loss. A thermal

management technique was used to achieve the desired temperature distribution resulting in more successful biochemical performance. Thermal management became more challenging and critical as the microfluidic footprint was reduced, or other functional thermal reactors were located on the same single substrate. A high surface-to-volume ratio was also created in a continuous flow environment because of the long microchannel. This environment also increased the chance of contact and adsorption between proteins and the microchannel walls and reduced the concentration of the active protein in the solution, which might degrade the biochemical performance or even terminate the reaction.

This chapter addresses these two major issues in the continuous flow environment, thermal management of a polymer microfluidic device and protein adsorption in a microchannel. In thermal management, several approaches were studied using simulations and experiments to improve the thermal and biochemical performance of a polymer microfluidic devices. In the study of protein adsorption, several experiments were carried out to understand the mechanism of protein loss in a continuous flow environment, the results should be helpful in designing a microfluidic device.

2.2 Thermal Management of a Thermal Reactor

2.2.1 Thermal Requirements for a Polymerase Chain Reactor (PCR)

Ideally, PCR cocktail must be cycled through three different temperature zones, 90°C - 94°C for denaturation, 50°C - 70°C for renaturation, and 70°C - 75°C for extension (Figure 2.1). In addition, preheating at 94°C and postheating at 72°C are executed to ensure complete denaturation before temperature cycling and complete extension after completion of the thermal cycles [Innis et. al, 1990].

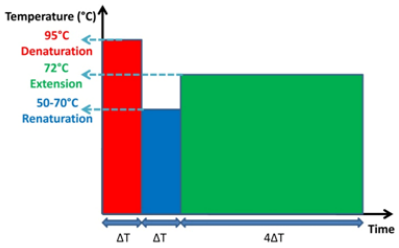

Figure 2.1: Ideal temperature profile for PCR.

Double-stranded DNA templates are separated from double helix structures into two single helix structures during denaturation at 90°C - 94°C. Incomplete denaturation is the most common reason for the failure of amplification and the accepted solution is preheating before the first thermal cycle [Innis et. al, 1990]. The time needed for the denaturation step during thermal cycles is theoretically less than one second [Wittwer et al, 1990]. Too high a temperature or too long a dwell time in denaturation will lead to a loss of enzyme activity.

The second step for DNA amplification after denaturation is renaturation and its required temperature is usually between 50°C and 70°C depending on the design of the primers for specific DNA fragments. At this temperature, the primers attach to the 3' end of the single helix DNA structure. The temperature and time needed for renaturation depend on the composition of the base, target DNA length, and concentration of the primers [Innis et. al, 1990]. Theoretically the duration is less than 1 second, like the denaturation time. [Wittwer, et al, 1990]. Higher renaturation temperatures could increase the precision of specific DNA amplification and decrease the nonspecific amplification and formation of primer-dimer in which forward and reverse primers attach to each other instead of template.

Extension is the last step in DNA amplification to form a complete thermal cycle. Its temperature typically varies from 70°C to 75°C. After the primers attach to the single strand DNA template, the nucleotides, adenine (A), thymine (T), cytosine (C), and guanine (G), in the

DNA cocktail generate a hydrogen bond with the template and begin to extend from the 3' end to the 5' end to form a complete double helix DNA structure. This step takes much longer than the previous two steps and the dwell time in the extension zone depends on the temperature, concentration, and length of the DNA amplicons. Amplification rates can be from 35 to 100 nucleotides/second based on the reaction environment [Innis et. al, 1990]. Longer extension times for early thermal cycles are helpful for complete amplification because more templates are made in the early thermal cycles, resulting in higher amplification rates and greater specificity [Innis et. al, 1990].

2.2.2 The Motivation for Developing Micro PCRs

Conventional benchtop PCR thermal cyclers (Figure 2.2) are commonly used in the biological and medical research because of their reliability. The primary drawback is the cycle time, which is typically on the order of two hours to complete 20 thermal cycles. This can be longer depending on the DNA segment length and the cocktail composition. The cyclers have large thermal capacitances in the supporting stages for the DNA cocktail. As a result, the heating and cooling of these machines is very slow, motivating much of the research on the PCR. By taking advantage of microfabrication technology, the goal is to design a better PCR devices with the same reliability but shorter cycle times. This, in turn, would accelerate the pace of research dependent on thermal cycling technology.

Figure 2.2: Commercial benchtop PCR thermal cycler [Flexigene, Albany, NY]

2.2.3 Continuous Flow Polymerase Chain Reactor (CFPCR)

Micro PCRs can be separated into different groups based on the different substrate materials, drive mechanisms, or heating/cooling mechanisms [Chen, 2006]. One type of micro PCR is a continuous flow reactor which relies on the continuous flow of reagents through three thermostatic zones: denaturation, renaturation and extension. The thermal equilibrium between the analyte and substrate is achieved quickly in a microfluidic device due to the small thermal capacitance of the analyte and high surface-to-volume ratio. This is the principal advantage of continuous flow PCR.

Figure 2.3 shows the footprint of a continuous flow PCR developed in LSU [Mitchell, 2002]. The DNA cocktail was injected into the microchannel and followed the microchannel through three different temperature zones as an alternative way of repeating thermal cycles [Chen, 2006].

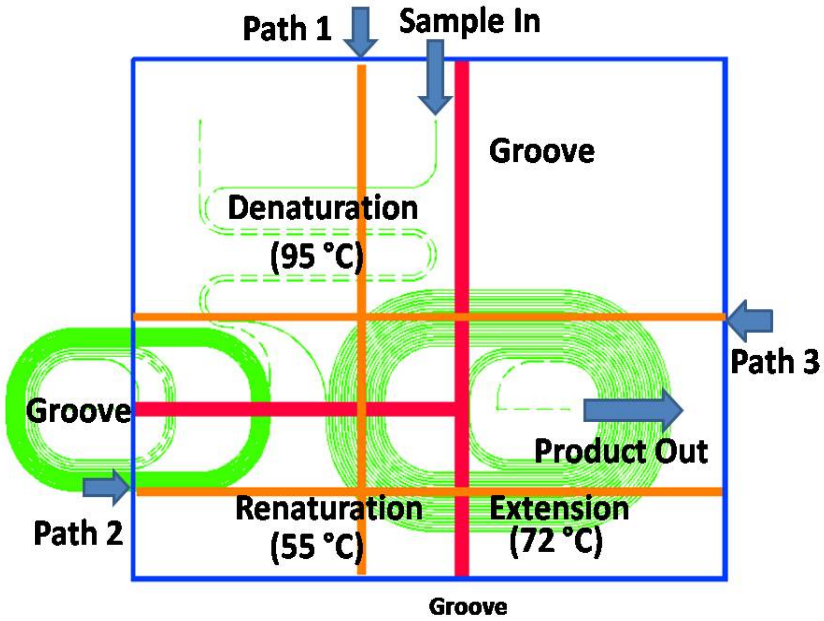

Figure 2.3: The layout of a continuous flow PCR. Grooves were made to separate three different

temperature zones and paths were defined to study the temperature distribution between different temperature zones.

2.2.4 The Motivation for Improving the Thermal Performance of CFPCR Device

Liquid crystal experiments showed that [Chen, et al., 2007b], the temperatures in the continuous flow PCR were not as uniform as assumed. The temperature variation in the renaturation zone was 4°C along a path defined in the liquid crystal experiment image, which might be primarily responsible for the low amplification efficiency of the DNA fragments. The highest amplification efficiency for 500 bp DNA fragments from λ-DNA templates was 25% when compared to a conventional thermal cycler using the same chemical composition [Hashimoto et al., 2004].

To improve the biochemical performance, the temperature distribution of the CFPCR device was carefully investigated. The short-term goal was to use thermal management to achieve three discrete and uniform temperature zones for a single thermal reactor and the long-term goal was to expand these techniques and apply them in either a point-of-care microsystem (POC) or a high throughput microsystem.

2.2.5 Review of Thermal Management Research for Microfluidic Devices

2.2.5.1 Finite Element Numerical Simulation

Numerical simulation is a well developed technology due to the extensive development of the software and computer industries. The dramatically increasing capability for calculations with the decreasing size of transistors allows simulation to be a primary tool in the design stage, decreasing the cost of research and fabrication processes. Many commercial software packages such as ANSYS [www.ansys.com], Intellisuite [www.intellisensesoftware.com], Coventor [www.coventor.com], and CFDRC [www.cfdrc.com] are available and relatively easy to use. The basic process of simulation is to build a solid model, mesh it into finite elements, apply

boundary conditions, and solve. Commercial packages are available for every specific application area and each has limitations.

A finite element numerical simulation package, ANSYS (vers. 9.0, ANSYS, Inc., Canonsburg, PA), was used to examine the temperature distribution in a continuous flow PCR on a glass substrate [Zhang et al., 2002]. Since the thermal conductivity (0.65 W/m K) of the glass substrate was low, achieving temperature uniformity was a challenge. Different thickness micro devices were built to help understand the temperature distribution in the device. Simulation results showed that the temperature distributions in the three temperature zones were discrete and uniform when the microfluidic device was less than 500 μm thick.

ANSYS was used to study the steady-state and transient temperature distributions in a micro chamber PCR device, and to optimize the design for a fast thermal cycling time on a silicon substrate with a Pyrex 7740 glass cover [Lin et al., 2000]. A transient simulation was used to monitor the temperature difference between the commercial heaters and the DNA sample in the microchamber; a 0.07°C difference was reported. A 50 μL 145 bp hepatitis C virus was amplified in the micro chamber PCR with each thermal cycle lasting 20 seconds including 5 seconds for denaturation, 5 seconds for renaturation, 10 seconds for extension. The output was analyzed on a slab gel.

Low-temperature co-fired ceramics (LTCC) were used as substrates for two microfluidic devices, a cyclic PCR device and a DNA detection chip [Sadler et al., 2003]. Thermofluidic simulations using CFDRC were used to optimize the input power, flow velocity, size and position of air gap, and positions of sensors. Different layouts of Ag/Pd micro heaters including serpentine and matrix arrays were simulated to understand which layout of micro heater could deliver the most uniform temperature distribution to the microfluidic device. The same device

was used in another study, where the DNA samples in the cyclic PCR were driven by and through a commercially external peristaltic pump, the flow velocity in the denaturation and renaturation zones was different from the extension zone because of microchannels with different widths. The dwell time in the extension zone was longer than the dwell time in the denaturation and renaturation zones since the extension step required more time. The total volume was 24 μL and each cycle time was 90 seconds at a flow rate of 19.5 μL/min. A 209 bp DNA fragment was amplified in this cyclic PCR [Chou et al., 2002].

A SU-8 micro chamber PCR was reported with platinum heaters and sensors deposited using e-beam evaporation. A 1-D analytical model and a numerical simulation were used to estimate the required power, heating/cooling rates, and the relationship between the cooling rate and substrate thickness. The power required to achieve 94°C was 5.7 W and the average cooling rate was 20°C/s from analytical model. From experiments, the heating rate was 50°C/s. Each thermal cycle was 125 seconds including 5 seconds for transition, 30 seconds for denaturation, 30 seconds for renaturation, and 60 seconds for extension. A 199 bp fragment of yeast ribosomal S3 gene was successfully amplified and analyzed using electrophoresis [El-Ali et al., 2004].

Numerical simulation has been used to understand both the temperature distribution in a micro device, the temperature distribution along a microchannel [Hashimoto et al., 2004], and the effect of grooves on the temperature distribution in a micro device [Yoon et al, 2002] [Yang et al., 2005].

A continuous flow PCR was realized on polycarbonate using LIGA microfabrication. A numerical simulation, ANSYS (vers. 9.0, ANSYS, Inc., Canonsburg, PA), was used to understand the temperature distribution along a microchannel at flow velocities from 2 mm/s to 20 mm/s [Hashimoto et al., 2004]. The dwell time of the DNA at each temperature zone

decreased with increasing flow velocity, which provided a reasonable explanation for lower amplification yields at higher flow velocities. Two different DNA fragments were amplified, 500 bp and 997 bp, and the successful amplification for each DNA fragment was performed in 5.2 seconds/cycles for 500 bp and 9.7 seconds/cycles for 997 bp, which were close to the biochemical reaction limitation.

A simulation package, FLOW3D, was used to analyze temperature distribution of a micro chamber PCR with a reagent volume of 3.6 μL. Parameters studied in the simulation included width, position, and depth of the grooves [Yoon et al., 2002]. A silicon wafer was the substrate material, which made thermal isolation critical in the microfluidic device, to prevent thermal cross-talk from location to location. A substrate with a deeper groove, 280 μm, could reduce the power consumption by 25.6% compared to a substrate without any groove at 95 ºC. The heating/cooling rates also increased with increasing the depth of the grooves because more surfaces were exposed to the ambient environment to dissipate the heat. The heating/cooing rates were 36°C/s/22°C/s. The fastest cycle time in the thermal experiment was 6 seconds/cycle but a cycle time of 2 minutes including 30 seconds for denaturation, 30 seconds for renaturation, and 60 seconds for extension was used to amplify the DNA of interest. A similar approach was realized to study the optimal geometry of a silicon-based micro device by using the finite element method, using ANSYS [Yang et al., 2005]. Different trench geometries were modeled to compare the temperature gradient, power consumption, and heating/cooling rates. A highest temperature gradient, 21ºC/s at a certain point, was obtained using a back etching technique on the silicon substrate to decrease the thermal capacitance. The complicated fabrication process increased the cost, cost of microfabrication increased 56% from $16 to $25, and made this approach, with a deep back etch on the back side, an expensive approach. Two other approaches,

copper conduits and back side dicing were simulated and realized to achieve results similar to back side etching. Different geometries of copper conduits and back side dicing were studied and optimized to estimate the fastest heating/cooling rates.

2.2.5.2 Thermochromic Liquid Crystals

Liquid crystals are used to describe an intermediate phase between solid and liquid. Thermochromic liquid crystals have many useful optical properties because of the variation of orientation order following the local temperature change [Hay et al., 1996]. The reflectivity wavelength of the liquid crystal molecules depends strongly on the local temperature within a certain range and its wavelength decreases with increasing temperature. The color at the lower end of the temperature range is red and the color changes to yellow, green, and blue as the temperature is increased to the high end of the temperature range.

Some groups have used thermochromic liquid crystals to investigate the thermal performance of micro devices [Chaudhari et al., 1998] [Noh et al., 2005] [Iles et al., 2005]. Chaudhari et al. used liquid crystals to examine the temperature distribution on a microchamber PCR on a silicon substrate [Chaudhari et al., 1998]. The temperature of the inside chamber and the temperature distribution over the whole device based on the combination of different clamping methods and a variety of interface materials were investigated. A smaller clamp, with an area of 5.6 mm^2, delivered a more radially symmetric temperature distribution. A 0.2°C non-uniformity across the renaturation zone (55°C) and a 0.4°C nonuniformity in the denaturation zone were achieved with a thermally conductive pad method. Using a larger clamp, with an area of 18.6 mm^2, delivered a relatively larger temperature nonuniformity since it drew a significant fraction of the power from the micro-chamber.

Noh et al. developed a silicon-based micro PCR and liquid crystals were used to investigate the temperature distribution [Noh et al., 2005]. The liquid crystals were injected into the micro chamber, heated by deposited platinum heaters, temperature feedback controlled by platinum sensors, and those raw images were captured by a charge-coupled-device (CCD). The measured temperature variance in the center of the micro-chamber was 1.5±0.5 °C and 3±0.3°C during renaturation and extension, respectively.

2.2.5.3 Infrared Camera

A multiple-chamber PCR device was realized on a soda-lime glass substrate with integrated platinum resistors as heaters/sensing elements [Liao et al., 2005]. The deposited heater and sensor were inside the micro-chamber to heat and measure the temperature of the sample directly. The heating and cooling rates were 10°C/s and 20°C/s, respectively, and a 0.2°C non-uniformity was achieved according to infrared camera measurements. Thirty thermal cycles were realized with a cycle time of 1000 seconds. Each micro chamber contained a 10 μL DNA sample. The experiments focused on five types of upper respiratory tract bacterial genes and the sizes of their corresponding antibiotic-resistant genes were from 273 bp to 1500 bp. Each single device had eight micro chambers and eight target samples could be amplified simultaneously.

Chen et al. used numerical simulation and an infrared camera to study the temperature distribution of a polycarbonate continuous flow PCR [Chen et al., 2008]. The uniform and discrete temperature distribution was achieved in the simulation by using a thinner substrate, micromilling grooves to isolate each temperature zone, and using copper plates as heating stages to supply a uniform temperature input. An infrared camera was used to validate the simulation results. The IR camera images from different layouts demonstrated that a uniform temperature input was a key factor in providing micro device discrete temperature distribution and that

grooves could isolate each temperature zone and decrease the thermal cross-talk. Improving the temperature distribution increased DNA amplification yields 363% at 2 mm/s and 440% at 3 mm/s compared to previous results [Hashimoto et al., 2004].

2.2.5.4 Other Methodologies

A temperature dependent dye, laser grade rhodamine, was used as an indicator for measuring the Joule heating caused by electrokinetically pumping PCR cocktail in a microchannel [Ross et al, 2001]. A relationship between fluorescence intensity and local temperature was used to measure the unknown temperature, and generate a calibration curve. Temperature dependent dye was used instead of thermochromic liquid crystals was due to the concern of the size of the liquid crystal molecules in a small microchannels, 20 μm wide and 30 μm high. The resolution of temperature dependent dye or thermochromic liquid crystals was highly dependent on recording and lighting equipment. A 3.5°C resolution was reported from room temperature to 90°C without any image averaging and this resolution could be improved with better recording equipment.

An interesting in-channel heating/cooling methodology was realized by Guijt [Guijt et al., 2003]. The temperature dependent dye, rhodamine B, was calibrated to measure the temperature in the microchannel. The cooling was realized by bringing acetone and air together from two channels to the cooling region of the microchannels. Each channel was controlled independently to have different ratios of air/acetone and deliver different cooling temperatures. The heating was realized using water and H_2SO_4. The lowest temperature achieved was -3°C at a flow rate ratio 7:1 of air/acetone and the highest temperature was 76°C at a ratio 0.4:1 of water/ H_2SO_4.

Another case of precise temperature control in a microchannel was achieved by using Joule heating [de Mello et al., 2004]. Joule heating of an ionic fluid was generated by applying

voltage across the microchannel to increase the temperature of the solution. A microfluidic device was fabricated on soda lime glass with two parallel microchannels. One microchannel was the platform for an analyte that required heat and the parallel microchannel was used as a heating unit with filling of ionic fluid, BMIM Imide and BMIM PF6. The temperature in the heating microchannel was controlled by measuring the temperature dependent conductivity as a feedback signal. The heat was transferred from the heating microchannel to the analyte microchannel via thermal conduction and the temperature could achieve 90 ºC. The temperature uniformity was ±2°C and could be maintained for at last 10 minutes in the experiment.

2.2.6 Improving the Thermal Performance of a Continuous Flow Polymerase Chain Reactors (CFPCR)

2.2.6.1 Ideas to Improve the Temperature Distribution of A CFPCR Device

The substrate material for the LSU CFPCR was polycarbonate since it had a higher glass transition temperature, 150°C-155°C, which can sustain the denaturation temperature of the PCR process, 94°C. The low thermal conductivity of the polymer material made temperature uniformity an issue in Bio-MEMS applications. On the other hand, its huge potential including low cost, a greater variety of fabrication processes, and more possibilities for surface treatment made it a perfect candidate for mass production of medical devices.

From experimental liquid crystal images [Chen et al., 2007], the lateral heat transfer across the renaturation zone was one of the reasons for a non-uniform temperature distribution. Another factor was the direct attachment of commercial heaters to the polycarbonate device. To overcome the temperature nonuniformity in polymer devices, three ideas were realized in the LSU CFPCR to achieve the thermal requirement for a CFPCR, three discrete and uniform temperature zones. A thinner polycarbonate substrate, making grooves to separate three

temperature zones, and thin copper plates to supply uniform temperature inputs were used (Figure 2.3).

2.2.6.2 Numerically Thermal Simulation for a Macro CFPCR Device

In order to understand the temperature distribution after modifying LSU CFPCR device, thermal numerical simulations were used. Figure 2.4 shows the configuration of the PCR model in a numerical simulation and its boundary conditions. Natural convection was the main cooling mechanism and the convection coefficient was 15 W/m^2 [Incropera, 2002]. The uniform heat flux, representing commercial resistance heaters, was applied under the copper plate and the polycarbonate micro device was mounted on top of the copper plate. The thickness of the copper plate was 2 mm and the micro device was 2 mm. The grooves fabricated by milling were 1 mm wide and 1.2 mm deep from the top surface and 0.8 mm thickness polycarbonate was left along the groove. No microchannel was constructed in this model since the physical dimensions of the microchannel were 200 times smaller than the micro device, which would make the mesh elements exceed the element limitations. Table 2.1 lists the material properties of copper and polycarbonate used in this simulation.

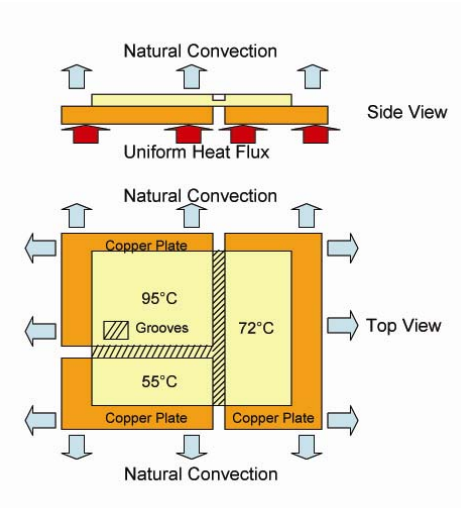

Figure 2.4: The boundary conditions applied for a macro CFPCR device.

Table 2.1: The thermal properties of PC and copper used in the numerical simulations (Incropera, 2001).

	Thermal Conductivity ($W\ m^{-1}K^{-1}$)	Density ($Kg\ m^{-3}$)	Specific Heat ($J\ Kg^{-1}K^{-1}$)
PC	**0.2**	**1200**	**1200**
Copper	**398**	**8940**	**398**

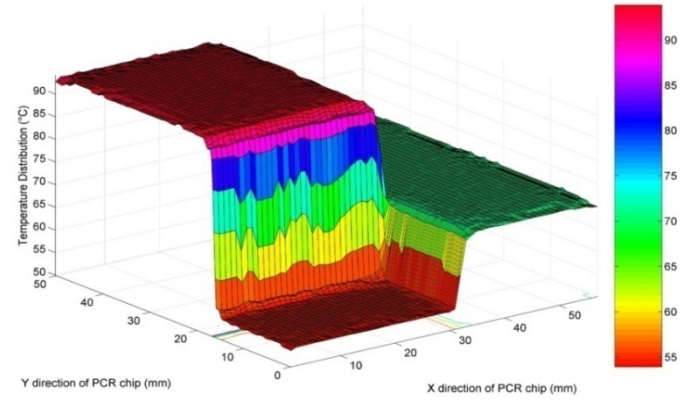

(a)

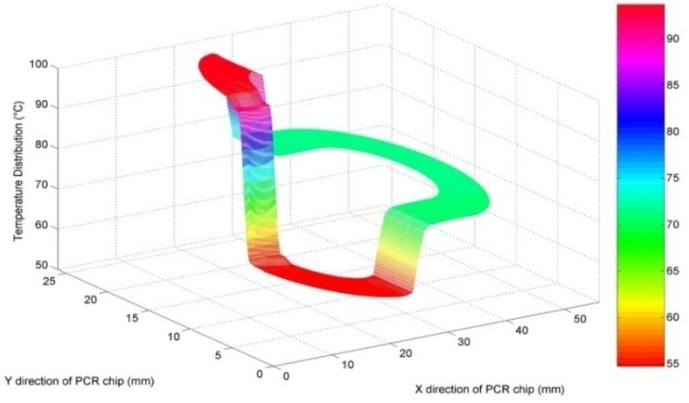

(b)

Figure 2.5: (a) The temperature distribution in the LSU CFPCR device after modification (b) the temperature distribution for 20 microchannels.

Figure 2.5(a) presents the estimated temperature distribution over the whole micro-CFPCR device. Temperature data points along the 20 spiral microchannels were extracted from the macro device simulation data (Figure 2.5(a)) based on their locations, resulting in Figure 2.5(b). The average slope of the temperature profile at the groove between the 95°C and 55°C zones in this simulation was 13.3° C/mm. Without considering convection via microfluidic transport, the reconfigured device provided uniform, discrete temperature zones. The key component was the uniform temperature platform (i.e. copper blocks) that was used instead of either commercial or directly-deposited heaters, which both delivered a uniform heat flux to the polycarbonate surface. A thinner micro-device yielded a lower thermal capacitance and a reduction of the thermal resistance in the vertical direction (z-direction), which decreased the temperature gradient in the z-direction. This made the temperature distribution in the microchannels closer to the temperature distribution of the closed-loop controlled copper plates and heaters. Grooves were used to reduce lateral heat conduction from higher temperature zones to lower temperature ones because the thermal conductivity of air (0.0263 W/ m K) is nearly an order of magnitude smaller than that of polycarbonate (0.2 W/ m K). In addition, the grooves defined distinct thermal capacitances for each zone so that the target temperature could be attained with less input power; faster cooling was also achieved since less power needed to be dissipated. Yoon et al. previously reported numerical simulations and experiments that demonstrated that using a groove could efficiently increase heating and cooling rates (Yoon, et al., 2002).

2.2.6.3 Numerically Thermal and Fluidic Simulation for a Microchannel

To further understand the temperature distribution along the microchannel when considering the thermal conduction and convection of the DNA cocktail, a single microchannel

was modeled. Figure 2.6 shows the modeling and boundary conditions used in this single microchannel simulation. Figure 2.6 (a) shows the thermal boundary conditions and Figure 2.6 (b) the fluidic boundary conditions. The material properties of copper and polycarbonate are listed in Table 2.1 and the water material properties representing the DNA analyte obtained from Incropera [Incropera, 2001].

For thermal boundary conditions, natural convection, 15 W/m^2, was applied on the top surface of the micro device and a uniform heat flux was applied under the copper plates in Figure 2.6 (a); the recess between each temperature zone represented the groove on the backside of the polymer separating each temperature zone. From the macro CFPCR device simulation, the temperature distribution was uniform in each temperature zone, which allowed an assumption of the adiabatic boundary along the Z-direction in single microchannel simulation. The temperature of the DNA cocktail at the inlet was 72°C and ambient temperature was 23°C.

The pressure applied at the inlet was used to change the flow velocity of the DNA cocktail in the microchannel. For different flow velocities, different pressure was applied at the inlet and no pressure was applied on outlet. The non-slip condition was applied on all microchannel walls to generate zero velocity in any direction on the microchannel walls.

Figure 2.7 shows the temperature distribution along the microchannel at flow velocities of 2 mm/s, 4 mm/s, and 6 mm/s. Data for 2 mm/s from previously published results was for comparison before and after the modification of the LSU CFPCR. Table 2.2 lists the average velocity (mm/s), maximum velocity (mm/s), and its corresponding pressure applied in ANSYS (vers. 9.0, ANSYS, Inc., Canonsburg, PA).

In Figure 2.7, the renaturation temperature in the previous publication [Hashimoto, et al., 2004] was 68°C and could not reach 55°C; this was validated using thermochromic liquid

crystals[Chen, 2006]. After modification of the LSU CFPCR device, the temperature distribution could achieve the desired 55 °C and offered a larger temperature range from 55°C to 70°C for renaturation. The temperature curves in the Figure 2.7 shifted and the dwell time of the DNA cocktail at each target temperature band became shorter at higher flow velocity. Figure 2.8 shows the dwell time percentage and transition time percentage at different flow velocities. The dwell time percentage decreased and the transition time percentage increased at higher flow velocities, which was a factor in the reduced amplification efficiency in CFPCR at higher flow velocities [Hashimoto, et al., 2004] since the DNA cocktail had less time to completely finish the reactions at higher flow velocities.

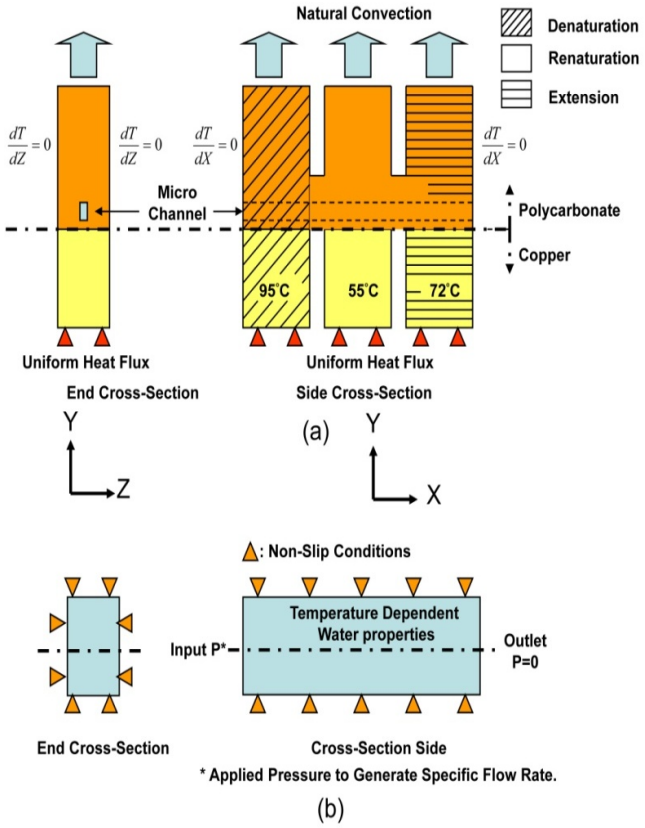

Figure 2.6: The boundary conditions used in the single microchannel simulation (a) thermal boundary conditions (b) fluidic boundary conditions.

Table 2.2: The average velocity, maximum velocity, and applied pressure in single microchannel simulation

Average Velocity (mm/s)	Maximum Velocity (mm/s)	Applied Pressure (Pa)
2	3.7	280
4	7.5	565
6	11.2	845

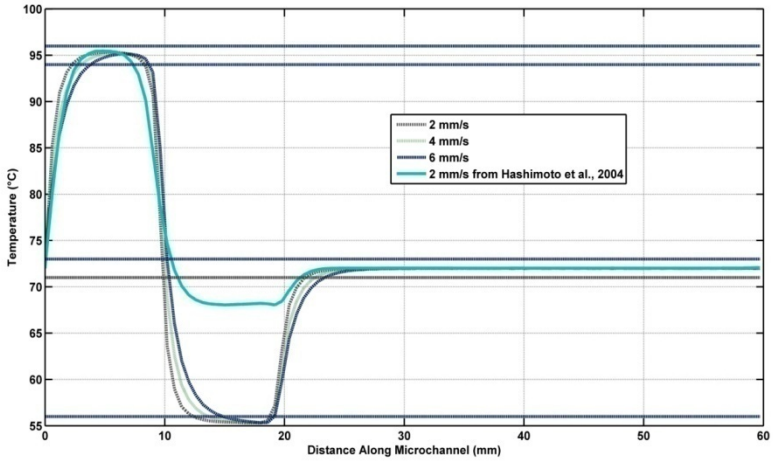

Figure 2.7: The temperature distribution along the microchannel at different flow velocities

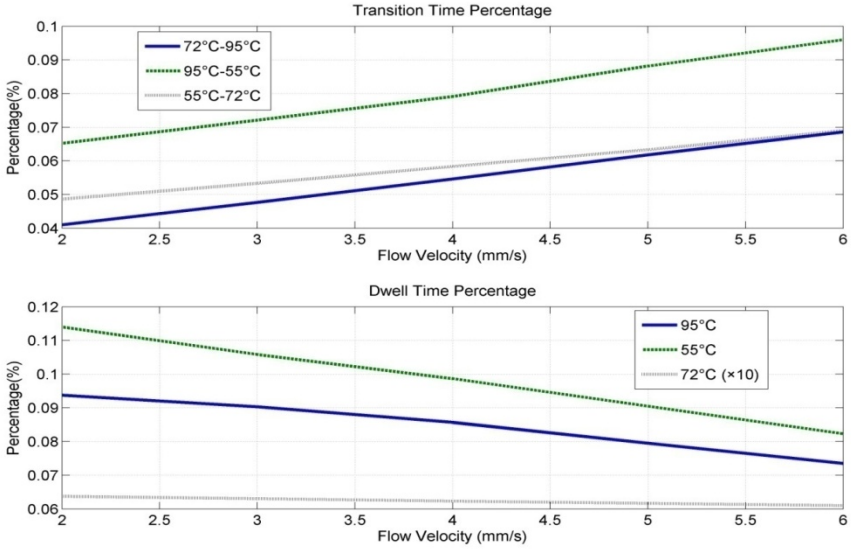

Figure 2.8: The time percentage of dwell and transition at different flow velocities.

2.2.7 Fabrication

A mold insert was within fabricated using LIGA microfabrication technology [Mitchell, 2002] [Desta, 2005]. The hot embossing, drilling, and thermal bonding are described in Appendix A.

2.2.8 Experiments

Two experiments were carried out, one was infrared camera to validate the temperature distribution of the macro CFPCR device and the other one was to assess DNA amplification. The latter was compared with the previously published experimental results to understand the difference before and after the modifications.

2.2.8.1 Experimental Setup

Figure 2.9 (a) shows the modified CFPCR micro device including three temperature zones separated by grooves, an inlet capillary, and an outlet capillary. Figure 2.9 (b) shows the three copper plates which were used to define each temperature zone. The commercial heaters and thermocouples were connected to a power supply and a steady-state temperature controller. They were attached under the copper plates using a thermally conductive double-sided tape. Uniformity of the heaters and durability of the double-side tape were a concern, which could possibly generate a hot spot or affect precise temperature control during the experiments.

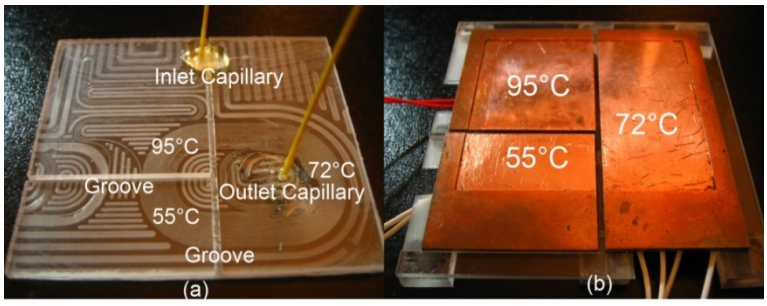

Figure 2.9: (a) The modified CFPCR device including grooves to separate three temperature zones, inlet capillary, and outlet capillary (b) The copper plate heating stage and the heaters were attached under the copper plates

2.2.8.2 The Temperature Validation Using an Infrared Camera

An infrared camera (IR camera) was used to measure the temperature distribution in the modified CFPCR device in order to evaluate the numerical results. The top of the CFPCR chip was sprayed with a thin layer of a special black paint (LCR, Glenview, IL) suitable for thermal investigations. The stable optical properties of the paint at high temperature and its protection against optical reflection and transmission inside the PC substrate were necessary for accurate measurements. An infrared (IR) camera (ThermaCAM® SC3000, FLIR SYSTEMS, Boston, MA) connected to a personal computer was used to monitor the surface temperature distribution of the CFPCR in real-time when power was supplied to the heaters. The system and camera were enclosed in a black box to shield the device from ambient optical and thermal disturbances.

After a steady-state temperature distribution was achieved, IR images of the CFPCR were captured. Matlab (7.0, The MathWorks, Inc., Natick, MA) was used to convert the IR images into thermal contour plots. Three different configurations listed in Table 2.3 were evaluated to understand the effects of each modification on the performance of the CFPCR. In the first case (Case A), only the reduced thermal capacitance of the thinner substrate was used, while neither the copper heating stages nor the grooves were implemented. For Case B, no grooves were included, but the modified heating stages and thinner substrate were retained. In Case C, micro-milled grooves, copper heating stages, and thinner substrate were added and this was the case simulated by a numerical software.

Figure 2.10 shows IR images and thermal contour plots for each configuration. The first case (Case A) had neither the grooves nor the copper plates to supply a uniform temperature and the resulting temperature zones were not discrete. The general pattern of the thermal contours for Case B (Figure 2.10 (B)) and Case C (Figure 2.10 (C)) were very similar; both used the copper

heating stage and the lower thermal capacitance. However, the renaturation (55°C) and extension (72°C) zone temperatures in Case B (Figure 2.10 (B)) were 2-3°C higher than in Case C (Figure 2.10 (C)). Cases B and C were executed under the same experimental conditions except for the addition of the grooves in Case C. The higher temperatures in Figure 2.10 (B) were most likely a result of greater heat transfer from the denaturation zone (95°C) to the other two zones (72°C and 55°C) due to higher thermal conduction through the substrate without the grooves.

Table 2.3: The configurations of infrared camera experiment shown in Figure 2.12.

	Thinner device	Groove	Copper Plates
A	Yes	No	No
B	Yes	No	Yes
C	Yes	Yes	Yes

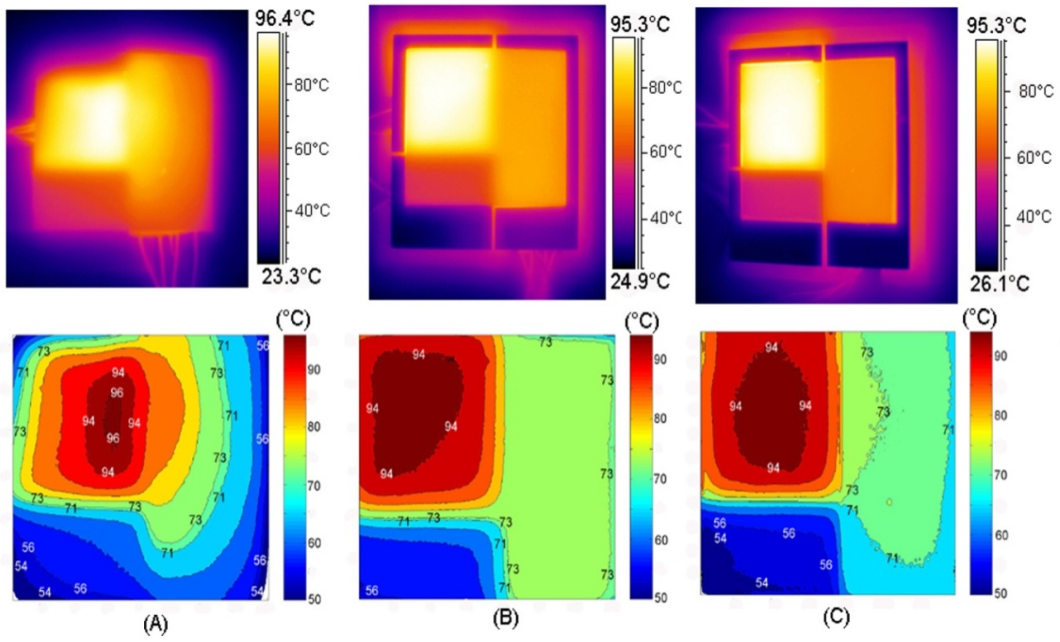

Figure 2.10: The infrared camera images and thermal contours using different setups listed in Table 2.3.

To further understand the temperature uniformity in the CFPCR device, three paths were defined across the transitions from 95°C to 55°C (Path 1), 55°C to 72°C (Path 2), and 72°C to 95°C (Path 3) on the spiral microchannel pattern (see Figure 2.3). The temperature distributions along each path are shown in Figure 2.11. There was a discontinuity, represented as vertical bold lines, in each path (Figure 2.11) at the location of the groove corresponding to a 4 °C/mm temperature gradient across the groove. Most of the paths were at the target temperatures, within a variation of ±1°C, except in the transition areas and close to the edge of the device.

The average cooling gradient across the 95°C to 55°C transition zone extracted from the IR image was less than that estimated using the numerical simulations. The estimated value in the macro CFPCR device simulation was 13.3°C/mm and in the single microchannel model (at 0 mm/s) 12.5 °C/mm, but as measured with the IR camera it was 4°C/mm. The small difference, 0.8 °C/mm, between the two simulation results was reasonable because the macro CFPCR device simulation estimated the temperature distribution in the substrate without considering local effects due to the flow, while the temperature distribution from the single microchannel model accounted for the convection and additional thermal conduction through the cocktail. The observed difference between the simulation results was consistent with, and can be explained by, the effect of convection and the higher thermal conductivity of water relative to PC. The difference increased to 6.36°C/mm at 6 mm/s, supporting the importance of the contribution of fluid convection (13.86×10^{-5} W), because it increased with the flow velocity. The gradient measured between the two zones from the IR image was 70% lower than estimated by the simulations. A transition distance of 4.5 mm was estimated from the simulation for the 95°C/55°C interface, while the actual measured distance on the IR image was about 8 mm. This difference between estimated and measured temperature gradients and thermal transition lengths

may be attributed to several factors. Radiation effects were not included in the simulations because of the added complexity and uncertainties in the radiation boundary conditions. These effects can be significant, especially in the proximity of the grooves dividing the heated zones. Another possible factor is that the natural convection heat transfer coefficient used in the simulations was for a flat horizontal plate and was assumed to be constant. This did not account for the geometry of the grooves separating the heated zones and the variation of the surface temperature. Other possible factors include the unmodeled effect of the adjacent parallel channels, contributions due to three-dimensional geometry, and differences between the parameters used for the simulations and actual values, such as the polymer thermal properties and their variation with temperature.

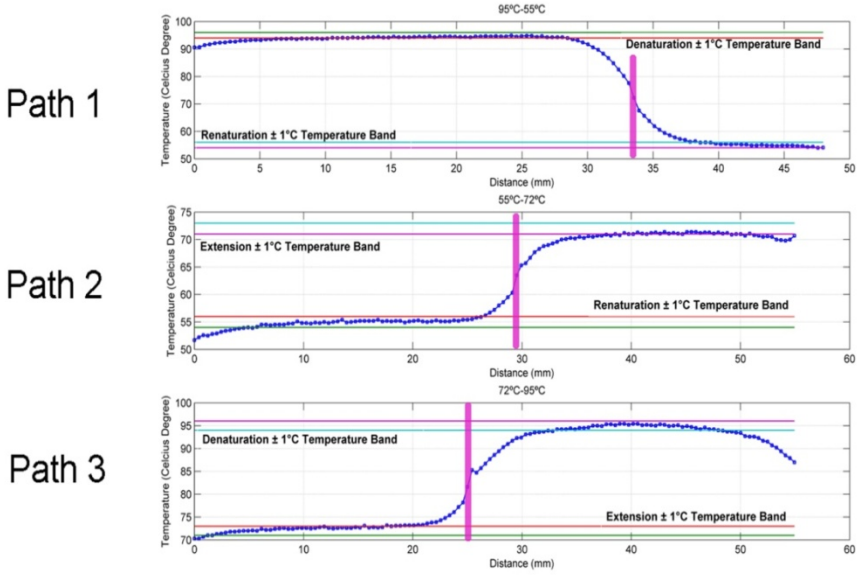

Figure 2.11: The temperature distribution of three paths defined in Figure 2.6.

2.2.8.3 Modified Micro Polymerase Chain Reactor Performance

The purpose of studying the thermal management of a polycarbonate CFPCR device was to improve its affect on biochemical performance of micro PCR. A DNA amplification

experiment followed using the modified CFPCR device. The results were would compared with the previous results to determine whether thermal management was a critical factor in a micro thermal reactor.

The DNA template was a 48 kbp λ-DNA c1857Sam7 (USB, Cleveland, OH) target. Primers were designed to generate a 500 bp DNA amplicon and both primers, forward and reverse, were 25 bp in length. The forward primer was a complement to the negative strand at position 7131-3155 and its sequence was 5'-GATGAGTTCGTGTCCGTACAACTGG-3'. The reverse primer was a complement to the positive strand at position 7606-7630 and its sequence was 5'-GGTTATCGAAATCAGCCACAGCGCC-3' (Integrated DNA Technologies, Coralville, IA). The PCR cocktail contained 10 mM Tris-HCl (PH 8.3), 1.5 mM $MgCl_2$, 50 mM KCl (USB, Cleveland, OH); the concentrations of nucleotides was 200 μM (USB, Cleveland, OH), the template was 10 ng/μL, each forward and reverse primer was 0.2 μM, bovine serum albumin (BSA) was 0.5 μg/μL, and *Taq* DNA Polymerase was 0.07 units/μL (USB, Cleveland, OH). This DNA cocktail was amplified in a bench top thermal cycler to validate the composition and as a reference for the CFPCR results. The cycling conditions were 2 min at 94°C for preheating, 7 min at 72°C for a final extension, and 20 cycles consisting of denaturation for 30 s at 95°C, annealing for 30 s at 95°C, and extension for 40 s at 72°C. The total time needed for this process on the commercial system was about 1.5 h.

The microchannel was washed by pumping deionized water (DI water) through the device for 10 min, followed by a 0.5 μg/μL of BSA and 10X PCR buffer with $MgCl_2$ (USB, Cleveland, OH) for 5 min at 6 mm/s. The DNA cocktail was then injected into the microchannel using a syringe pump (KDS100, kdScientific, Holliston, MA) at four different linear velocities, 2 mm/s (30 s/cycle), 3 mm/s (20 s/cycle), 4 mm/s (15 s/cycle), and 6 mm/s (12 s/cycle). The set

point temperature for the controller in the denaturation zone was 96.7°C, in the renaturation zone 55.7°C, and in the extension zone 73°C, to obtain the desired temperatures. The amplicon was collected from the outlet capillary (Figure 2-11 (a)), mixed with 1X Blue/Orange Dye (Promega, Madison. WI), and injected into an agarose gel (Bio-Rad, Herculus, CA) for electrophoresis. The product was imaged using a Gel Logic 200 Imaging System (Kodak, New Haven, CT) with UV light and each resultant band was evaluated with ImageQuant software (Amersham Biosciences, Piscataway, NJ).

The Case C CFPCR configuration in Figure 2.10 was used for the PCR amplification of bacteriophage λ-DNA. Figure 2.12 (a) represents an agarose gel image of the amplicons generated from a commercial thermal cycler and the CFPCR at different flow velocities. The product from the bench-top thermal cycler was used as a reference to understand the biochemical performance in amplification efficiency at different flow velocities. Figure 2.12 (b) gives the relative intensity of the amplicons compared to the amplicon from the bench-top thermal cycler and previous results obtained using the unmodified CFPCR [Hashimoto, et al., 2004]. The slowest flow rate used in the current study was 2 mm/s, the design flow velocity. The amplification efficiency at that velocity was 72.7% of the bench-top thermal cycler, but in a much shorter processing time, 14.8 min including preheating and post-heating (30 s/cycle) as compared to 4.5 min/cycle. At higher velocities, the amplification efficiency decreased with increasing flow velocity: 44% at 3 mm/s, 29.4% at 4 mm/s, and 20% at 6 mm/s. The amplification efficiency using the modified CFPCR improved by 363% at 2 mm/s and 440% at 3 mm/s compared to the earlier work [Hashimoto, et al., 2004] due to the improved thermal management. Alternatively, according to Figure 2.12 (b), the PCR could be performed three times faster (2 mm/s versus 6 mm/s) at a constant yield of 20% because of the improved thermal

management in applications where the reaction time is the critical measure. The pattern of lower product yields at higher flow velocities matched previous experiments [Hashimoto, et al., 2004] and was most likely due to the shorter dwell times at the set point temperatures, because the design point for the length of the CFPCR channels was 2 mm/s. The lower overall yield of the micro CFPCR compared to the commercial thermal cycler may be due to several factors. In the micro device the *Taq* polymerase has more opportunity to adsorb on the microchannel walls due to the high surface-to-volume ratio of the long channel. Since the PCR cocktail components are flowing at similar flow rates within the microchannel there is also less mixing during the reaction. In contrast, in a commercial thermal cycler, thermal convection recirculation inside a 0.2 mL PCR tube can promote further mixing of the PCR cocktail and increase the chances of the reaction occurring and the smaller surface-to-volume ratio provides less opportunity for nonspecific adsorption of the *Taq* polymerase.

2.2.8.4 Conclusions

A CFPCR device was designed and microfabricated using LIGA technology [Bejat. et al., 2002, Bejat, 2001]. The micro-device was realized in PC because of the advantages of polymers for Bio-MEMS applications [Soper, et al., 2000] [Boone, et al., 2002]. A rapid amplification process was demonstrated in the CFPCR device [Hashimoto, et al., 2004], but the low product yield and the nonuniform temperature distribution [Chen, et al., 2007] motivated a study of the effect of improved thermal management on PCR yields when the micro-device was operated at high processing speeds. Due to the low thermal conductivity of PC, the high temperature gradients in the polymer devices were potentially a limiting factor for performance. Thermal management strategies for the CFPCR were designed using numerical simulations and validated using IR thermography. The experimental and simulation results showed that inclusion of insulating

grooves on the backside of the device, reducing the thermal capacitance, and adding copper heating blocks ensured that the three discrete temperature zones required for PCR were well-defined. The biochemical performance, showed that thermal management considerations were critical in significantly increasing CFPCR efficiency at lower velocities and providing usable output at higher flow velocities (eg. 4 mm/s and 6 mm/s) where no measurable output was obtained in the original design. The experiments also showed that the CFPCR efficiency decreased with increasing velocity while the time per cycle decreased (faster PCR). This was a result of the shortened residence times in each temperature zone and the increased length of the thermal transition zones with increasing velocity, and was predicted by the simple microchannel flow model.

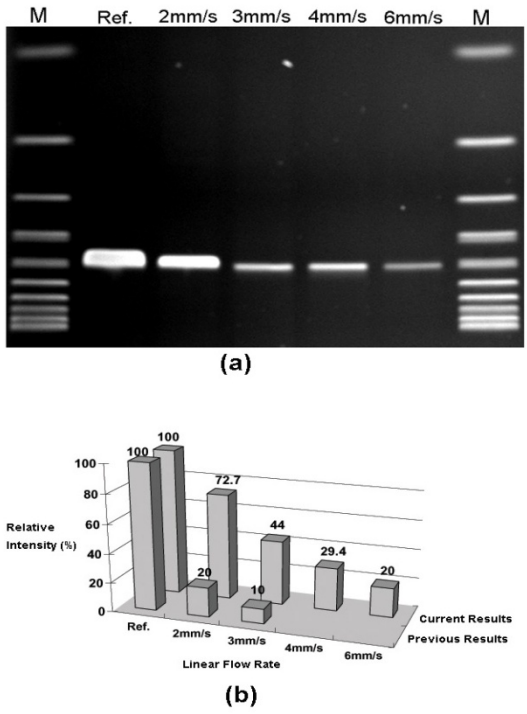

Figure 2.12: (a) Agarose gel image of amplicons from a commercial thermal cycler (reference), and the CFPCR at linear flow velocities of 2 mm/s, 3 mm/s, 4 mm/s, and 6 mm/s. (b) The relative intensity of the amplification efficiency at each flow rate compared to the reference commercial thermal cycler amplicon and the results published by Hashimoto, *et al.* (2004).

2.3 Enzyme Loss Evaluation in Different Microchannel Geometries

2.3.1 Motivation

Microfluidic devices have become a major platform for many biological and biochemical reactions. Using micro scale devices could use fewer reagents, have faster heat transfer and diffusion, use less dangerous chemicals, and cost less due to mass production. When protein-based experiments were realized in microfluidic devices, protein adsorption degraded and even terminated the chemical reactions in these microfluidic platforms due to the increased surface-to-volume ratio. The consequences of protein adsorption included cross-contamination, altered material properties of the substrate surface, and terminated reactions, so understanding the adsorption phenomena in a microfluidic environment is important for the design of microfluidic devices. The continuous flow approach in microfluidic devices has the disadvantage of higher surface-to-volume ratios due to the long microchannels, which may make protein adsorption a dominant factor. To determine this, microchannels with different geometries were used to study the protein adsorption phenomena.

PCR is an enzymatic reaction and the enzyme, a catalyst, is used to help build hydrogen bonds between nucleotides and single strand DNA template in the extension step of every cycle. A lower enzyme concentration might significantly reduce the concentration of amplicons because of insufficient catalyst to help complete a double strand DNA fragment. The enzyme adsorption phenomena was observed in silicon [Shoffner et al., 1996, Taylor et al., 1997, Erill et al., 2003, Krishnan et al., 2004, Wang et al., 2005], glass [Shoffner et al., 1996, Erill et al., 2003], and polymer substrates [Kim et al., 2006, Zhang et al., 2008, Gonzalez et al, 2007]. Each research group used different dummy proteins as precoating agents to reduce enzyme adsorption. A typical polyethylene PCR tube has a 1.5 mm^2/ μL surface-to-volume ratio [Shoffner et al.,

1996], while a microfluidic device has a several-fold increase in the surface-to-volume ratio, like the ratio of 5.33 mm^2/ μL in the LSU-CFPCR [Chen, 2006]. This high surface-to-volume ratio dramatically increases the chance of the enzyme to encounter the microchannel surface, followed by a higher possibility of losing active enzyme from the DNA cocktail. Due to the experience with the LSU-CFPCR, understanding protein adsorption in a continuous flow environment was important for designing future devices and interpreting experimental results.

2.3.2 Reviews of Enzyme Loss Research

Several research groups observed enzyme adsorption in silicon-based microfluidic devices and most of them coated channels with dummy proteins to prevent enzyme adsorption during PCR experiments [Shoffner et al., 1996, Taylor et al., 1997, Erill et al., 2003, Krishnan et al., 2004, Wang et al., 2005]. Bovine serum albumin (BSA) was commonly used as a dummy protein and the methods used to coat the microchannel walls included both dynamic coating and static coating. In dynamic coating, the dummy protein was mixed with the DNA cocktail and injected into the microfluidic device simultaneously to compete with the enzyme for adsorption sites. In static coating, the dummy proteins were injected into the microfluidic device to cover the adsorption sites before injecting the DNA cocktail.

Adding BSA to the PCR cocktail to prevent enzyme adsorption changes the chemical composition; a high concentration of BSA was reported to damage PCR performance [Erill et al., 2003]. A BSA concentration of 2.5 μg/μL in the DNA cocktail was shown to be optimal and would help prevent enzyme adsorption without degrading the PCR performance. To demonstrate PCR performance in a high surface-to-volume environment, PCR cocktail was mixed with powdered silicon or glass and performed in a conventional thermal cycler. The results showed a strong inhibitory of PCR by silicon powder while the glass powder had a relatively small

inhibiting effect. Another experiment was carried out to demonstrate an important relationship between PCR performance and the added enzyme. Adding extra enzyme might not help PCR amplification like addition of unlimited BSA, due to the potential unbalance of the chemical composition in the DNA cocktail. A DNA cocktail with 5-fold more enzyme concentration was prepared to compare with a DNA cocktail having a normal concentration of enzyme and 5 μg/μL BSA. Both DNA cocktails were thermally cycled in a conventional thermal cycler and analyzed. The DNA cocktail with a normal concentration of BSA, 5 μg/μL, showed a better amplification performance. A microchamber type PCR was fabricated on a silicon substrate and successfully amplified a 310 bp DNA fragment in 26.6 seconds/cycle by using the optimal concentrations of enzyme and BSA.

A continuous flow type PDMS-glass device was fabricated and used to amplify a 430 bp DNA fragment [Kim et al., 2006]. Since protein adsorption occurred on the surface of the PDMS microchannels, two steps were used to prevent enzyme adsorption in the PDMS microchannel. The first step used a plasma treatment to convert the hydrophobicity of the surface to hydrophilicity. The second used 2.5% of polyvinylpyrrolidone (PVP) as a dummy protein for dynamic coating. The amplification results showed that the intensity of amplicons with 2.5% of PVP inside the DNA cocktail was almost 4 times stronger than the intensity without adding PVP.

A suprehydrophobic surface was fabricated to prevent enzyme adsorption, which were contributed by several factors including the minimized contact between the solid and liquid, the increased interfacial slip between solid and liquid, and the smaller curvature of the liquid. To understand the protein adsorption phenomena on different surfaces, three kinds of surfaces were investigated including a smooth surface, a surface with microstructures, and a surface with nanostructures. The highest contact angle on micro scale roughness was 152º and for nano scale

roughness was 169º. Three surfaces were exposed to a BSA solution, a model protein used to evaluate protein adsorption phenomena, and measured by a fluorimetric assay as an initial estimate of adsorption. The samples were then exposed to a water flow environment in a water tank to detach the BSA, simulating a microchannel environment for those attached BSA molecules. A second fluorimetric assay was used to obtain a final estimate of adsorption after exposure to flow in the water tank. The initial BSA adsorption before flowing through a water tank on the superhydrophobic surface was similar to a smooth surface, but the residual BSA on a superhydrophobic surface after flowing through a water tank was much lower than that on a smooth surface. The BSA molecules adsorbed on the superhydrophobic surface could be more easily removed. Another interesting result was that the surface with microscale roughness adsorbed more BSA than the smooth surface due to the increased roughness although the micro scale surface had a higher water contact angle [Koc et al., 2008].

Another study used the water contact angle to investigate the adsorption of *Taq* enzyme on different microfluidic materials. The experiment was carried out in a vacuum to prevent droplet evaporation during the 10 minute long experiments. Thirteen microfluidic materials were investigated and categorized into two groups based on the experimental results, propagating adsorption and contained adsorption. The *Taq* droplet on any propagating adsorption material like SU-8, PMMA, and glass totally collapsed within 10 minutes. For example, the SU-8 surface had an initial water contact angle of 60º and the final water contact angle was 10º after 10 minutes. The droplet on contained adsorption materials, like Teflon, had a rapid adsorption saturation. For example the Teflon had an initial water contact angle of 65º and final water contact angle of 60º. In addition to measuring the water contact angle on the different materials, AFM was used to investigate the surface morphologies of the SU-8 and Teflon. The AFM

measurement showed that the Taq enzyme accumulation made the SU-8 roughness 700 nm in height while the Teflon only had several 200 nm pillar-like structures from enzyme adsorption on the surface. Of the thirteen materials, most were propagating adsorption and the enzyme kept spreading over the virgin surfaces [Prakash et al., 2008].

Several microfluidic materials were under investigation for inhibition to the PCR reaction. Those materials included plastic substrate materials like Acrylic, Delrin, Kel-F, PEEK, Polysulfone, and Teflon, and materials for tubing like PEEK, Tefzel, stainless steel, titanium, and Teflon. The materials were statically exposed to DNA cocktail for 5 minutes, then the cocktail was collected, PCR was performed on a conventional thermal cycler, and results compared. Each material including both the substrate and tubing materials were evaluated in four different investigations; first was a 1^{st} run of PCR cocktail, second was a 1^{st} run of PCR cocktail with the addition of PEG 8000, the third was a 2^{nd} run of PCR cocktail, and the fourth was a 2^{nd} run of PCR cocktail with the addition of PEG 8000. The addition of PEG 8000 to either substrate or tubing material increased the amplification intensity. Results from the 2^{nd} runs generally had higher amplification intensity. The reason might be that the PEG 8000 or 1^{st} run of enzyme acted as a dummy protein to saturate the adsorption sites. Metal tubing, like stainless steel or titanium, had very low amplification intensities; so metal tubing might seriously adsorb proteins leading to a significantly degraded amplification result when they were used as tubing [Panaro et al., 2004].

PCR amplification result was studied based on different materials, different exposure length of DNA cocktail, different flow rates, different length-to-volume ratios (LV ratio), and to determine the major reaction component adsorbed to microchannel walls. The materials under investigations were FEP (fluoroethylene-propylene) blue, FEP black, FEP orange, high purity PFA (perfluoralkoxy), PFA natural, PEEK (polyetherketone) orange, and Tefzel (fluoropolymer).

The process included injecting the DNA cocktail through the tubing, collecting the sample from the outlet, amplifying it in a thermal cycler, and comparing the results. Different materials did not show a significant difference when DNA cocktail was injected into the tube at a flow rate of 10 mm/s though 40 cm of tubing. Two different lengths of PFA tubing, 40 cm and 3m, were used to study the DNA amplification in terms of different LV ratio. The results showed that the higher LV ratio, the lower amplification intensity. The amplification results also showed that a larger volume of DNA cocktail, 50 μL, had higher amplification results than a DNA cocktail of 20 μL. The larger reagent volume injected, the more active protein was left in the collected centrifuge tube for the thermal cycler. The flow rates did not significantly change the amplification result and both the enzyme and DNA template substantially adsorbed to the tubing wall, providing low amplification intensities [Gonzalez et al., 2007]. A different conclusion might result at lower flow rates through the tubing, since the adsorbed molecules are large and require a sufficient time to diffuse to the wall and adsorb. Also adsorbed components might be removed from walls due to the large shear forces generated on the boundary between liquid and solid wall at higher flow rates.

The amplification intensity along a microchannel was studied as a function of different surface-to-volume ratios, different surface properties, and different DNA cocktail components. Silicon-glass hybrid microchannels with different cross-sectional areas but the same length, 110 mm, were fabricated. The PCR cocktail was pulled into the microchannel by capillary force and then the entire device was put in a thermal cycler. After amplification, the microchannel was scanned by a fluorescence microscope and the amplification intensity was recorded and plotted along the microchannel. The first conclusion was that the amplification intensity varied along the microchannel because one or several components of the DNA cocktail were adsorbed to the

microchannel walls resulting in a nonuniform distribution along the microchannel. When the microchannel became smaller, with a higher surface-to-volume ratio, the amplification intensity decayed much closer to the loading reservoir, implying that the components in the DNA cocktail had higher chance to be absorbed to the microchannel walls in the smaller microchannels. The concentration of active chemical components was below the critical concentration for successful amplification. The authors assumed that Mg^{+}, an electronic receptor to assist binding between nucleotides and single template in the extension step [Cui et al., 2004], was also an adsorbed target and the experiment validated this point. The Mg^{+} ions were caged by using DM-Nitrophen (DMNP) in the DNA cocktail. After injecting the DNA cocktail into the microchannel it was exposed to UV light to release the Mg^{+} ions, and then thermally cycled. The amplification intensity was detected along the whole microchannel in this caged Mg^{+} experiment, but only partial amplification was detected in the control experiment which used free Mg^{+} in the DNA cocktail. The uncaged Mg^{+} was adsorbed to the hybrid microchannel walls [Krishnan et al., 2004].

2.3.3 The Layouts of Two Mold Inserts

Two layouts were designed to understand the protein adsorption phenomena in microchannels with different geometries. The first layout had eight different length microchannels with the same cross-sectional areas, 200 μm × 60 μm, which used to quantify the protein adsorption in terms of microchannel length (Table 2.4). The second layout had different cross-sectional areas for every microchannel, but the same length, 70 mm. These were used to understand the rate of protein adsorption as a function of cross-sectional area (Table 2.5).

2.3.4 Quantification of Protein Adsorption in The Microchannels with Different Lengths

2.3.4.1 Experimental Protocol

The microfabrication process to produce a polycarbonate microfluidic device for experiment is described in Appendix A. To quantify the amount of protein adsorption in a solution, NanoOrange (N6666, Invitrogen, Carlsbad, CA), a molecular probe, was used. The allowable protein concentration range of this quantification kit was from 10 ng/mL to 10 μg/mL. Its excitation wavelength was 479 nm and emission wavelength was 570 nm. Bovine serum albumin (BSA) was used as the model protein because of its popularity as a dummy protein in microfluidic devices and its low cost.

Table 2.4: The dimensions of 8 microchannels on the first mold insert. Every microchannel had the same cross-sectional area, 200 μm wide × 60 μm deep.

	1	2	3	4	5	6	7	8
Length (mm)	70	210	350	630	910	1190	1610	2030
Contact area (mm^2)	36.4	109.2	182	327.6	473.2	618.8	837.2	1055.6

Table 2.5: The dimensions of the second mold insert. Every microchannel had the same length, 70 mm, but different cross-sectional area.

	1	2	3	4	5	6	7	8
Cross sectional dimension (width (mm) × depth (mm))	20 × 40	50 × 30	50 × 60	50 ×120	200 × 30	200 × 60	200 × 120	200 × 240
Cross sectional area (mm^2)	800	1500	3000	6000	6000	12000	24000	48000

A calibration curve was required to interpret the protein concentration in the solution. Different concentrations of BSA solution were prepared by mixing different volumes of either 10 μg/mL BSA solution (A1 solution) or 1 μg/mL BSA solution (A2 solution) and working solution including fluorescence inside. Table 2.6 lists the different concentrations of BSA solution used to build the calibration curve.

Table 2.6: Different concentration of BSA solution used to build the calibration curve.

ID	Volume of A1* solution (μL)	Volume of working solution (μL)	Final concentration of BSA (μg/mL)
1	0	100	0
2	100	0	10
3	60	40	6
4	30	70	3
5	10	90	1
ID	Volume of A2** solution (μL)	Volume of working solution (μL)	Final concentration of BSA (μg/mL)
6	60	40	0.6
7	30	70	0.3
8	10	90	0.1

* The concentration of A1 was 10 μg/mL; ** The concentration of A2 was 1 μg/mL

Different concentrations of BSA solution were injected into a cuvette and the fluorescence intensity (cps) was measured under a fluoremeter. By knowing the concentration and fluorescence intensity, a calibration curve was generated (Figure 2.13). The maximum concentration of BSA was 10 μg/mL.

The initial concentration of BSA in the experiments was 100 µg/mL and it was injected into the different microchannels listed in Table 2.4. The flow velocity was 1 mm/s and a volume of the initial 20 µL was collected from the outlet of the microchannel for analysis. The 10 µL of collected BSA was mixed with 90 µL of working solution to achieve a final volume of 100 µL in a cuvette for intensity measurement, in which the working solution was made of 4.5 mL nuclease free water (35659230, Integrated DNA Technologies, Coralville, IA), 0.5 mL of NanoOrange protein quantitation diluents, and 10µL of NanoOrange protein quantitation reagent (N-6666, Invitrogen, Carlsbad, CA). The samples were incubated in a thermocycler at 90°C-96°C for 10 minutes followed by 20 minutes at room temperature, protected from light through the process. The fluorescence intensity was maintained for 6 hours without decreasing. The measured fluorescence intensity was interpreted by using the calibration curve in Figure 2.13 to obtain the corresponding BSA concentration for each microchannel.

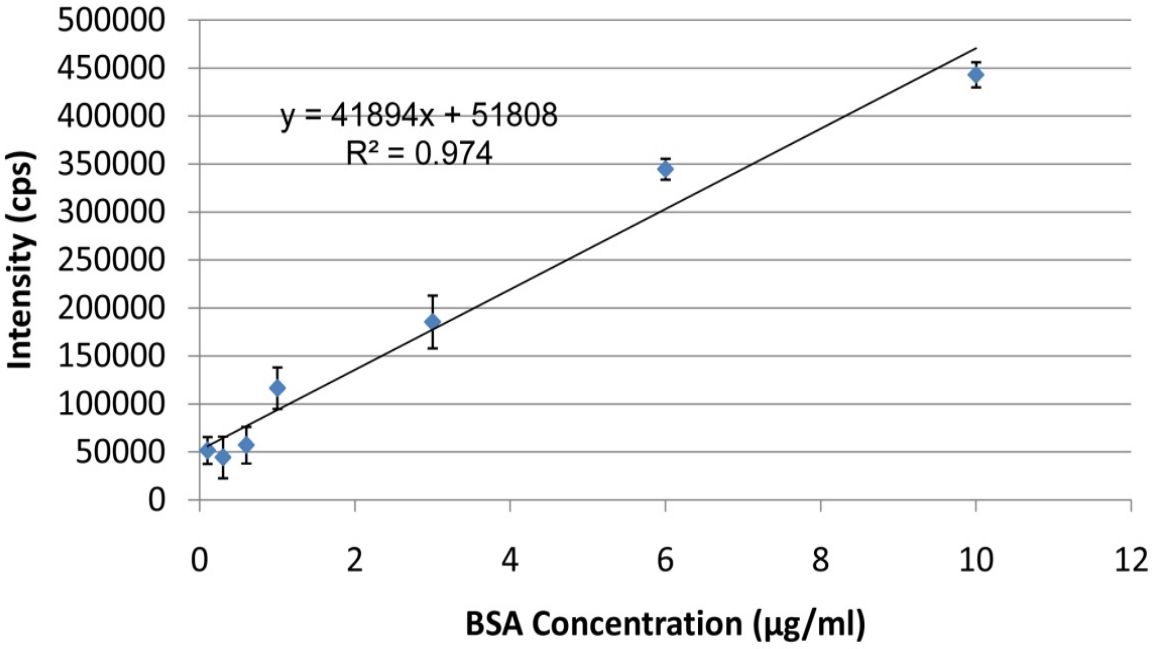

Figure 2.13: The calibration curve for interpreting the BSA concentration from fluorescence intensity in experiment.

2.3.4.2 Experimental Results

Figure 2.14 shows the results of BSA adsorption from microchannels with different lengths. Up to 58% of the injected BSA was lost after flowing through a 2030 mm long microchannel. The adsorption rate of BSA in the entry region was the highest because of the higher concentration of BSA in this region, resulting in a greater chance for BSA molecules to contact the microchannel walls. Figure 2.14 also revealed that the BSA adsorption rate decreased as the length of microchannel increased. The concentration of BSA decreased as the BSA solution flowed further, which reduced the chance of contact between the BSA and the microchannel walls. A possible adsorption phenomena might be implied in the experiment results shown in Figure 2.14. If the slope of the BSA adsorption was always as high as the slope in the entry region, the BSA would be completely exhausted in an approximately 1000 mm long microchannel, which was not true. So the reduced slope of BSA adsorption might contribute to the generally reduced BSA concentration along the microchannel or the laminar flowing profile of BSA molecules in a microchannel if the flowing environment was all the same for every single microchannel.

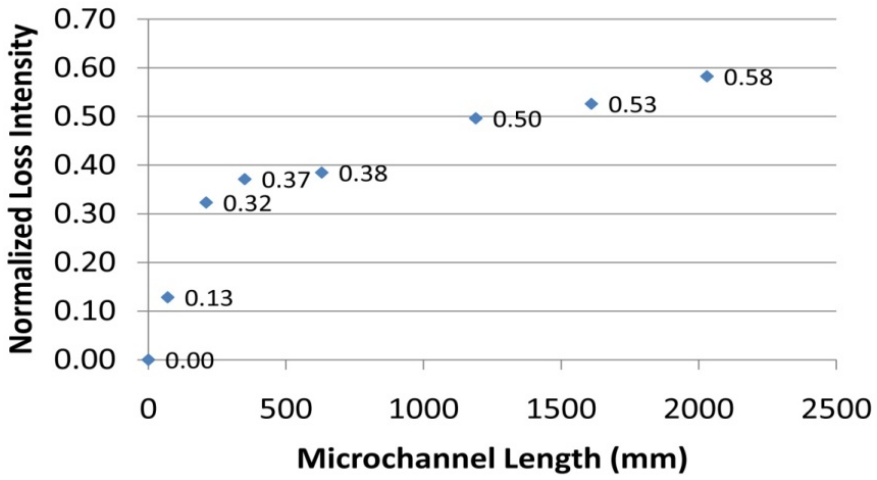

Figure 2.14: BSA loss in different length microchannels.

2.3.5 Protein Loss Phenomena in Microchannels with Different Cross-Sectional Areas

2.3.5.1 Experimental Protocol

Protein adsorption was also investigated in the microchannels with different cross-sectional areas listed in Table 2.5. The microfluidic devices were made on PMMA substrates by using the microfabrication process described in Appendix A. PMMA had better optical properties than polycarbonate, including less background noise, so PMMA was used for the experiments. Two experiments were realized, one using a fluorescence microscope (Zeiss Axiovert 200M Inverted Microscope, Hicksville, NY) to monitor the fluorescence intensity in a microfluidic device which had 5 microchannels. The second one used the microscope to detect the saturation time of BSA adsorption at the end of the microchannels with different cross-sectional areas. The model protein was BSA conjugate (Invitrogen, Carlsbad, CA) whose excitation wavelength was 494 nm and emission wavelength was 520 nm.

In the first experiment, the BSA conjugate was injected into the microfluidic devices with 5 microchannels (Figure 2.15). Figure 2.16 shows the accumulated fluorescence intensity of 5 microchannels recorded in Figure 2.15. Each microchannel had a different accumulation time to reach its saturation point and the slope of the fluorescence intensity accumulation of every single microchannel was different. The accumulation times for microchannels 4 and 5 were longer than those for microchannels 1, 2, and 3 because the concentration of BSA conjugate after flowing through microchannels 1, 2, and 3 was smaller. The saturation intensity of microchannel 5 was the smallest although BSA conjugate was continuously pumped into the microchannel which might imply that the BSA molecules were accumulated as a multilayer in the entry region, the multilayer accumulation of enzyme was observed using an AFM [Prakash et al., 2008]. Combined with the previous results shown in Figure 2.14, which demonstrated that only a

portion of the flowing BSA molecules had a chance to contact the microchannel walls under the laminar flow profile, microchannels 4 and 5 in this experiment would never have the same accumulation intensity as microchannels 1, 2, and 3, until the multilayer accumulation of the previous three microchannels were saturated. In Figure 2.16, microchannels 4 and 5 reached a level intensity plateau than the intensities of the previous three microchannels.

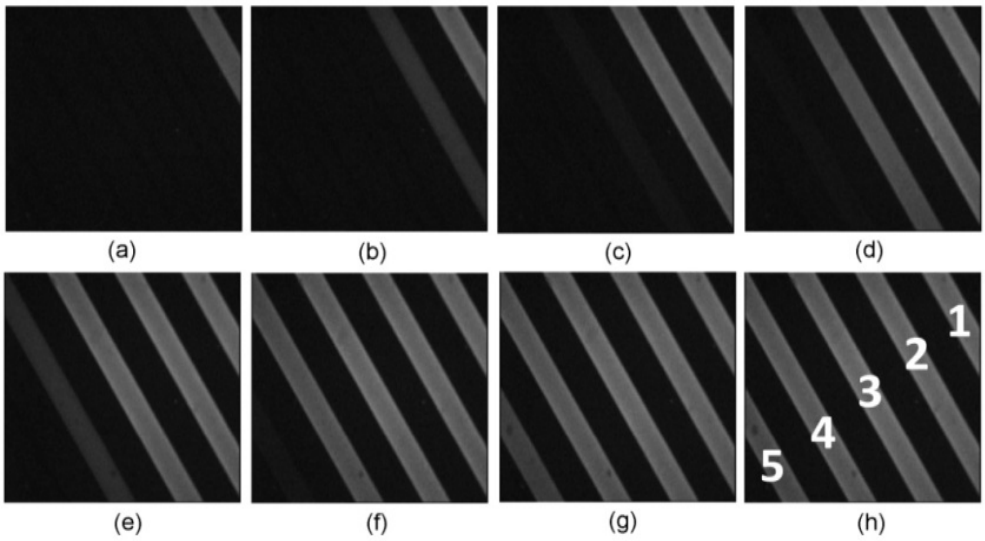

Figure 2.15: The fluorescence images recorded to analyze the fluorescence intensity.

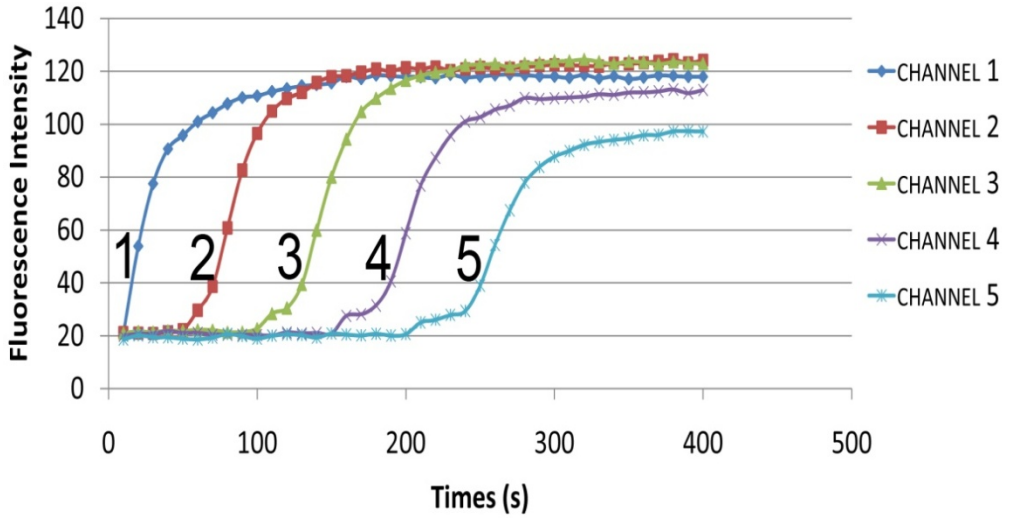

Figure 2.16: The fluorescence intensity for the 5 microchnanels in Figure 2.15

The second experiment used a fluorescence microscope to monitor the saturation time of each microchannel listed in Table 2.6 at the end of each microchannel, 5 mm away from outlet. Figure 2.17 shows the configuration of the experiment. The fluorescence microscope was connected to a computer for recording the fluorescence video and the BSA conjugate was injected into each microchannel by a syringe pump (Harvard Apparatus, Holliston, MA) at 1 mm/s. The BSA conjugate was pumped continuously through the microchannel and into a waste tube via the outlet. The recorded video was stored on a hard disk and analyzed by image processing software (Image J, NIH, Bethesda, Maryland) to estimate the saturation time for each microchannel.

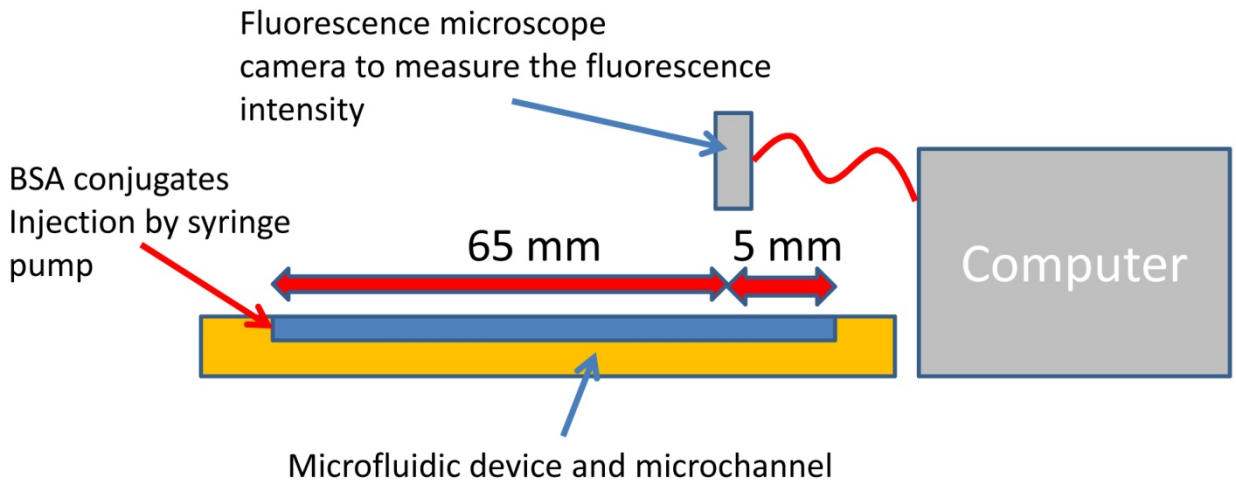

Figure 2.17: The configuration of the experiment for measurement of saturation time of BSA conjugates.

2.3.5.2 Experiment Results

Table 2.7 shows the geometry and the saturation times for each microchannel. The microchannels had the same length, 70 mm, but different cross-sectional areas. Figure 2.18 shows the saturation time of each microchannel corresponding to different volume-to-surface ratios. The saturation time was 60 seconds in a smaller microchannel with a volume-to-surface

ratio of 9.375 and the saturation time was 0.8 seconds in a much larger microchannel with a volume-to-surface ratio of 50. Smaller microchannels required a much longer time to be saturated by BSA conjugate at the end of the microchahnel.

Table 2.7: The geometry characteristics of microchannels used in fluorescence microscope experiment.

	1	2	3	4	5	6	7	8
Microchannel dimensions (μm^2)	20 × 40	50 × 30	50 × 60	50 ×120	200 × 30	200 × 60	200 × 120	200 × 240
Cross-sectional areas (μm^2)	800	1500	3000	6000	6000	12000	24000	48000
Perimeter	120	160	220	340	460	520	640	960
Surface/ Volume	0.15	0.1067	0.0733	0.0567	0.0767	0.0433	0.0267	0.02
Volume/ Surface	6.67	9.375	13.03	17.64	13.04	23.07	37.5	50
Saturation Time (s)	N/A	60	24	3.27	N/A	2	1.2	0.8

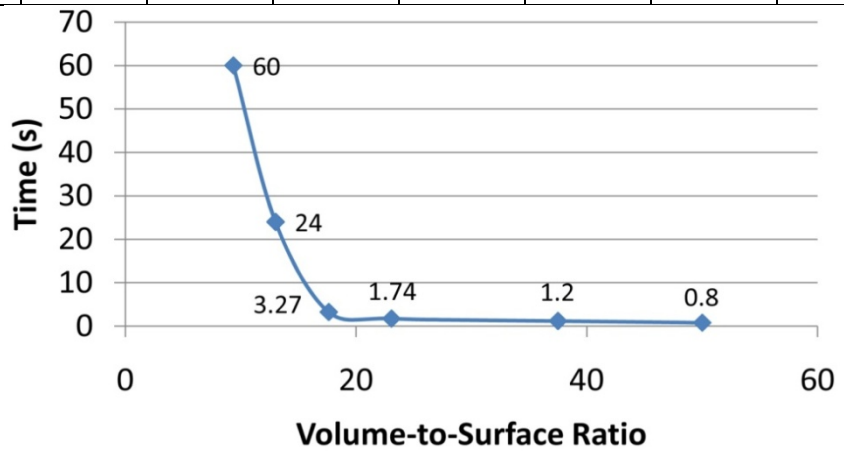

Figure 2.18: The saturation time (s) of different microchannels corresponding to different surface to volume ratios.

2.3.6 Conclusions

The results from both experiments delivered some useful information about protein adsorption. The longer microchannel had larger inner walls which adsorbed more BSA molecules from the solution at different adsorption rates along the microchannel. Only a portion of the BSA molecules had a chance to contact the microchannel walls because of the laminar flow profile for macro molecules in a microchannel. The macro molecules in a microchannel tend to flow in the center of the microchannel, which reduces the chance of encounter with the microchannel walls [Jendrejack et al., 2003]. The experiment also shows that a smaller microchannel took a much longer time to be saturated by BSA conjugates at constant flow velocity of 1 mm/s since it had a smaller volume-to-surface ratio.

The current coating technologies including dynamic or static coatings were used to prevent protein adsorption in a microfluidic device, but the experimental results implied that both coating methods are not very efficient. Both coating technologies were dynamically flowing dummy proteins into microchannels to pre-block or compete with active protein to occupy those adsorption sites, but only a portion of the dummy proteins have the chance to contact the microchannel walls resulting in poor efficiency in coating the microchannel walls especially in a long microchannel. The dummy proteins were not evenly coated on the microchannel walls and most of the protein might be accumulated and layered in the entry region [Prakash et al., 2008]. When the dimension of the microchannel became smaller, the time for dummy protein coating became much longer since the volume/surface ratio became smaller based on two assumptions, the same concentration of dummy protein solution and same adsorption density at the surface. Although the experiment results implied that dynamic or static coating were not efficient, both

still could reduce protein adsorption by reducing the number of binding sites in the microchannels.

CHAPTER 3: A 96 CFPCR ARRAY ON A LARGE AREA MOLD INSERT (LAMI)

3.1 A 96 CFPCR Array for a High Throughput Microsystem

A microsystem to detect acute infectious diseases will include many components from sample preparation, amplification, and detection. The Polymerase chain reaction (PCR) is a key component in molecular diagnosis [Robertson et al., 2005] because of its exponential growth of amplicons, which enabled practical nucleic acid tests in routine laboratories for many applications [Csako, 2006]. In point-of-care (POC) microsystems, PCR is the most common platform in the current nucleotide-based disease detection and other components have to be integrated with PCR to achieve a complete POC microsystem. PCR is selected as the first platform of the high throughput microsystem and other functional devices will be developed from this platform.

3.2 Review of High Throughput Microsystems

High throughput microfluidic devices for different functions have been reported so far including PCR arrays, cell capture, and DNA extraction. This review includes two parts, the first part focuses on high throughput PCR devices and the second part focuses on other high throughput microfluidic devices.

3.2.1 High Throughput PCR Microsystem

Micro PCRs can be separated into two groups based on their approaches, one is microchamber type and another one is continuous flow type. Microchamber type PCR is a miniaturization of the current benchtop PCR using microfabrication and continuous flow type PCR is an alternative method to repeatedly thermal cycling the DNA cocktail. Microchamber type microfluidic devices are the mainstream platform in the high throughput approach since the

design and fabrication are less complicated than the continuous flow approach and the required analyte volume can be less than 1 μL.

A PCR array with picoliter volume was fabricated on a silicon substrate and demonstrated by successful DNA amplification [Nagai et al., 2001]. Different size cavities with volumes ranging from 1.3 pL to 32 μL were designed to examine the minimum volume required for a successful amplification in a microchamber. Fluorescence detection was used off chip to monitor the fluorescence intensity and the results were converted to amplicon concentration. The DNA cocktail was mixed with 0.2 w/v (%) BSA to minimize the enzyme adsorption in the silicon microchambers. A 200 bp DNA fragment was successfully ampLified in a 85 pL microchamber [Nagai et al., 2001]. The silicon micro device was attached under a weight by using double-sided tape so that micro device could be moved between three constant heat blocks repeatedly by manually moving the weight. The dwell time used for the experiment was 5s for denaturation, 5 s for renaturation, and 10 s for extension, resulting in a total time of 18 minutes for 40 cycles with a heating/cooling rate of 16ºC/s.

A multi-chamber thermal cycler was reported [Zou et al., 2002]. This device had 16 silicon heating components, 4 × 4, mounted on a printed circuit board (PCB board) by flip chip bonding to make 16 individual heating islands. The microchamber PCR array was mounted on the heating islands for repeated thermal cycles. The temperature sensors and heaters were aluminum, vapor-deposited on the PCB board and connected to thermal PID controllers. From the deposited sensors, the heating and cooling rates were 34-50 ºC/s and 23-31ºC/s. The thermal cross-talk between each heating island or microchamber was minimized by the low thermal conductivity of the PCB board and plastic microchamber device. The temperature distribution in the microchamber was studied using finite element analysis. A 320 bp DNA fragment was

successfully amplified in 15 minutes for 30 cycles with a 20 μL DNA cocktail. A similar approach was reported in another microchamber PCR array with 4 chambers [Zou et al., 2005]. A 2 × 2 microchamber PCR array was developed on a glass substrate with an individual chamber volume of 2.5 μL. The sensors and actuators were fabricated by vapor depositing platinum. Temperature was controlled within a variation of ±0.5ºC and its heating and cooling rates were 6ºC/s and 3.5ºC/s respectively. A 500 bp DNA fragment was amplified for 30 cycles in 30 minutes, with each cycle composed of 14 s for denaturation, 21 s for renaturation, and 13s for extension.

PCR-based genotyping assays were developed by BioTrove (Woburn, MA), The OpenArray system, which had up to 3072 microchambers on a single device with a dimension of 1" × 3". [Morrison et al., 2006, Brenan, C., 2005]. The substrate was stainless steel and each microchamber required 33 nL of chemical reagents. The top surface of the device was hydrophobic to prevent leakage or evaporation while the inner walls of the microchamber were hydrophilic to keep the reagents inside the reservoirs. An automated loading system was built to distribute the DNA reagent precisely and evenly. A fluorescence detection system was included to monitor the fluorescence intensity of the amplicons in the real-time.

A high throughput PCR was realized in a continuous flow environment by generating DNA droplets in a polycarbonate microchannel [Mohr et al., 2007]. Two inlets were connected with the device, one for DNA cocktail and the other for carrier oil. Each inlet had an independent flow control to determine the size of each droplet. The diameter of the droplets decreased from 155 μm to 100 μm when the oil flow rate decreased from approximately 18 μL/min to 84 μL/min, the DNA cocktail flow rate was a constant 4 μL/min. A 60 bp DNA fragment was amplified in 32 cycles by using two different temperature zones, 95ºC for denaturation and 72º for

renaturation/extension. Numerical simulations and an experiment with temperature-sensitive dye were used to ensure the temperature in the microchannel was correct for amplification. In the experiment, the fluid color in the denaturation section at 95°C was colorless and the color in the renaturation/extension at zone 72°C was opaque, which led to a distinct boundary between the denaturation and renaturation/extension zones at a zero flow rate. When the flow rate was increased to 51 μL/min, the discrete boundary between the two temperature zones disappeared, demonstrating that the temperature transition in a continuous flow environment was significantly affected by convection.

A microdevice with multiple microchannels was developed and used for either the polymerase chain reaction (PCR) or the reverse transcription polymerase chain reaction (RT-PCR) followed by capillary electrophoresis [Toriello et al., 2006, Liu et al., 2006]. The device had three glass layers, one for fluidic actuation, one for heater/channel, and one for resistance temperature detector (RTD) sensors. Another PDMS layer was used as a gasket to prevent leakage between the top and second glass layers. The microchamber required a volume of 380 nL of chemical reagents and the heaters and sensors were Ti/Pt vapor deposited on the glass. The heating rate was faster than 15ºC/s and the cooling rate was faster than 10ºC/s to achieve 30 thermal cycles in less than 27 minutes. Samples were injected into the microchambers pneumatic actuation and kept in the microchambers by pneumatically closing the valves for repeated thermal cycles. After thermal cycling, the amplicons were pushed into the gel for capillary electrophoresis by applying voltages. Both the PCR and the RT-PCR were demonstrated on this device and multiple analyses were realized simultaneously.

A high throughput microfluidic device with thousands of micro pumps and micro valves was developed in multiple layers of PDMS [Liu et al., 2003, Unger et al., 2000]. Due to the

softness of the PDMS, multiple layers of PDMS could be used as micro pumps or micro valves to transport chemical reagents or enclose the analyte at specific locations. In addition, having on-chip mixing and delivery could minimize the times for preparing the chemical reagents, minimizing the times for pipetting. The PDMS membrane in the upper layer was pneumatically deformed and closed the microchannels in the lower layer like a micro valve. The reagent was transported by continuously and orderly deforming the PDMS layer in the upper layer, which moved the analyte in the lower layer. The microfluidic device demonstrated 400 successful PCR reactions simultaneously with only 41 pipetting steps. The PCR cocktail was distributed to the 400 microchambers using the micro pumps and micro valves by deforming the upper layer PDMS layer, then the all device with 400 microchambers was put on a thermal cycler for PCR amplification.

A study was realized to understand chemical reagent distribution in a microfluidic device with multiple chambers [Gong et al., 2006]. Nine micro chambers with different geometries were fabricated between two parallel microchannels on a glass substrate. The inlet microchannel and microchambers were surface treated to be hydrophilic and the outlet was treated to be hydrophobic to act as a micro valve and stop the reagent. The surface treatment also minimized the residual bubbles inside the microchambers. A fluorescent solution was injected into the inlet and flew into the microchambers at a temperature of 90°C to investigate any leakage through the outlet. Since there no significant leakage was observed, the DNA cocktail was injected into the microchambers and a block thermal cycler was used to heat/cool the device for amplification.

A pneumatically-driven real time PCR was developed [Frey et al., 2007]. Three constant temperature zones were aligned along a single microchannel and a 125 nl DNA sample was injected and driven repeatedly through the three temperature zones. An 82% amplification

efficiency was achieved compared to amplicons from a block thermal cycler. A high throughput approach was proposed to extend this microfluidic device to a high throughput device.

Several other high throughput PCR devices have been reported, but they were similar to those described above [Chaudhari et al., 1998, Waters et al., 1998, Belgrader et al., 2001, Chen et al., 2003, Leamon et al., 2003, Yu et al., 2003, Matsubara et al., 2005, Marcus et al., 2006].

3.2.2 Other High Throughput Microsystems

The idea of using a high throughput approach for DNA purification was reported in 1995 [Wang et al., 1995], this approach did not use microtechnology but only used titer plates as the platform. The titer plate was filled with a purification matrix and samples, then the titer plate was fixed and spun at a certain speed to filter the samples to obtain 400 bp DNA fragments. This study used the simplest tools to demonstrate the idea of a high throughput device.

A titer plate-based polymer microfluidic platform used for high throughput purification of nucleic acid acids was designed and fabricated using UV-LIGA [Park et al., 2008, Witek et al., 2008]. Each purification chamber containing 3800 20 μm diameter posts and 96 chambers were arranged on a single 3" × 5" polycarbonate substrate. A universal microfluidic microchannel was designed to connect all 96 chambers and made the injection of chemical reagents into each well easier. The device was operated in both push, by a syringe pump, and pull, by a vacuum pump modes. Purified gDNA from different samples, *B. subtilis, S. aureus, and E. coli*, were isolated with an efficiency of 63% and then amplified in a PCR thermal cycler. Three target amplicons, 159 bp, 204 bp, and 600 bp, were successfully amplified from the thermal cycler demonstrating the capability of purification in this high throughput format.

A polymer 96-well microfluidic device, with 12 columns and 8 rows, used for capillary electrophoresis was developed [Guber et al., 2004, Gerlach et al., 2002]. To achieve the mass

demand of disposable device in biotechnology and medical engineering, a master mold insert was fabricated by micromilling a brass substrate for hot embossing with the PMMA substrates. Capillary electrophoresis was successfully demonstrated in a single device to separate DNA fragments in different sizes under an applied voltage.

A high throughput approach for capillary electrophoresis was reported [Emrich et al., 2002, Paegel et al., 2002]. There were either 96 or 384 microchannels arrayed radially from the center of a disk and a universal detector was designed on the top of the center region of a disk to cover the outlet end of either the 96 or 384 microchannels. The microchannels were patterned by photolithography and they were etched on a glass substrate. The device with 384 lanes, 8 cm long for each microchannel, successfully demonstrated in genotyping 384 individuals for the common hemochromatosis-linked H63D mutation in the human HFE gene in 325 s. The device with 96 lanes, 15.9 cm long for each microchannel, successfully demonstrated sequencing at a rate of 1.7 kbp/min, a 5-fold increase over current commercial capillary array electrophoresis technology.

A high throughput microfluidic device for cell culture was reported [Wu et al., 2008]. The advantage of using microchambers for cell culture was the homogenous and stable culture environment leading to accurate control of the cultured cells. The device was fabricated using multiple PDMS layers and a glass substrate. The 3-D geometry generated microchambers for cell culturing space, microchannels made for delivering fresh culture media, and micro valves/micro pumps realized by multiple PMDS layers made for controlling the flow of the culture media. The micro valves and micro pumps were manipulated by deforming the PDMS membrane pneumatically, which was similar to the previous examples described in section 3.2.1 [Liu et al., 2003, Unger et al., 2000]. Thirty microchambers were made on this device for cell culturing and

the cell viability remained 95% to 98% in 48 hours by monitoring the fluorescence intensity in the microchambers.

3.3 A 96 CFPCR Array on a Polycarbonate Substrate

3.3.1 Design and Dimension of a 96 CFPCR Array

The dimensions of a 96 CFPCR array followed the standard dimensions of a titer plate used in the basic science departments [Soc. Biomolecular Screening (SBS), 2004]. The ultimate goal of this high throughput microsystem is to have its own supporting components such as sample preparation and detection systems in a portable approach. Another possibilities to use the standard dimensions of a titer-plate for a 96 CFPCR array is the potential to integrate it with current high throughput robotic systems (Figure 1.5). Figure 3.1 shows the configuration of this 96 CFPCR array which has 12 columns and 8 rows resulting in 96 individual CFPCRs on a single substrate. Each CFPCR is 8 mm× 8 mm, the gap between each CFPCR is 1 mm, the margin area around the device is 6 mm, which gives a 96 CFPCR array have a length of 120 mm and a width of 96 mm (Figure 3.1).

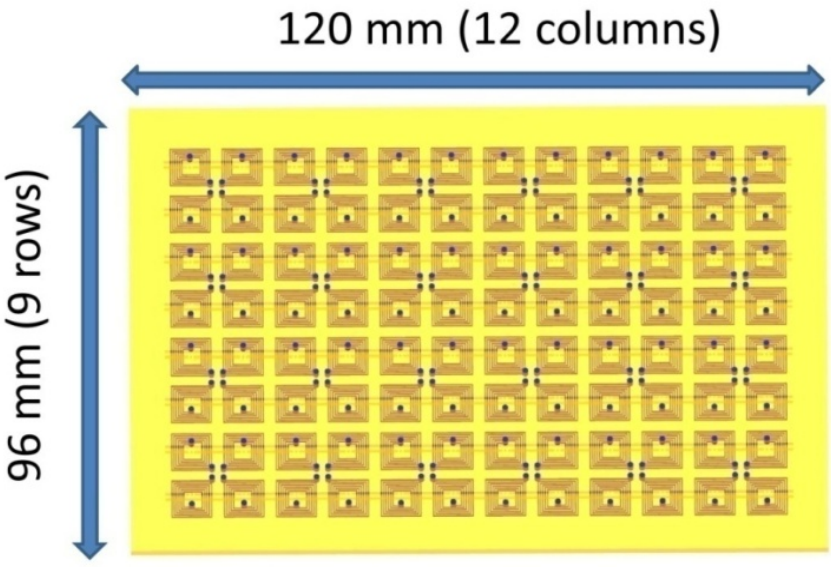

Figure 3.1: The dimension of a 96 CFPCR array.

3.3.2 Design and Dimension of a Single CFPCR Device

In a standard 96 well titer plate, each well is confined in an area of 9 mm × 9 mm. The actual area for a single CFPCR was 8 mm × 8 mm due to a 1 mm wide groove on the backside shared with the adjacent device. Two choices of cycle numbers, 20 cycles and 25 cycles, were designed and used to amplify DNA fragments with different sizes or different concentrations of template. Figure 3.2 shows layouts of single CFPCR devices used: Figure 3.2 (a) shows the layout of a 20 cycle CFPCR and Figure 3.2 (b) shows the layout of a 25 cycle CFPCR. Since the extension step is required to be longer than the other two steps, denaturation and renaturation, the width of the microchannel in the extension zone was designed to be wider than the microchannels in the denaturation and renaturation zones (Figure 3.3). Different width microchannel were designed and fabricated resulting in a time ratio of 1:1:4 corresponding to denaturation, renaturation, and extension. The width of the microchannels in denaturation and renaturation zones was 20 µm and the width in extension zone was 40 µm, with a universal depth of 40 µm. The total length of a 20 cycle CFPCR was 49 cm with a volume of 740 nL and the length of a 25 cycle CFPCR was 63 cm with a volume of 990 nL.

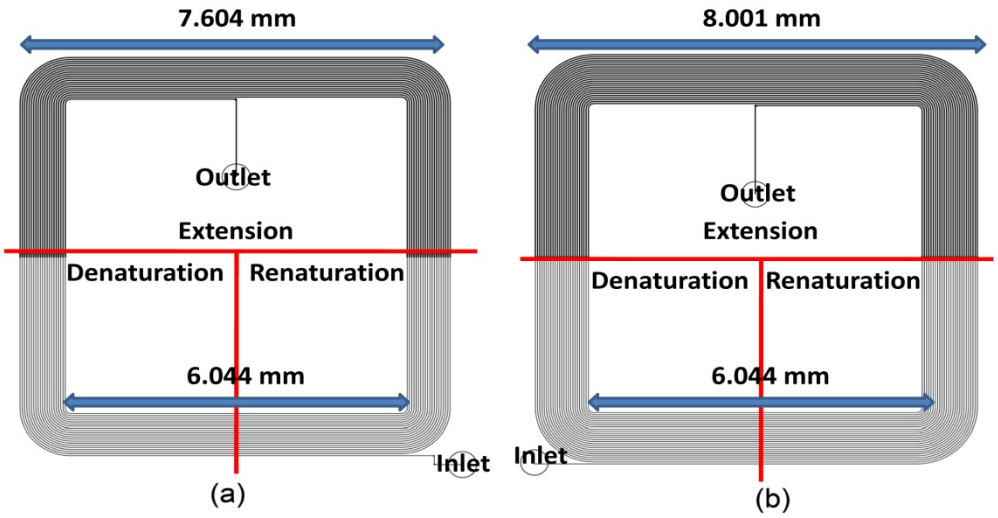

Figure 3.2: The layout of a single CFPCR device (a) 20 cycles CFPCR (b) 25 cycle CFPCR.

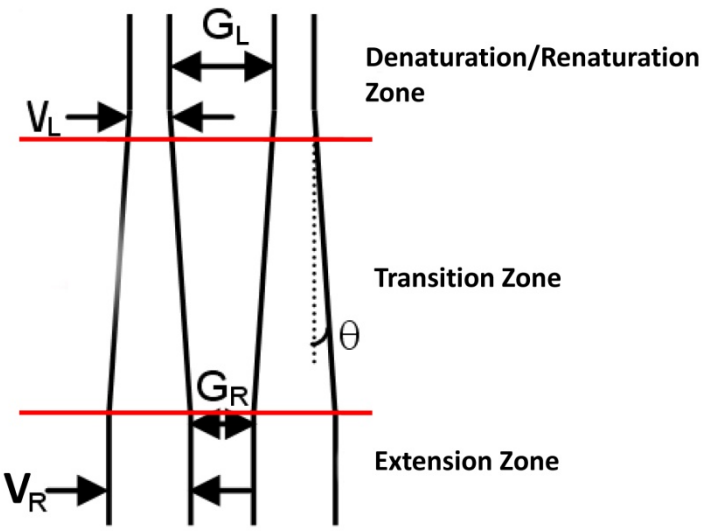

V_L (width of microchannel)= 20 µm
G_L (distance between microchannels) = 40 µm
V_R (width of microchannel)= 40 µm
G_R (distance between microchannels) = 20 µm
Θ= 7.9°

Figure 3.3: The transition zone between either denaturation and extension or renaturation and extension.

3.3.3 Design Concepts for Four Adjacent CFPCR Devices that Share Temperature Zones

Every CFPCR requires three different temperature zones for DNA amplification and a 96 CFPCR array should have 288 distinct temperature zones for multiple amplifications. To simplify the thermal requirement and minimize the number of heating units and capillaries used to operate the 96 CFPCR array, temperature zones were shared by adjacent devices in both the 96 CFPCR array and the multi-zone thermal system. Figure 3.4 shows one arrangement of four CFPCRs together; 4 CFPCRs share the same denaturation/renaturation zone while 2 CFPCRs located either in the upper row or lower row share an extension zone. Once this idea was extended to the design of a 96 CFPCR array, it can significantly reduce the numbers of heating units required for the necessary 288 steady-state temperature zones using a 96 CFPCR array,

only 57 constant temperature areas are needed for sharing including 5 for extension, 28 for renaturation, and 24 for denaturation.

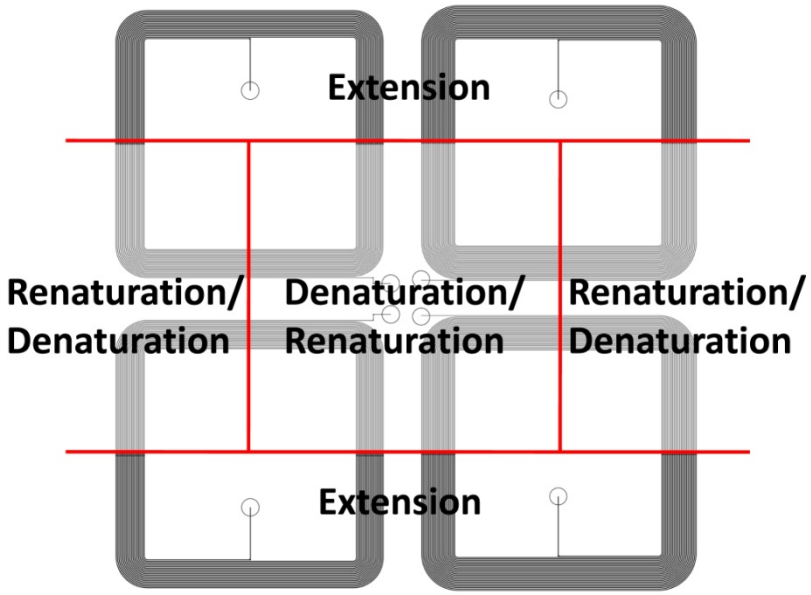

Figure 3.4: The arrangement of 4 CFPCRs on the 96 CFPCR array

3.3.4 Microfabrication of a 96 CFPCR Array on a Polycarbonate Substrate

The substrate material used for the 96 CFPCR array was polycarbonate since it had a glass transition temperature, 155°C-160°C, higher than the temperature required for denaturation reaction in PCR, 94°C. The microfabrication process for a polycarbonate 96 CFPCR array was compLeted by Park and described in several publications [Park et al., 2007, Park et al., 2008].

Polycarbonate 96 CFPCR arrays were produced by double-sided hot embossing at the Center for Advanced Microstructures and Devices (CAMD) using a HEX 02 hot embossing machine (HEX-02, Jenoptik, Jena, Germany) with two mold inserts. The top mold insert, for patterning the 96 microchannels, was fabricated with a UV-LIGA process and the bottom mold insert, for patterning the thermal management features, was micromilled. Figure 3.5 shows the layouts of both mold inserts, Figure 3.5 (a) shows the layout for the 96 well CFPCR array and

the Figure 3.5 (b) shows the layout of the grooves used to achieve required temperature distribution.

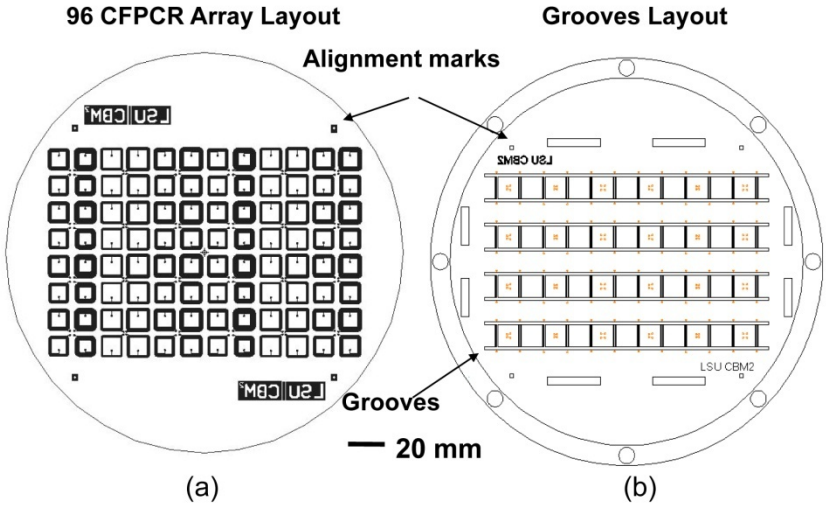

Figure 3.5: The layouts for the two mold inserts and the alignment marks used to align the two mold inserts during hot embossing (a) the layout for the 96 CFPCR array (b) the layout for the grooves used to achieve the required thermal performance.

3.4 Simulation of a Single Nanoliter CFPCR

3.4.1 Challenges and Introduction

Each CFPCR was built in an area of 8 mm × 8 mm and three distinct and uniform temperature zones for denaturation, renaturation, and extension were required. To achieve a large temperature gradient from denaturation, 94°C, to renaturation, 63°C, in a short distance by natural convection, a design which maximized the temperature gradient by increasing the convection area was critical. Numerical simulations were used to determine the physical dimensions of the grooves to realize the required temperature distribution.

Three models were developed: (1) a thermofluidic simulation was used to determine the physical dimension of the groove features for cooling; (2) a thermal simulation was realized to understand the temperature distribution across the 20 microchannels on a single CFPCR device; and (3) a thermofluidic simulation was used to understand the temperature distribution along a

single microchannel at different flow velocities. For the two thermofluidic simulations, the first and third simulations, no lateral heat transfer across the 20 microchannels was assumed because of the uniform temperature distribution of the 20 microchannels in a single CFPCR device. This assumption was based on the use of PID control of the temperature in each zone and confirmed by the thermal simulation results described in Section 3.4.3 which was the second simulation. The first simulation was used to determine the dimensions of the grooves for cooling, which were applied in the second simulation to estimate the temperature distribution over a 96 CFPCR array.

3.4.2 First Model: Design of the Physical Dimensions of the Dual Grooves between the Denaturation and Renaturation

In Section 2.1.6.2, grooves were used to reduce the thermal cross-talk and made each temperature zone independent in a larger footprint CFPCR. A similar idea was applied in the nanoliter CFPCR device with an area of 8 mm × 8 mm. Two models were considered, one with a single groove and the second with dual grooves. The dominant cooling mechanism in both cases was natural convection with a natural convection coefficient of 15 W/m^2 K. The software for finite element analysis (FEA) was ANSYS (vers. 9.0, ANSYS, Inc., Canonsburg, PA). In both numerical simulations, the microchannel was meshed by using a Fluid-Thermal element, FLUID 142, which is a 3-D element with 8 nodes and its degrees of freedom (DOF) includes velocities in three directions, pressure, temperature, turbulent kinetic energy, and turbulent dissipation rate. FLUID 142 can be used in a simulation of solid-fluid interaction analysis in either transient or steady-state simulation. The meshing element for the polymer and copper was SOLID 70, which is a 3-D thermal conduction element with 8 nodes and its only DOF is temperature.

Figure 3.6 shows the configuration and boundary conditions for the simulation model with a single groove. The denaturation temperature in this model was 95°C and the expected

renaturation temperature was 55°C, the actual renaturation temperature depends on the design of the groove feature. Several models with different depths but a fixed width of 1 mm were studied to optimize the thermal performance as a function of groove depth. Static flow was assumed so no pressure was applied at the inlet. A path was defined along the microchannel to monitor the temperature distribution with different groove depths. Figure 3.7 shows that the temperature could achieve 55°C with a 1.4 mm deep groove, and only 0.6 mm thick polycarbonate sheet was left on the opposite side of a 2 mm thick CFPCR device. If a ± 2°C was assumed to be the temperature tolerance band for quantifying the simulation data (Figure 3.7), the results were listed in Table 3.1. In the cases of 1.2 mm and 1.3 mm deep grooves, the temperature of the PCR cocktail did not reach 57°C, the upper boundary of 55°C when considering a ±2 temperature band, so the transition distance and the corresponding temperature gradient were not available in Table 3.1. In cases with 1.4 mm and 1.5 mm deep grooves, the 57°C temperature was achieved; the transition distance for a 1.5 mm deep groove was 0.4 mm shorter and had a higher temperature gradient of 22.11 °C/mm since it had larger effective area for convection.

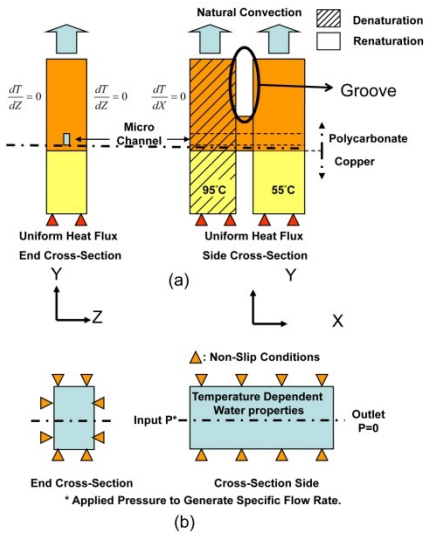

Figure 3.6: The boundary conditions used in the simulations to determine the dimensions of a single groove (a) the thermal boundary conditions (b) the fluid boundary conditions.

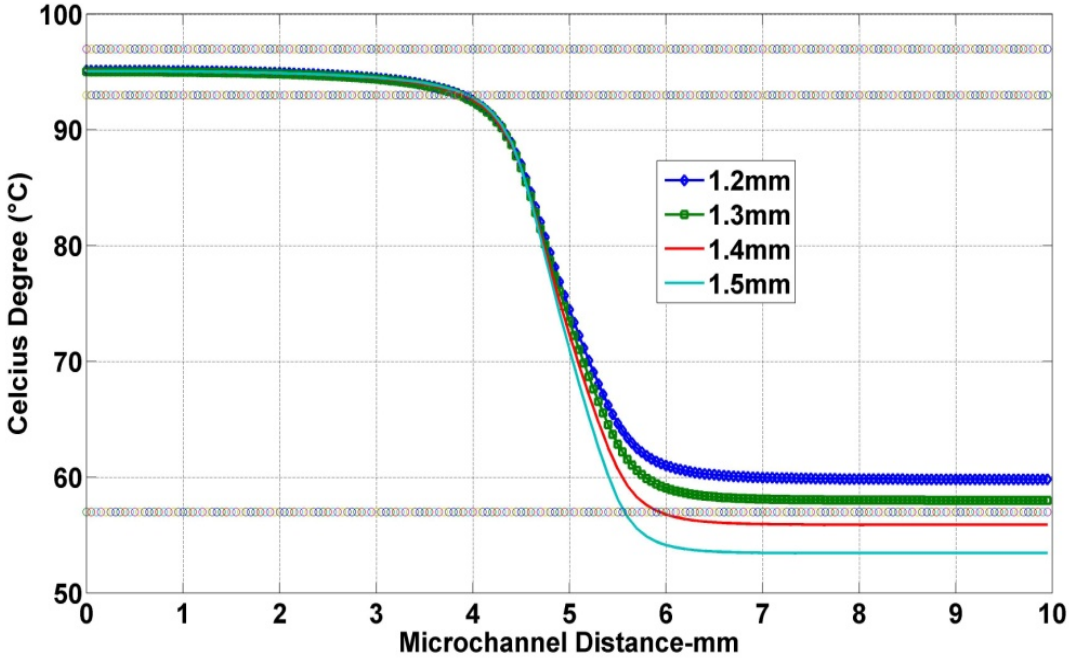

Figure 3.7: The temperature distribution along the microchannel based on different groove depths.

Table 3.1: The transition distance from denaturation to renaturation and the corresponding temperature gradient from the simulation cases with single groove.

	1.2 mm	1.3 mm	1.4 mm	1.5 mm
Distance (mm)	N/A	N/A	2.03	1.63
Temperature Gradient (°C/mm)	N/A	N/A	17.73	22.11

Another approach, using dual grooves, was applied to increase the temperature gradient between denaturation and renaturation while considering rigidity and fabrication. Dual grooves were made between the denaturation and renaturation to increase the convection area, and a 400 μm diameter milling bit was assumed for making the dual grooves. Figure 3.8 shows the boundary conditions used in this simulation. The only difference between Figures 3.6 and 3.8 was the number of grooves between the 95°C and 55°C zones; the distance between denaturation and renaturation zones, 1 mm, was the same for both cases. The meshing elements and

convection coefficients were all the same. A path was defined along the microchannel to monitor the temperature distribution based on different groove depth and Figure 3.9 shows the results with a ±2°C temperature band. The dual grooves with a depth of 1.2 mm could achieve the desired temperature, 55°C, from 95°C with a temperature gradient of 11.1°C/mm. Table 3.2 shows the summary of the simulation results for different groove depths. The groove with a dimension of 1.2 mm deep and 0.4 mm wide could be milled by using a 400 µm diameter milling bit. A smaller milling bit could not drill the groove to 1.2 mm deep due to the maximum aspect ratio limitation of 3 and a larger milling bit would make the groove larger than 1 mm in width and reduced the effective area of the temperature zones in the denaturation or renaturation zones.

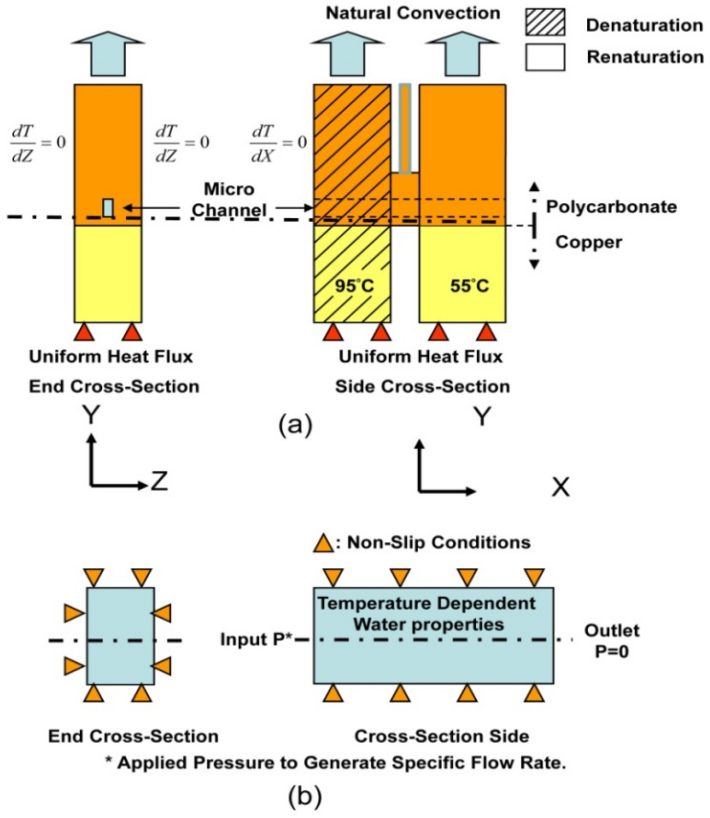

Figure 3.8: The boundary conditions used in the simulations to determine the dimensions of the dual grooves (a) the thermal boundary conditions (b) the fluid boundary conditions.

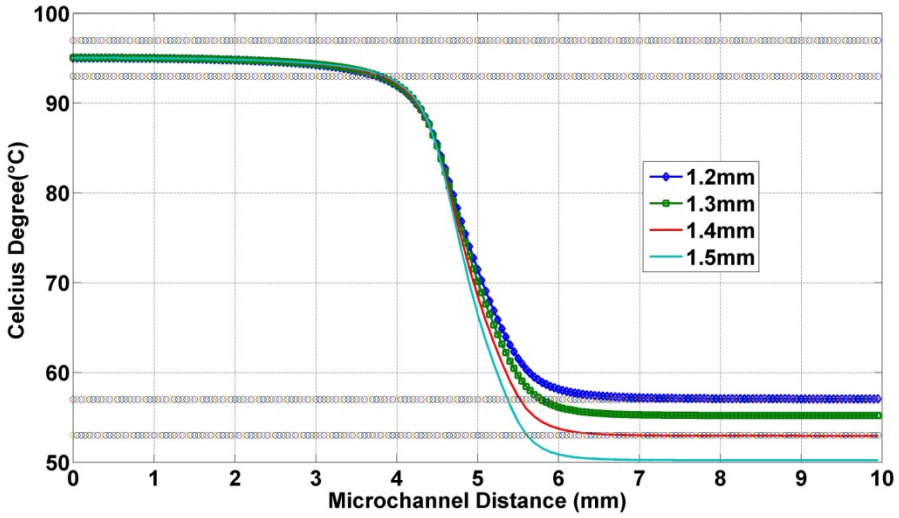

Figure 3.9: The temperature distribution along the microchannel for different depth grooves.

Table 3.2: The transition distance from the denaturation to the renaturation zone and the corresponding temperature gradient from the simulation of cases with dual grooves.

	1.2 mm	1.3 mm	1.4 mm	1.5 mm
Distance (mm)	3.24	2	1.71	1.52
Temperature Gradient (°C/mm)	11.1	18	21.05	23.68

An approach with dual groove features was applied in the design of the single CFPCR to dissipate heat and efficiently reduce the temperature of PCR cocktail in the microchannel from denaturation to renaturation. The selected physical dimensions of the dual grooves were 1.2 mm deep and 0.4 mm wide, those could be fabricated by micromilling.

3.4.3 Second Model: Temperature Distributions across 20 Microchannels on a Single Nanoliter CFPCR

The dual grooves were designed to dissipate the heat from the microchannels during the transition from denaturation to renaturation, and their physical dimensions, 1.2 mm deep and 0.4 mm wide, were determined from the previous thermofluidic simulation described in Section 3.4.2. A thermal simulation was carried out to estimate the temperature distribution of 20

microchannels on a single CFPCR device. In addition, the simulation results could validate the assumption used in the first and third thermofluidic simulations in which no lateral heat transfer across the 20 microchannels was assumed.

Figure 3.10 shows the boundary conditions used in this simulation. The natural convection coefficient was assumed to be 15 W/m^2 K. Three uniform heat fluxes were appLied to achieve the required temperature for each zone and a single microchannel, the innermost microchannel, was modeled inside the polymer device (Figure 3.11 (b)) to understand the temperature distribution along the innermost microchannel. Different size of elements were used to ensure the simulation results were not dependent on the meshing size. The only meshing element used in this simulation was a SOLID 70, which is a 3-D thermal conduction element with 8 nodes and its only DOF is temperature. Figure 3.10 shows the model for the thermal simulation, Figure 3.11 (a) shows the whole model including a single CFPCR device, three copper plates, and a microchannel (embedded), Figure 3.11 (b) shows the innermost microchannel embedded inside the polymer.

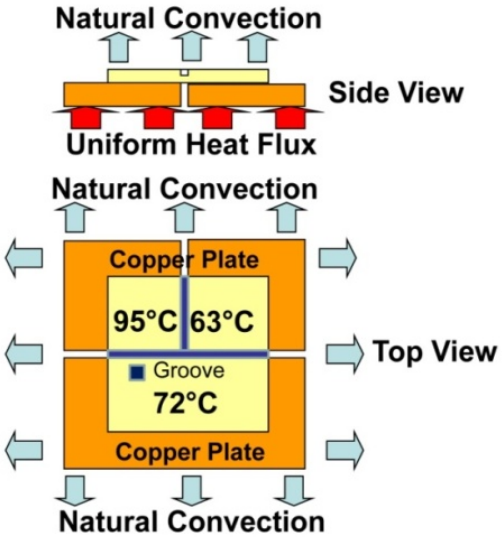

Figure 3.10: The boundary condition of a single CFPCR simulation.

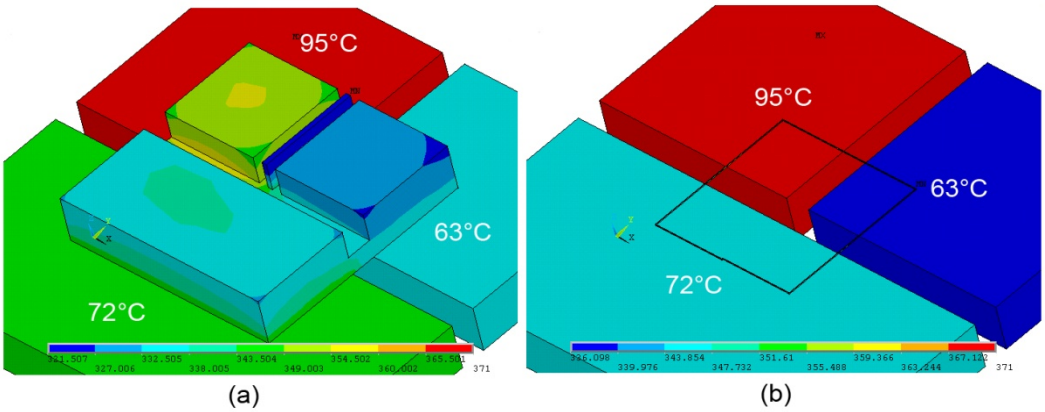

Figure 3.11: The model for numerical simulation (a) the whole model including the single CFPCR device, three copper pLates, and the microchannels (embedded) (b) partial model including three copper pLates and microchannels.

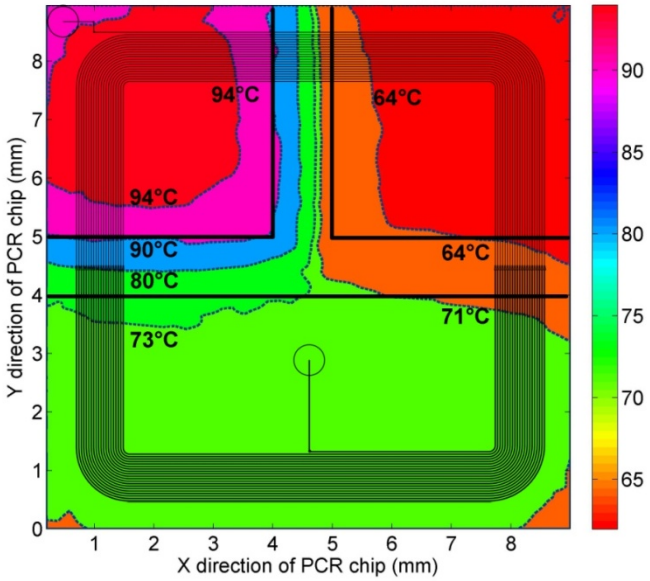

Figure 3.12: The temperature distribution of a cutting surface through the center of the innermost microchannel.

Figure 3.12 shows the temperature distribution of a plane through the center of the microchannel from the simulation. The data were extracted from the simulation results and plotted using Matlab (7.0, The MathWorks, Inc., Natick, MA). The thermal contour was overlapped with a plot of the 20 microchannels, which elucidated the temperature distribution in terms of location of the 20 microchannels. The contours plotted in Figure 3.12 had a temperature band of ± 1°C, 94°C, 73°C, 71°C, and 64°C for quantification. To obtain more detailed

information, a microchannel was built in the simulation model shown in Figure 3.11 (b). Figure 3.13 shows the location of the innermost microchannel and five paths were defined along the innermost microchannel, path 1 for 72°C from the inlet, path 2 for 72°C to 63°C, path 3 for 63°C to 95°C, path 4 for 95°C to 72°C, and path 5 for 72°C to the inlet. Figure 3.14 shows the temperature distribution along each path as defined in Figure 3.13. If a ± 1°C was assumed to be the tolerance band for each target temperature, Figure 3.14 can be quantified and listed in Table 3.3 and Table 3.4. Table 3.3 shows the transition distance and the temperature gradient of path 3, path 4, and path 5, and Table 3.4 shows the temperature uniformity along path 1 and path 5 in extension temperature. In Table 3.4, a 0.29°C variation for path 1 and 1 0.19°C variation for path 5 were observed; the reason can be explained from Figure 3.13, compared to path 5, path 1 is closer to the 63°C and had a larger temperature drop from the extension zone center to the edge. From Figure 3.14, the maximum sized DNA fragment can be amplified will be approximately 1000 bp at a flow velocity of 1 mm/s since a 10 mm long microchannel was within the ±1°C temperature band in extension, based on the DNA extension rate of 100 bp/s, while denaturation and renaturation reactions are less than 1 second [Wittwer et al., 1990].

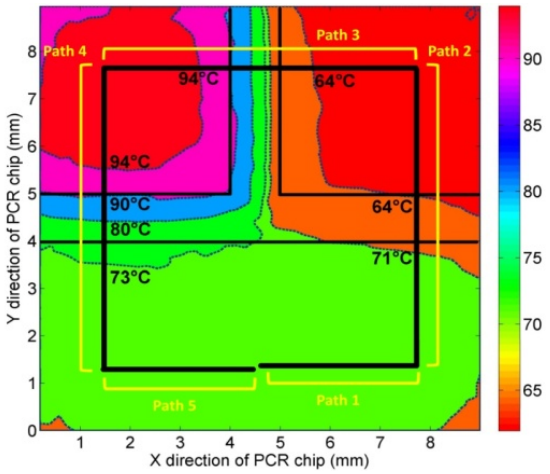

Figure 3.13: The innermost microchannel defined as 5 paths in the thermal contour.

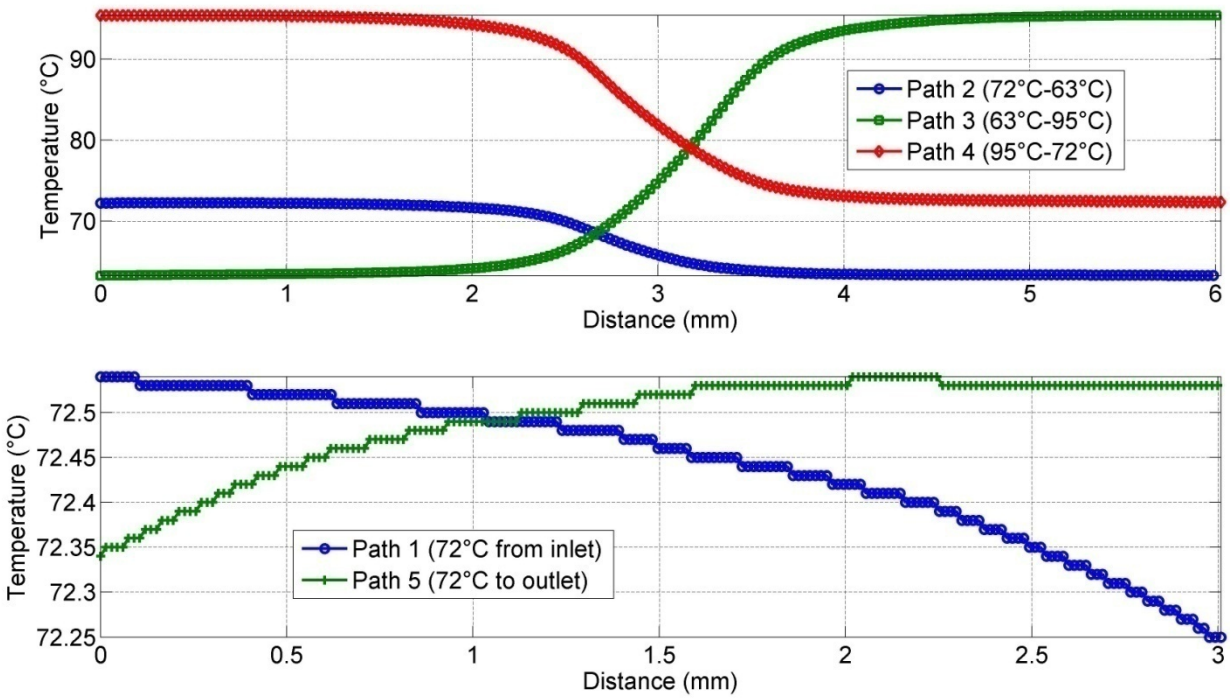

Figure 3.14: The temperature distributions of paths defined in Figure 3.13 to monitor the thermal performance of the innermost microchannel.

Table 3.3: The transition distance and temperature gradient for path 2, path 3, and path 4 defined in Figure 3.13.

	Path 2 (72°C to 63°C)	Path 3 (63°C to 95°C)	Path 4 (95°C to 72 °C)
Transition Distance (mm)	1.16	2.22	1.96
Temperature Gradient (°C/mm)	6.03	13.51	10.71

Table 3.4: The temperature uniformity of path 1 and path 5 in Figure 3.13.

	Path 1 (72°C from the inlet)	Path 5 (72°C to the inlet)
Temperature Variation (°C)	0.29	0.19

3.4.4 Third Model: Thermofluidic Simulations along a Single Microchannel

To understand the temperature distribution along a microchannel at different flow rates, a single microchannel model was used. In Section 3.4.3, the temperature distribution along the microchannel only considered the thermal conduction, but thermal convection actually had the

same magnitude of heat transfer as thermal conduction in a microchannel [Chen, 2006]. These heat transfer phenomena in a microchannel affected the dwell time and transition time of the PCR cocktail at each temperature zone, resulting in different chemical reaction output [Chen et al., 2008].

Figure 3.15 shows the boundary conditions used in this simulation to understand the temperature distribution along a microchannel at different flow velocities. Figure 3.15 (a) shows the thermal boundary conditions and Figure 3.15 (b) shows the fluidic boundary conditions. Different pressures were applied at the inlet of the microchannel to push the water, representing the PCR cocktail in the simulation, go through the microchannel at different flow velocities. Different size of element was used to ensure the simulation result was independent of meshing size.

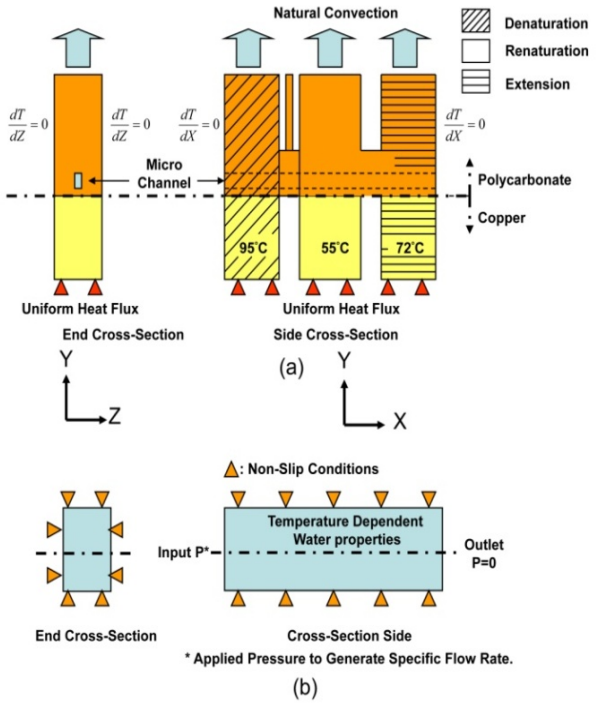

Figure 3.15: The boundary conditions used to understand the temperature distribution along a microchannel at different flow velocities (a) Thermal boundary conditions (b) fluidic boundary conditions.

Figure 3.16 (a) shows the temperature distribution for the whole model, including all three temperature zones, Figure 3.16 (b) is an enlarged view to show the thermal contours in the area around the dual grooves between denaturation and renaturation, and Figure 3.16 (c) shows the temperature distribution of the area around the single groove between renaturation and extension. Figure 3.17 (a) shows the temperature distribution in the transition zone which connected 20 µm wide renaturation microchannel and the 40 µm wide extension microchannel with a universal depth of 40 µm; the temperature of the cocktail increased from the renaturation zone to the extension zone. Due to the change of microchannel geometry from renaturation to extension, the flow profile changed as well. Figure 3.17 (b) shows the flow velocity in the microchannel, the maximum flow velocity occurred along the center streamline and it was reduced as the PCR cocktail flowed into the transition zone and the wider microchannel in the extension. The purpose of designing this transition zone and the wider microchannel in the extension zone was to achieve the nominal time ratio of 1:1:4 for denaturation, renaturation, and extension.

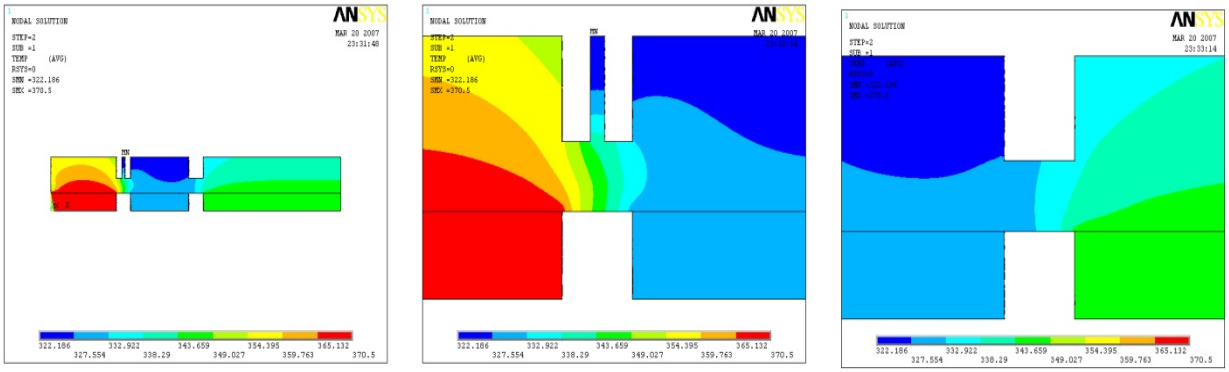

Figure 3.16: (a) The thermofluidic simulation results for a single microchannel (b) enlarged thermal contour to show the temperature distribution around the area of dual grooves between denaturation and renaturation (c) enlarged thermal contour to shows the temperature distribution around the area of the single groove between renaturation and extension.

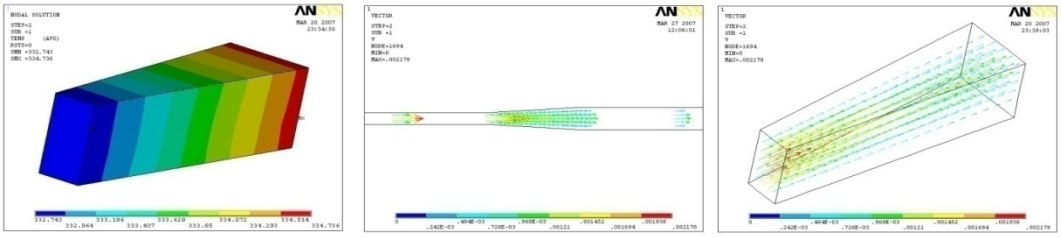

Figure 3.17: (a) The temperature distribution of the transition microchannel from renaturation to extension (b) the flow profile of PCR cocktail from a narrow microchannel in renaturation to a wider microchannel in extension (c) enlarged view to show the flow profile in the transition microchannel.

A path was defined along the center of the microchannel to monitor the temperature distribution of the PCR cocktail at different flow velocities. The different flow velocities were realized by changing the pressure on the inlet of the microchannel to push the DNA cocktail through the microchannel. Figure 3.18 shows the temperature distribution along the microchannel at different mean flow velocities from 1 mm/s to 4 mm/s with a ±2°C temperature band. The data shown in Table 3.5 are the transition and dwell distance for the different flow velocities from Figure 3.18 with the temperature bands. When the PCR cocktail flowed at a higher velocity, the transition distance increased and the dwell distance decreased. Table 3.6 shows the transition and dwell time at different flow velocities, the dwell time was reduced as the flow velocity increased, which indicated that the PCR cocktail had less time to complete the chemical reactions before moving to the next temperature zone.

3.5 Experimental Performance of a Single Nanoliter CFPCR

Every nanoliter CFPCR is a single unit of the 96 CFPCR array. Understanding the limiting performance is important for the design and expectation of the performance of the whole 96 CFPCR array. Three experiments were carried out to understand the performance of the single nanoliter CFPCR. Amplification of a 99 bp λ-DNA at different flow velocities,

amplification of different lengths of λ-DNA fragments at different renaturation temperatures, and the limiting concentration of λ-DNA template for a successful amplification.

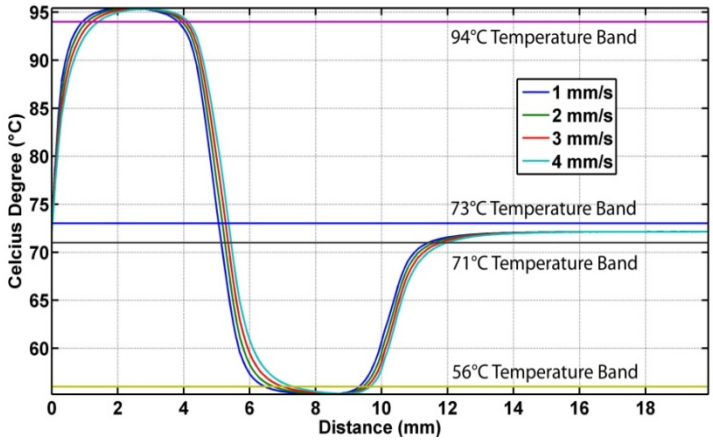

Figure 3.18: The temperature distribution along the microchannel at flow velocities from 1 mm/s to 4 mm/s.

Table 3.5: Summary of the residence and transition distances (mm) of the PCR cocktail in each temperature zone at different flow velocities (mm/s).

Flow Velocity	72°C-94°C	94°C	94°C -55°C	55°C	55°C -72°C	72°C
1mm/s	0.93	2.89	2.63	2.86	2.09	8.59
2mm/s	1.07	2.87	2.78	2.71	2.16	8.41
3mm/s	1.23	2.81	2.96	2.54	2.23	8.23
4mm/s	1.41	2.72	3.17	2.35	2.32	8.03

Table 3.6: Summary of residence and transition times (s) of the PCR cocktail in each temperature zone at different flow velocities (mm/s).

Flow Velocity	72°C-94°C	94°C	94°C -55°C	55°C	55°C -72°C	72°C
1mm/s	0.93	2.89	2.63	2.86	2.09	8.59
2mm/s	0.535	1.435	1.39	1.36	1.08	4.20
3mm/s	0.41	0.937	0.987	0.847	0.743	2.743
4mm/s	0.353	0.68	0.793	0.588	0.58	2

3.5.1 Amplification of 99 bp DNA Fragment at Different Flow Velocities

The numerical simulations described in Section 3.4.4 showed that the PCR cocktail in a microchannel had less dwell time and a longer transition time when the flow velocity was increased, which implied that the DNA cocktail might not have sufficient time to complete the chemical reaction before moving to the next temperature zone at high flow velocity [Chen et al., 2008].

A 99 bp λ-DNA fragment was amplified in both the 20 cycle and 25 cycle devices. The PCR cocktail was injected into the microchannel by a syringe pump (PicoPlus, Harvard Apparatus, Holliston, MA) at flow velocities from 1mm/s to 4 mm/s. The DNA template was a 48 kbp λ-DNA c1857Sam7 (USB, Cleveland, OH) target. Primers were designed to generate a 99 bp DNA amplicon. The forward primer was 25 bp and the reverse primer was 24 bp in length. The forward primer was a complement to the negative strand and its sequence was 5'-GATGAGTTCGTGTCCGTACAACTGG-3'. The reverse primer was a complement to the positive strand and its sequence was 5- GAC GGG CAATCA GTT CAT CTT TCG -3 (Integrated DNA Technologies, Coralville, IA). The PCR cocktail contained 10 mM Tris-HCl (PH 8.3), 1.5 mM $MgCl_2$, 50 mM KCl (USB, Cleveland, OH); the concentrations of the nucleotides was 200 μM (USB, Cleveland, OH), the template was 4.46 ng/μL, each forward and reverse primer was 0.2 μM, bovine serum albumin (BSA) was 0.5 μg/μL, and *Taq* DNA Polymerase was 0.1 units/μL (USB, Cleveland, OH). This PCR cocktail was amplified in a bench top thermal cycler to validate the correct composition and temperature, the amplicons from the thermal cycler was used as a reference standard for the CFPCR results from the microfluidic devices. The cycling conditions were 2 min at 94°C for preheating, 7 min at 72°C for a final extension, and twenty thermal cycles consisting of denaturation for 1 minute at 95°C,

renaturation for 1 minute at 63°C, and extension for 1 minute at 72°C. The total time needed for this process on the benchtop system was about 2 hours.

The microfluidic device was double-sided hot embossed and thermal fusion bonded with a 0.25 mm thick polycarbonate to sheet seal the microchannels. A band saw was used to cut a single CFPCR device out of a 96 CFPCR array. Two PEEK capillaries (1543, Nature Peek Tubing, Upchurch, Oak Harbor, WA) were inserted into the inlet and outlet and fixed by applying Epoxy glue around the capillary. Three copper plates were used to support the single CFPCR device and supply the uniform temperature to the device while three individual Kapton heaters (KH104/5-P, Omega, Stamford, Connecticut) were attached underneath the copper plates. Three individual Type-K thermal couples (5TC-TT-K-30-36, Omega, Stamford, Connecticut) were inserted between the heaters and copper plates to measure the temperature as feedback for the thermal controllers (Serious 96, Watlow, St. Louis, Missouri). Figure 3.19 shows the experiment setup for a single CFPCR device. The PCR cocktail was pumped into the microchannel via the inlet and collected from the outlet.

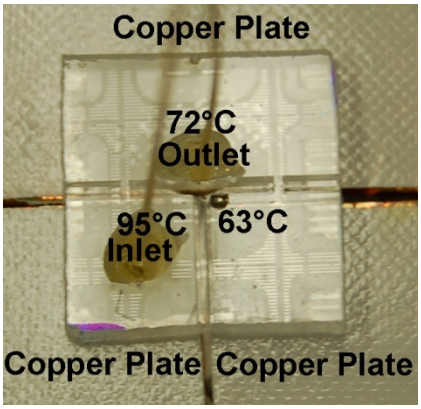

Figure 3.19: The experiment setup for a single CFPCR experiment.

A volume of 3 to 5 μL of PCR amplicons was collected from the outlet and used for electrophoresis. Figure 3.20 (a) shows the results for amplicons from a device with 20 cycles. The marker in the gel (M) shows the correct size of the amplicons. The total length of the

microchannel in a 20 cycle CFPCR device was 487.647 mm and the average time to compLete a thermal cycle was 24.38 s/cycle, 12.19 s/cycle, and 8.13 s/cycle corresponding to flow velocities of 1 mm/s, 2 mm/s, and 3 mm/s. The reduced amplification efficiency compared to the control, the amplicons from the thermal cycler, might be due to enzyme adsorption to the microchannel wall as discussed in Chapter 2 or insufficient dwell time for complete chemical reaction at high flow velocities.

Figure 3.21 shows the amplification results of a 99 bp DNA fragment from a 25-cycle CFPCR device with the same chemical composition, temperature distribution, and flow velocities.

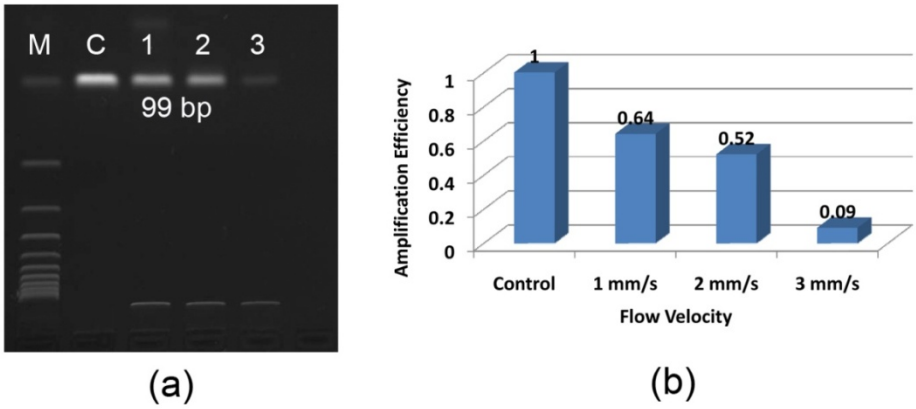

Figure 3.20: Amplification of a 99 bp λ-DNA fragment at different flow velocities from 1 mm/s to 3 mm/s in a device with 20 cycles.

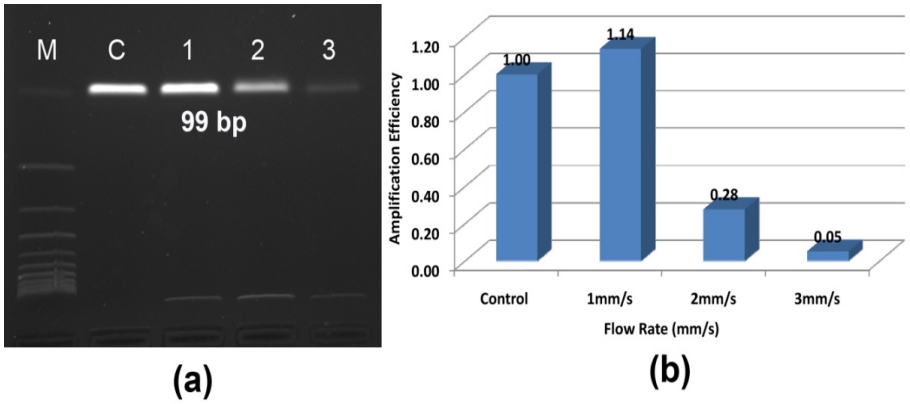

Figure 3.21: Amplifying a of 99 bp λ-DNA fragment at different flow velocities from 1 mm/s to 3 mm/s in a device with 25 cycles.

3.5.2 Amplifications of Different Length DNA Fragments

The renaturation temperature varies from 55°C to 70°C depending on the sample and primers. The numerical simulations in Section 3.4.2 used 55°C as the target temperature in renaturation to determine the dimensions of the dual grooves, which enabled the CFPCR device to amplify a broad range of samples with different renaturation temperatures. To demonstrate the appropriate design of this nanoliter CFPCR device, different length DNA fragments from a λ-DNA template were amplified by changing the renaturation temperature and primers. The denaturation and extension temperatures were the same for all samples. Table 3.7 shows the renaturation temperature required for six different length DNA fragments from 99 bp to 997 bp; the temperature range was from 55°C for a 500 bp DNA fragment to 69°C for a 150 bp DNA fragments.

The experimental apparatus was described in Section 3.5.1 and the different renaturation temperatures were realized by changing the set point temperature on the thermal controller. Figure 3.22 shows the results for different lengths of DNA fragments from 99 bp to 997 bp. The amplification was carried out on a 20 cycle CFPCR device. The intensity of the band for each DNA fragment is different; this might be caused by many factors such as the chemical reaction strength between primers and template, the chemical environment in a microchannel, the physical environment of the microchannel, and the amount of absorbed dye to different length of DNA fragments. The intensity did not necessarily mean that a stronger intensity band had better amplification efficiency.

Table 3.7: Different renaturation temperatures for ampLifications of different length of λ-DNA fragments

DNA fragments (bp)	99	125	150	200	500	997
Renaturation Temperature (°C)	63	65	69	62	55	68

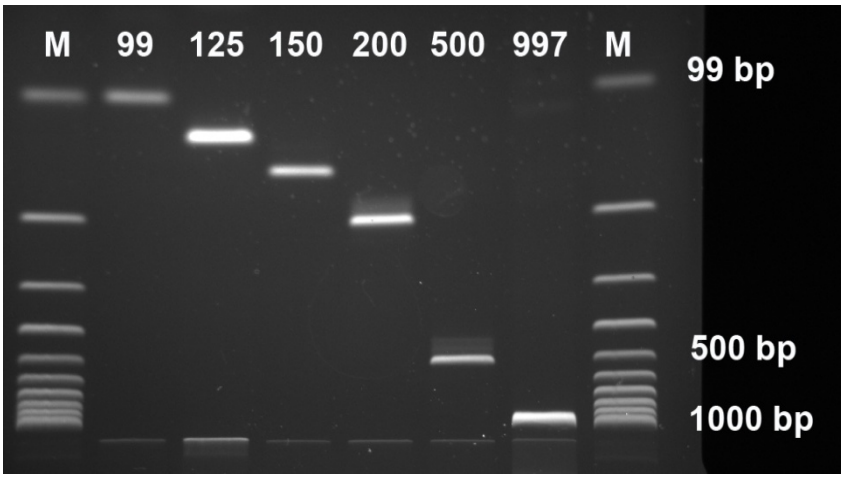

Figure 3.22: The amplification results for different lengths of DNA fragments from a 20 cycle nanoliter CFPCR device.

3.5.3 Limiting Concentration of λ-DNA Template in a Single Nanoliter CFPCR

Another experiment was carried out to determine the limiting concentration of λ-DNA template required for a successful amplification. Two lengths of DNA fragments were chosen in this experiment, 99 bp and 997 bp DNA fragments from a λ-DNA template. The concentration of the template used for the previous two experiments was 4.46 ng/μL, corresponding to 8×10^{7} initial copies of the λ-DNA template. Table 3.8 shows the concentration used in this experiment from 4.46×10^{-5} ng/μL to 4.46 ng/μL, corresponding from 8×10^{2} to 8×10^{7} in initial copies.

Figure 3.23 shows the results for the 99 bp DNA fragments. The lowest concentration successfully amplified on a 20 cycle CFPCR was 9×10^{-3} ng/μL and the lowest concentration on a 25 cycle CFPCR was 4.46×10^{-4} ng/μL corresponding to 8000 initial copies of the DNA template. For a 997 bp template, the lowest concentration for λ-DNA template was 0.223 ng/μL corresponding to a 4×10^{6} initial copies of DNA template. Since the detection used in this experiment was agarose gel with bromide to stain the amplicons, the sensitivity was poor and required better tools with better sensitivity like capillary electrophoresis (CE) to determine the lowest concentration used in the nanoliter CFPCR device.

Table 3.8: The concentration and initial copy numbers of λ-DNA tempLates used in the limiting concentration experiments.

	1	2	3	4	5	6	7
Concentration of the λ-DNA (ng/μL)	4.46	4.46×10^{-1}	4.46×10^{-2}	9×10^{-3}	4.46×10^{-3}	4.46×10^{-4}	4.46×10^{-5}
Number of Corresponding copies	8×10^{7}	8×10^{6}	8×10^{5}	40×10^{4}	8×10^{4}	8×10^{3}	8×10^{2}

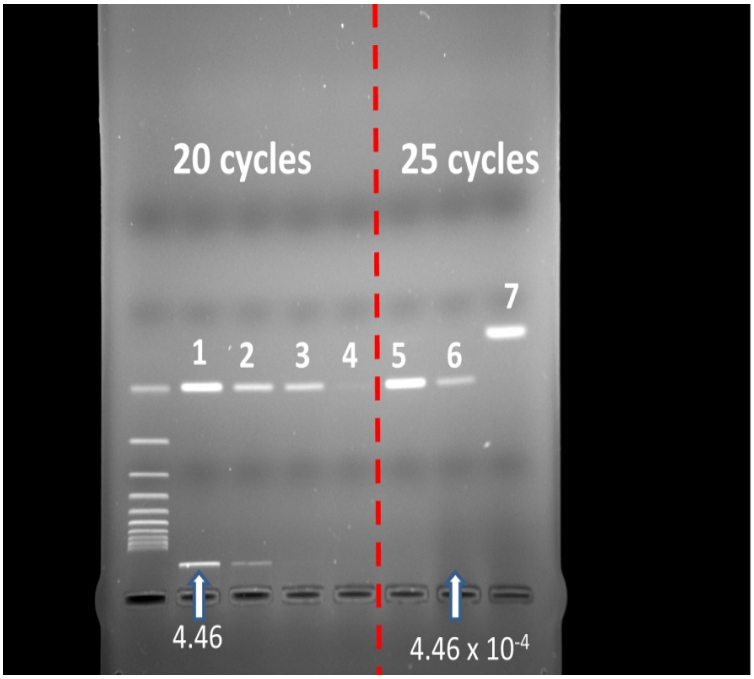

Figure 3.23: Results of the limiting concentration of the λ-DNA template for a successful 99 bp amplification, the concentration and the initial copies corresponding to each lane were listed in Table 3.8.

3.6 Conclusions

A nanoliter CFPCR was designed and fabricated as a unit of a 96 CFPCR array. Finite element simulations were used to determine the physical dimensions of the dual grooves needed to reach the maximum temperature gradient between the denaturation and renaturation zones within the capability of the micromilling machine. The simulations were also used to estimate the temperature distribution as a function of the locations of 20 microchannels and the temperature distribution along a single microchannel at different mean flow velocities.

Several experiments, including infrared camera and biochemical experiments, were realized to validate the simulation results and understand the limiting performance of a single nanoliter CFPCR. The experiments show that the design of a CFPCR was appropriate for amplifying different DNA fragments from 99 bp to 997 bp at different mean flow velocities from 1 mm/s to 4 mm/s. The limiting concentration of λ-DNA template for a successful 99 bp amplification was 4.46×10^{-4} ng/μL corresponding to 8000 copies. Those experimental results proved that the design of a 20 cycle CFPCR with a volume of 740 nL was appropriate and suitable for being a single unit in a 96 CFPCR array.

CHAPTER 4: A MULTI-ZONE THERMAL SYSTEM

4.1. A Multi-zone Thermal System

Microfluidic devices have been under development for over two decades and most of the reported achievement emphasized on single functional microfluidic device. A microfluidic system integrating all of the necessary components, which can significantly upgrade the current medical tools available for fighting acute infectious diseases and result in improving public health, is the direction researchers have been working toward. To realize a microfluidic system based on nucleic acid analysis, several thermal inputs are needed for certain chemical reactions as thermal cell lysis, the polymerase chain reaction (PCR), and the ligase detection reaction (LDR). A multi-zone thermal system is in urgent demand for an integrated system, which has the capability to control multiple temperature zones in different locations on a single substrate leading to multiple chemical reactions in sequence or in parallel.

4.2. Thermal Requirements for a 96 CFPCR Array

A high throughput microfluidic thermal reactor, a polycarbonate 96 CFPCR array, was described in the Chapter 3. The 96 CFPCR array can amplify 96 different DNA fragments of interest in parallel and have the potential to integrate with other functional components as a high throughput microfluidic system. To realize a 96 amplifications simultaneously, a multi-zone thermal system is required to support multiple temperature zones to a single microfluidic device. In Chapter 2 and Chapter 3, continuous flow polymerase chain reactor (CFPCR) was described as an alternative method to amplify DNA fragments. Each CFPCR requires the following three steady-state temperature zones for amplification, 90-94°C for denaturation, 50-70°C for renaturation, and 72°C for extension. A 96 CFPCR array requires 288 steady-state temperature zones. Figure 3.2 shows the layout of each CFPCR within an area of 8 mm× 8 mm. Denaturation and renaturation are within a 4 mm × 4 mm area while the extension zone is within a 4 mm × 8

mm area. The three different temperature zones of each CFPCR should be uniform and discrete from each other to ensure the best performance of every chemical reaction in the microchannels.

4.3. Ideas to Realize Multiple Temperature Zones for A 96 CFPCR Array

To realize 288 steady-state temperature zones simultaneously, Figure 4.1 (a) shows a configuration for a multi-zone thermal system. The idea behind this multi-zone thermal system was based on the sharing of a constant temperature copper strip by multiple CFPCRs. In total eighteen copper strips were used to realize 288 temperature zones including six copper strips for denaturation (95°C), seven for renaturation (63°C), and five for extension (72°C). Figure 4.1 (b) shows an enlarged configuration of copper strips and each CFPCR was designed to sit on three different copper strips with three different temperatures. In the extension zone, each copper strip was shared by either twelve or twenty-four CFPCRs while in the denaturation or renaturation zone, each copper strip was shared by either eight or sixteen CFPCRs (Figure 4.1 (a)). The copper strips for denaturation and renaturation were arranged in columns while the copper strips for extension overlaid them orthogonally (Figure 4.2). The dimensions of the copper strips for denaturation and renaturation was 96 mm × 8 mm with a various thickness between 2mm to 5 mm and the dimension of copper strips for extension was 132 mm × 8 mm × 2 mm.

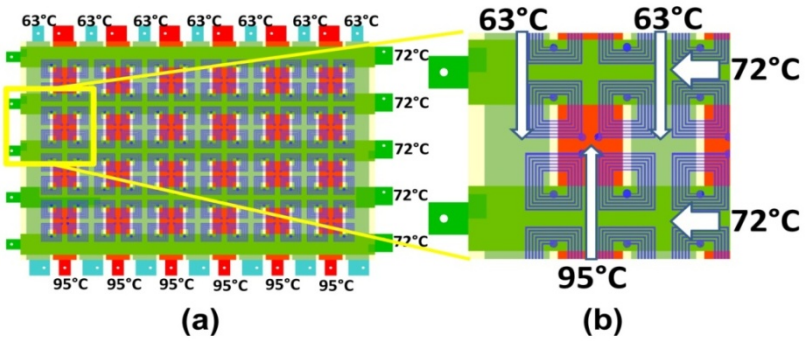

Figure 4.1: (a) An idea of using eighteen copper strips to realize 288 steady-state temperature zones simultaneously (b) an enlarged figure showing the configuration of three copper strips used for denaturation (95°C), renaturation (63°C), and extension (72°C).

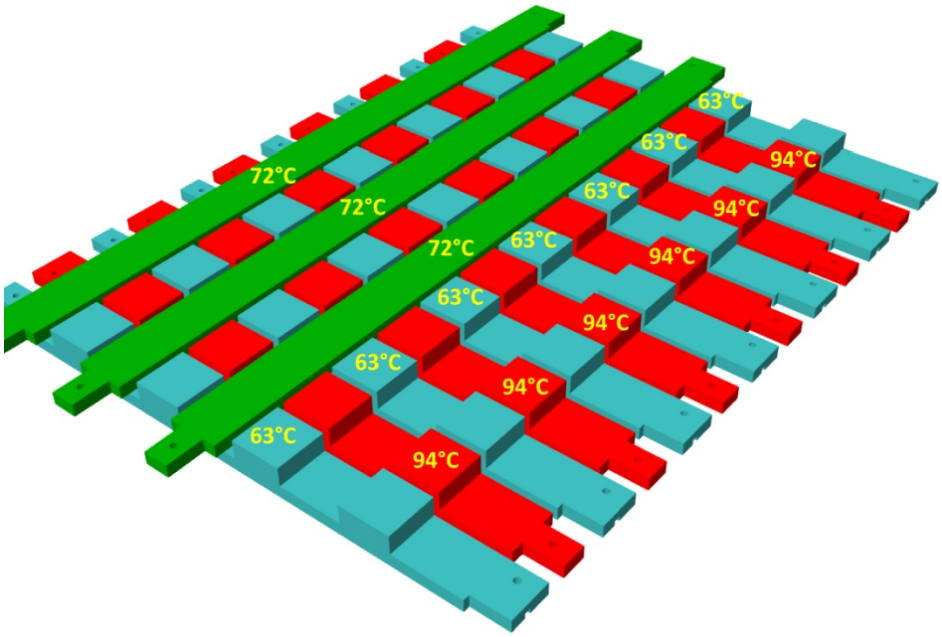

Figure 4.2: The copper strips for denaturation (95°C) and renaturation (63°C) were arranged in columns while the copper strips for extension (72°C) overlaid them orthogonally.

4.4. Numerical Simulation

To understand the temperature distribution of each copper strip and the thermal cross-talk phenomena based on the configuration shown in Figure 4.2, finite element analysis (FEA) was used. Two numerical simulations were carried out to estimate the lowest temperature achievable in the renaturation zone. The first model only had one active heating unit to support the denaturation zone and the second model had two active heating units to support denaturation and extension. Since the renaturation zone was not active in both simulations, the final temperature distribution of the renaturation copper strip was determined by the thermal cross-talk from the denaturation zone in the first model and from the denaturation and extension zones in the second model.

4.4.1. Modeling and Boundary Conditions

An area near the center of the thermal stage was selected in Figure 4.3 as the representation model, since the center area had symmetric boundary conditions, while the areas

close to the thermal stage boundaries which had the side cooling effects. The selected area in Figure 4.3 included partial copper strips for denaturation, renaturation, and extension, and the boundaries around the area were assumed adiabatic. To reduce the thermal cross-talk, the short copper strips for denaturation and renaturation were undercut to make them islands and increase the gap distance between the copper strips. Furthermore thermal insulation material was used to cover most of the area of each copper strip to decrease the thermal cross-talk. Figure 4.4 (a) shows the short copper strip after undercutting; the pillar supporting the top island was 4 mm square and Figure 4.4 (b) shows the short copper strip covered by thermal insulation material to reduce heat transfer between strips.

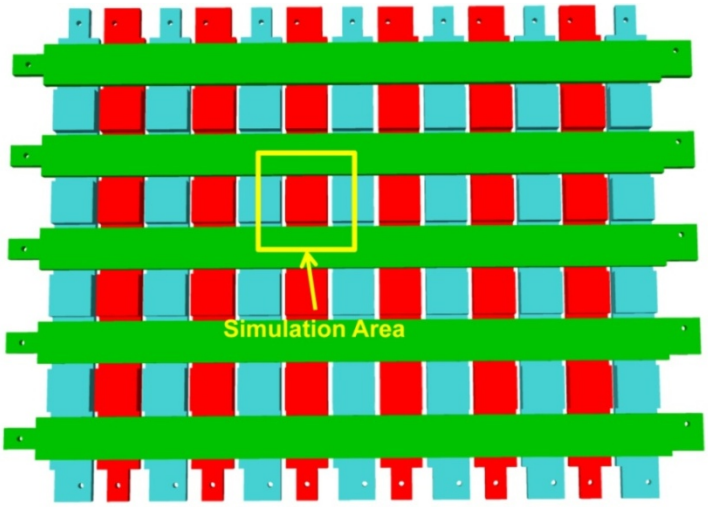

Figure 4.3: The rectangle shows the area used in the simulation

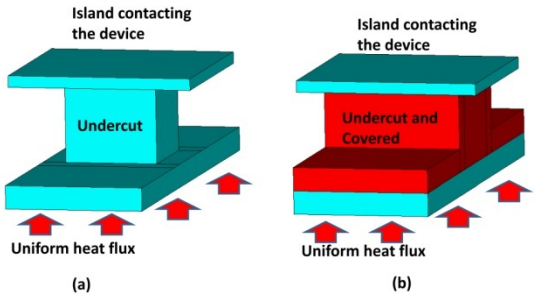

Figure 4.4: (a) Short copper strip after undercutting (b) Short copper strip after undercutting covered by thermal insulation material.

Figure 4.5 (a) to Figure 4.5 (c) show the boundary conditions used in the numerical simulations. The purpose of the simulations was to investigate the lowest temperature that could be achieved in the renaturation copper strips in the presence for heat transfer from the denaturation (95°C) and extension (72°C) zones. The boundary conditions of the copper strips were considered as adiabatic to the surrounding copper strips. Two paths were defined in Figure 4.5 (d) to monitor the temperature distributions from denaturation to renaturation (Path 1) and from denaturation to extension (Path 2). Table 4.1 lists the material properties of copper [9821K14, McMaster, Atlanta, GA], polycarbonate [Goodfellow, Oakdale, PA], thermal insulating materials [Heat Sink Pads, Digi-Key, Thief River Falls, MN] used in the simulations. The material properties of air between each copper strip considered the thermal convection and radiation [Mitchell, 2002].

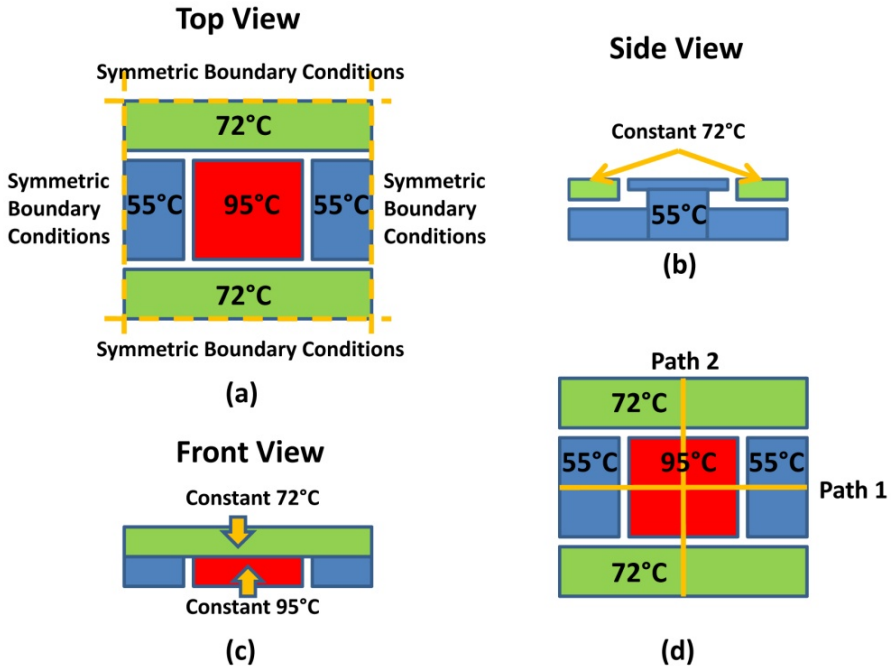

Figure 4.5: (a) (b) (c) Boundary conditions applied in numerical thermal analysis (d) paths defined for monitoring temperature distribution from denaturation (95°C) to renaturation (55°C) (path 1) and denaturation (95°C) to extension (72°C) (path2).

Table 4.1: Material properties of polycarbonate, copper, and thermal insulating materials for thermal simulations.

	Thermal Conductivity (W/m K)	Density (Kg/m^3)	Specific Heat (J/ Kg K)
PC	0.02	1200	1200
Copper	398	8940	398
Thermal Insulating Material	0.0155	190	1047

4.4.2. Numerical Simulation Results

The first simulations had only one active heating unit for denaturation (95°C) and the simulation results could be used to estimate the thermal cross-talk between denaturation and renaturation. The modeling and boundary conditions were described in Figure 4.5. The simulation results of two paths are shown in Figure 4.6. Path 1 defined in Figure 4.5 (d) was the temperature distribution between the denaturation (95°C) and renaturation (55°C) zones while Path 2 monitored the temperature distribution between denaturation (95°C) and extension (72°C). The temperature of the renaturation copper strip was approximately 55°C and the temperature of the extension step was 56.5°C. Both temperatures were contributed by the thermal cross-talk from the denaturation zone. Although the temperature distribution of the extension copper strip was affected by the denaturation temperature via thermal cross-talk, the resultant temperature, 56.5°C, was still lower than the desired temperature, 72°C, so it could be actively controlled to the preferred value. But in the case of the renaturation copper strip, the temperature from thermal cross-talk was 55°C, which might exceed the required temperature, 55°C, after adding another heating unit for extension to the model.

The second model used active heating units for denaturation (95°C) and extension (72°C), to further understand the thermal cross-talk between each copper strip. The modeling and the boundary conditions were described in Figure 4.5 (d) and the simulation results are shown in Figure 4.7. Defined path 2 between denaturation (95°C) and extension (72°C) showed expected temperature distribution precisely. But defined path 1 between denaturation (95°C) and renaturation (55°C) produced a temperature of 61°C in the renaturation zone, 6°C higher than the target value because of the thermal cross-talk from denaturation (95°C) and extension (72°C).

Thermal cross-talk affected the temperature distributions in the copper strips in the renaturation and extension zones. The thermal cross-talk between copper strips produced a renaturation zone at 55°C and an extension zone at 56.5°C. With an active heater input on the extension zone, the renaturation temperature zone could not achieve the required temperature, 55°C, due to the thermal cross-talk between zones.

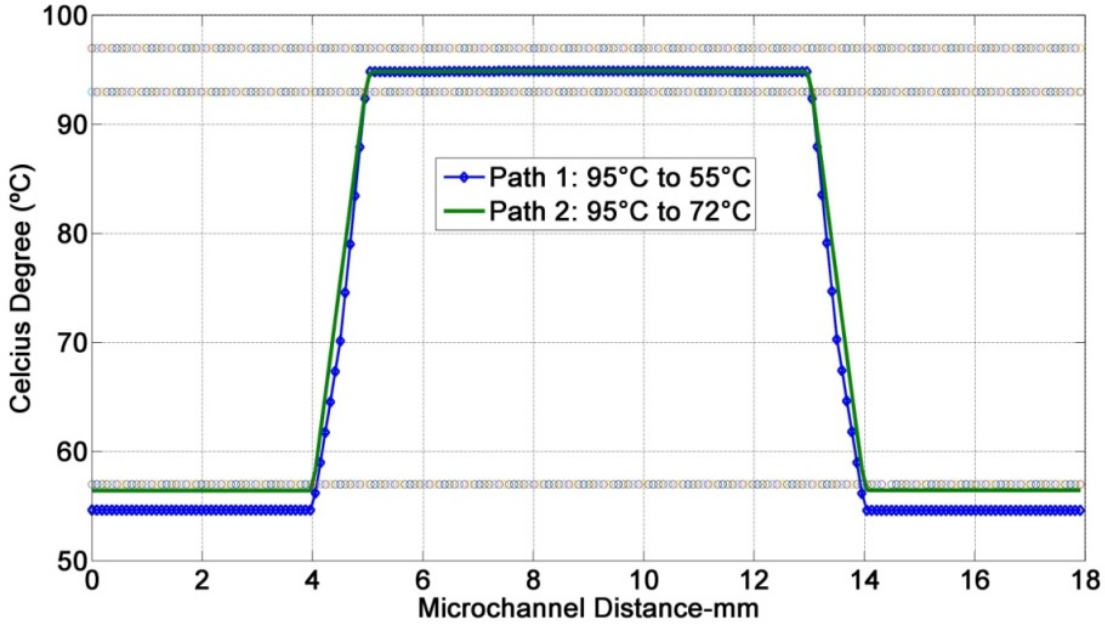

Figure 4.6: The temperature distribution along the two paths defined in Figure 4.5 (d) in the first thermal simulation with one active heating zone (denaturation, 95°C).

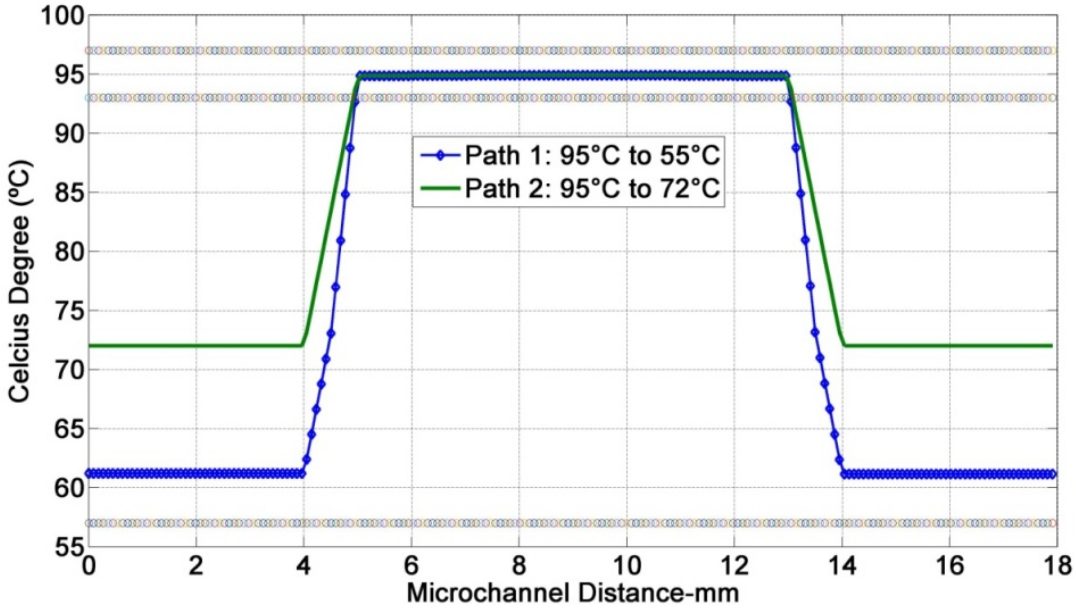

Figure 4.7: The temperature distribution along the two paths defined in Figure 4.5 (d) in the second simulation which had two active heating zones.

4.5. Fabrication and Assembly

The multi-zone thermal system was based on multiple CFPCRs sharing copper strips. Copper is a high thermal conductivity material, which would lead to a uniform temperature distribution due to the smaller temperature gradient. Eighteen copper strips were needed to realize 288 steady-state temperature zones, in addition to thermocouples, thermal controllers, thin-film heaters, power supplies, and hardware were also required to build the multi-zone thermal system.

4.5.1. Components for a Multi-zone Thermal System

Each heating unit in a multi-zone thermal system included a k-Type thermal couple [5SC-TT-K-30-36, Omega, Stamford, CT], a commercial thin-film heater [HK5161R78.4L12, Minco, Minneapolis, MN], a thermal controller [Watlow 96AO-CCAA-AABB, TSCI Corporation, Houston, TX], and a 3-Amp fuse [RadioShack, Fort worth, TX] to protect the heater and thermal controller, and eighteen heating units were connected to a power supply [1743B, BK Precision, Yorba Linda, CA]. A polycarbonate stage (Figure 4.8) was fabricated to

support the eighteen copper strips and those copper strips were installed in grooves in the polycarbonate stage to ensure the correct position to obtain precise temperatures. Polycarbonate was used as the stage material to minimize the heat loss from the copper strips to the ambient environment via the polymer because of the low thermal conductivity of polycarbonate. An aluminum box was designed, fabricated, and assembled to carry all of the components and supported the polycarbonate stage while the polymer stage carrying all copper strips was bolted with the aluminum box.

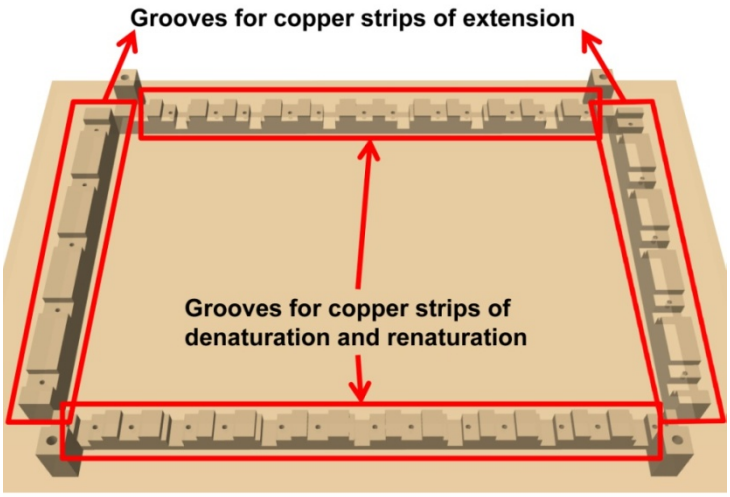

Figure 4.8: Schematic of the polycarbonate stage to support eighteen copper strips.

4.5.2. Assembly of a Multi-zone Thermal System

In Figure 4.8, the height of the grooves for the extension copper strips were higher than those for the denaturation and renaturation copper strips, which made the top surfaces of all copper strips have the same height after assembly to evenly support a 96 CFPCR array. For assembly, the copper strips for denaturation and renaturation were assembled on the polycarbonate stage first, then the extension copper strips were overlaid orthogonally. Figure 4.9 shows the polycarbonate stage carrying the eighteen copper strips after assembly and each copper strip was fixed in the groove by screws at both ends.

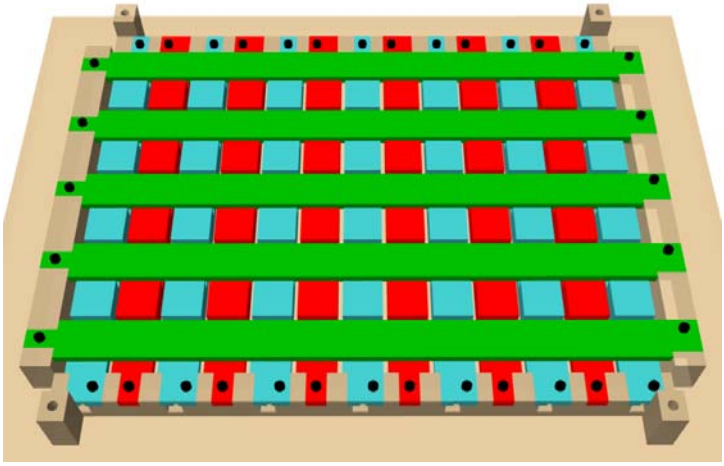

Figure 4.9: Eighteen copper strips were fixed on the polycarbonate stage.

After assembling the polycarbonate thermal stage with the eighteen copper strips (Figure 4.10 (b)), the thermal stage was assembled in the aluminum box as shown in Figure 4.10 (a).

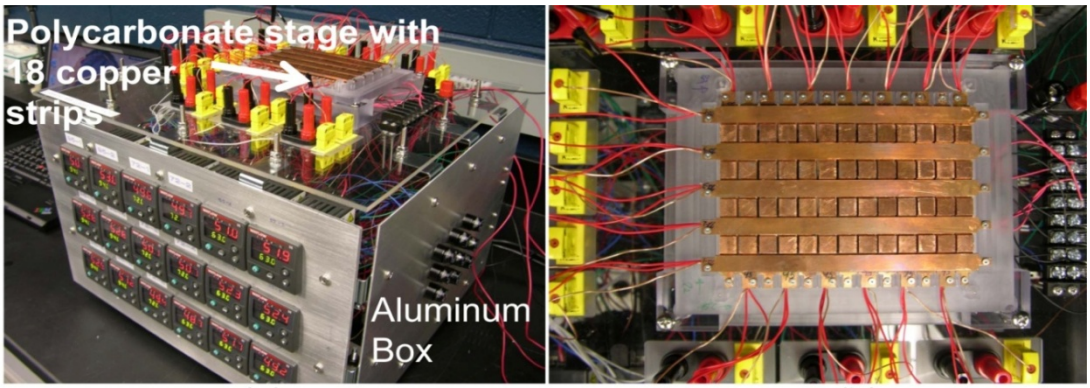

Figure 4.10: (a) The aluminum box contained the polycarbonate stage with 18 copper strips, thermal controllers, and all required electronic hardware (b) The polycarbonate stage with 18 copper strips after assembling with thermocouples, thermal controllers, and commercial thin-film heaters.

4.5.3. A 96 CFPCR Array Assembly with a Multi-zone Thermal System

To setup a 96 CFPCR array on the multi-zone thermal system, a device holder was designed. This 96 CFPCR array holder was made of aluminum and it ensured a good contact between the 96 CFPCR array and the eighteen copper strips leading to a good heat transfer from

copper strips to the 96 CFPCR array. Figure 4.11 shows the layout of the 96 CFPCR array holder which was used to push the perimeter of the 96 CFPCR array.

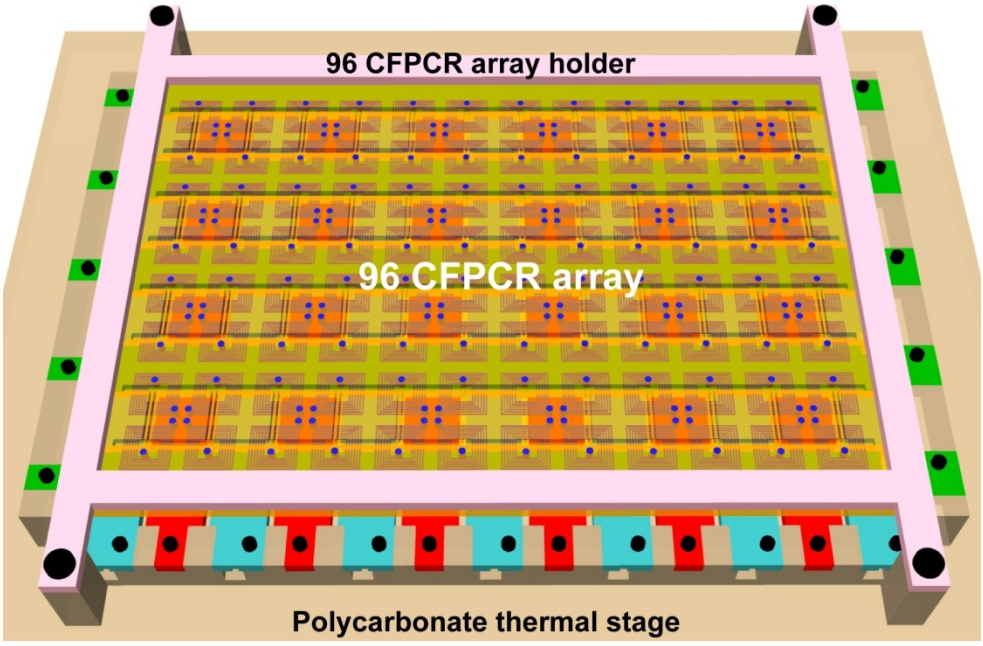

Figure 4.11: A 96 CFPCR array holder was designed and fabricated to ensure good contact between a 96 CFPCR array and the copper strips heating stage resulting in a good heat transfer.

4.6. Infrared Camera Experiments

To measure the surface temperature distribution of multiple CFPCRs on the multi-zone thermal system, an infrared camera was used. The first experiment focused on the temperature distribution of eight CFPCRs arranged in a column and the second experiment investiagted the temperature distribution of the 96 CFPCR array with eighteen active copper strips.

4.6.1. IR Camera Experiment on Eight CFPCRs Arranged in A Column

In the first experiment, eight 25-cycle CFPCRs arranged in a column, as shown in Figure 4.12, were used. Seven copper strips were used to define three different temperatures for them, as shown in Figure 4.13, one for denaturation, one for renaturation, and five for extension. Eight CFPCRs had the same temperatures for denaturation and renaturation since they shared the same

copper strips, the five copper strips for the extension zones were all at 72°C. In Figure 4.13, the column of devices including eight CFPCRs was attached to the copper strips using thermal double-sided tape (BER159-ND, Digi-Key, Thief River Falls, MN) since the 96 CFPCR array holder (Figure 4.11) could not be used for the column device. The thermal double-sided tape supplied a good thermal path from copper strips to the column devices while strongly holding the column device during experiments.

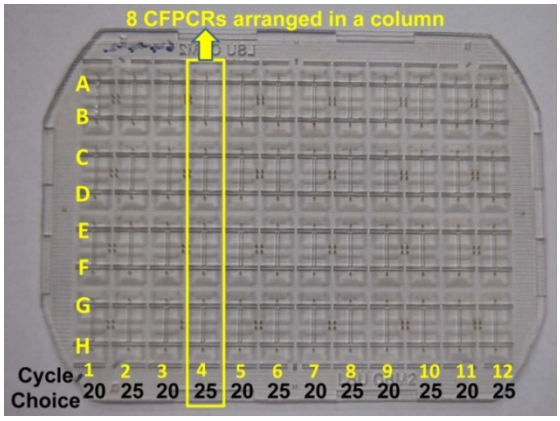

Figure 4.12: Eight CFPCRS arranged in a column were used for temperature measurements.

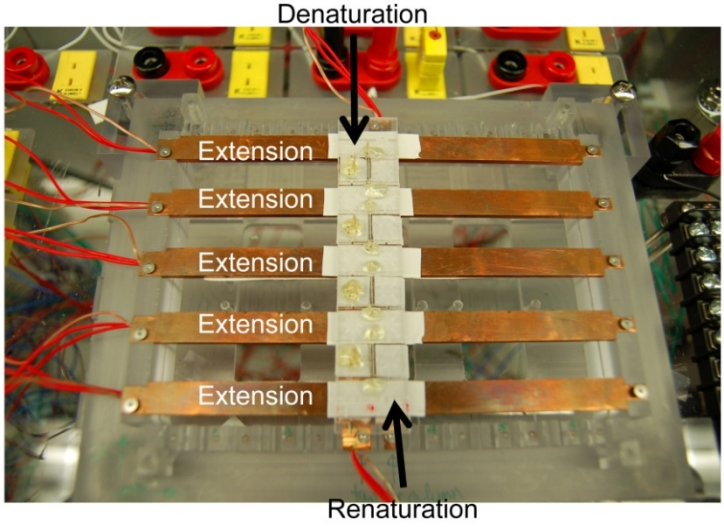

Figure 4.13: The first experiment used seven copper strips to support eight CFPCRs arranged in a column, one copper strip for denaturation, one for renaturation, and five for extension.

An infrared (IR) camera (ThermaCAM® SC3000, FLIR SYSTEMS, Boston, MA) connected to a personal computer was used to monitor the temperature distribution of the column

device in real-time starting when power was supplied to the heaters. After a steady-state temperature distribution was achieved, IR images of the CFPCR were captured. Matlab (7.0, The MathWorks, Inc., Natick, MA) was used to convert the IR images into thermal contour plots. The first DNA samples amplification required a temperature of 63°C for renaturation and 95°C for denaturation and 72°C for extension, so these temperature were used in the IR camera experiment. Figure 4.14 (a) shows the IR image of the column of devices and Figure 4.14 (b) shows the thermal contours converted from IR image using Matlab. The variation in the denaturation zone was 95°C ± 2°C and the variation in the renaturation and extension zone was 63°C ± 1°C and 72°C ± 1°C respectively.

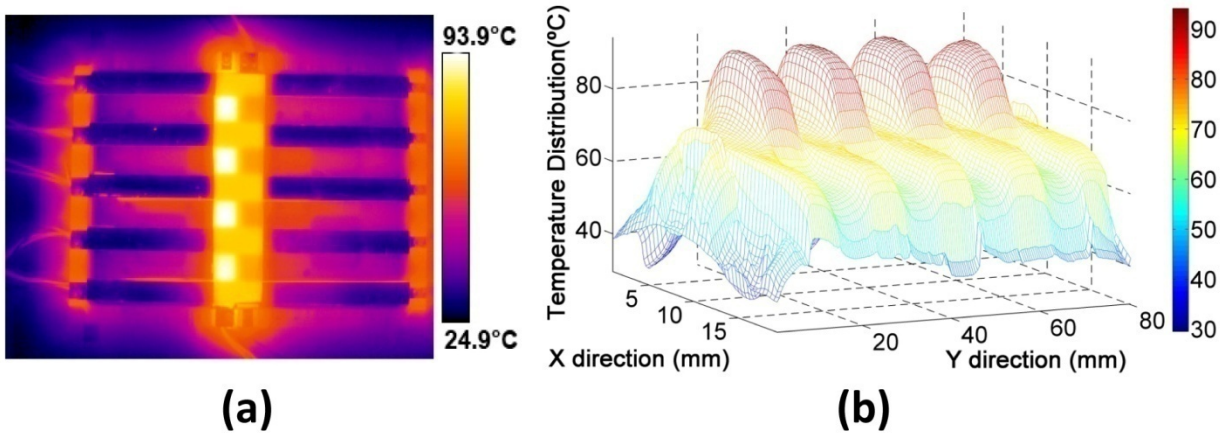

Figure 4.14: (a) The IR image of a column device composing eight CFPCRs supported by seven copper strips, one for denaturation, one for renaturation, and five for extension (b) The IR image was converted into thermal plot using Matlab.

To further understand the thermal performance of a column of devices, eleven paths were defined in Figure 4.15. Path 95 was defined along the copper strip for denaturation, path 63 was defined along the copper strip for renaturation, five paths of 72 were defined to assess the uniformity of these copper strips for extension. Path 1 to path 4 were defined from denaturation to renaturation. The experimental results for each path defined in Figure 4.15 are shown in Figure 4.16 to Figure 4.18 with a ±2°C temperature band for quantification purposes. Figure 4.16

shows the temperature distribution along path 95 and path 63. Along the path 95, peak 2 and peak 3 had larger dwell distances than peak 1 and peak 4 in the denaturation zone because peak 1 and peak 4 were closer to the device edge and were influenced by natural convection. The temperature of peak 4 was lower than the other three peaks and it might be due to the poor attachment between the device and the copper strip during the experiment. Along path 63, the same temperature phenomena were observed, peak 1 and peak 4 had shorter dwell distances in the renaturation zone. Figure 4.17 shows the temperature distribution on the five paths across the extension copper strips, and Figure 4.18 shows the temperature distribution along the four paths.

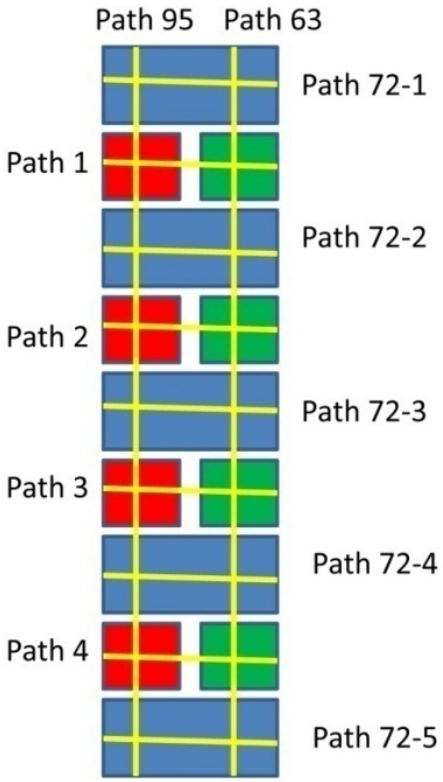

Figure 4.15: Eleven paths were defined to understand the temperature distribution across different temperature zones.

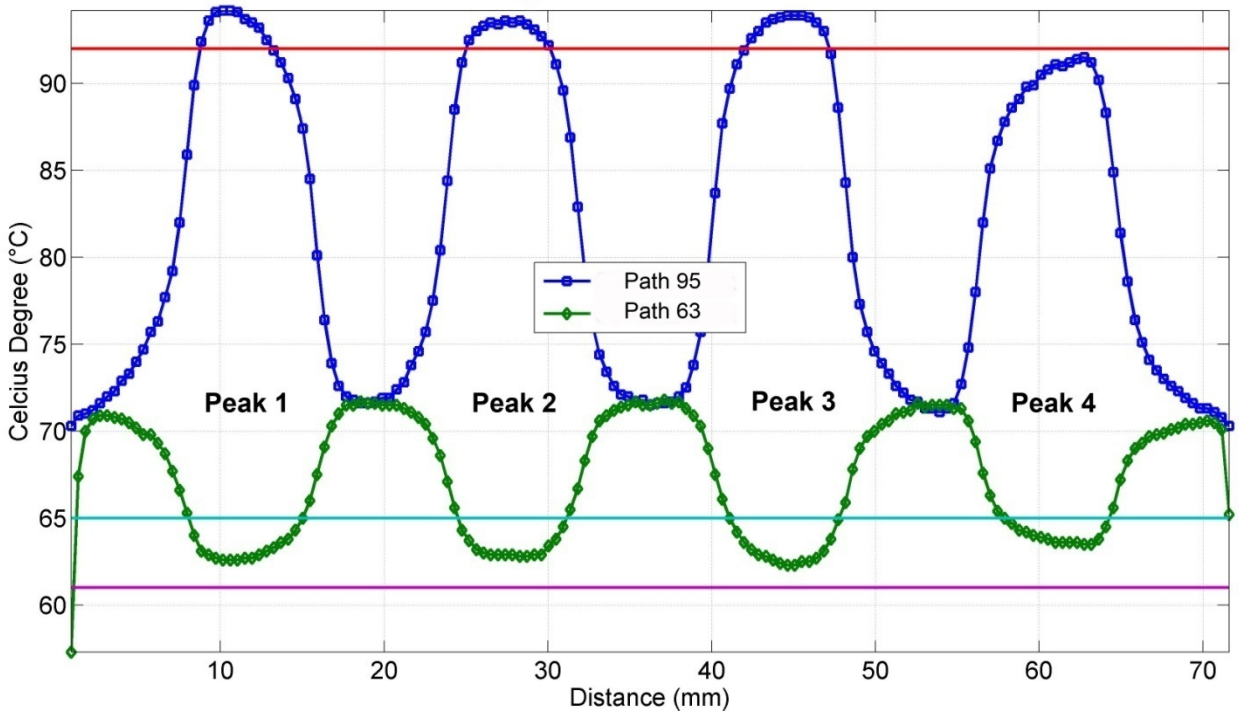

Figure 4.16: The temperature distribution of path 95 along the denaturation copper strip and path 63 along the renaturation copper strip.

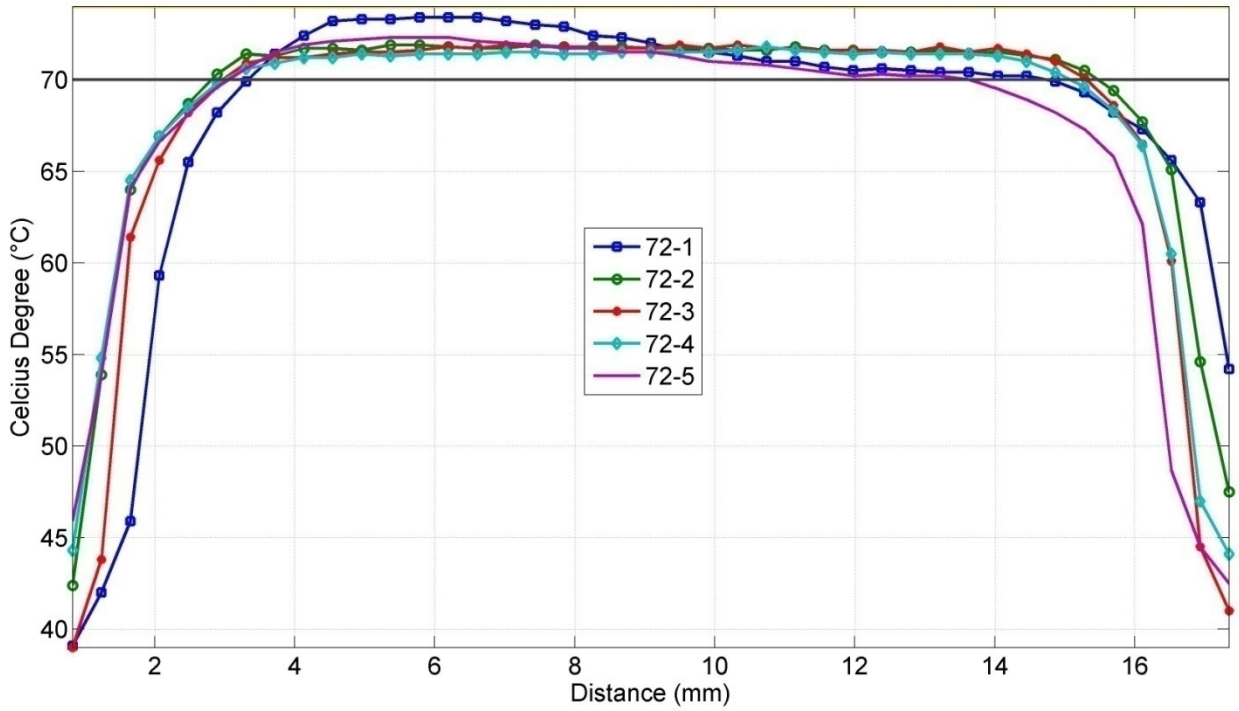

Figure 4.17: The temperature distribution of five paths along five extension copper strips defined in Figure 4.15.

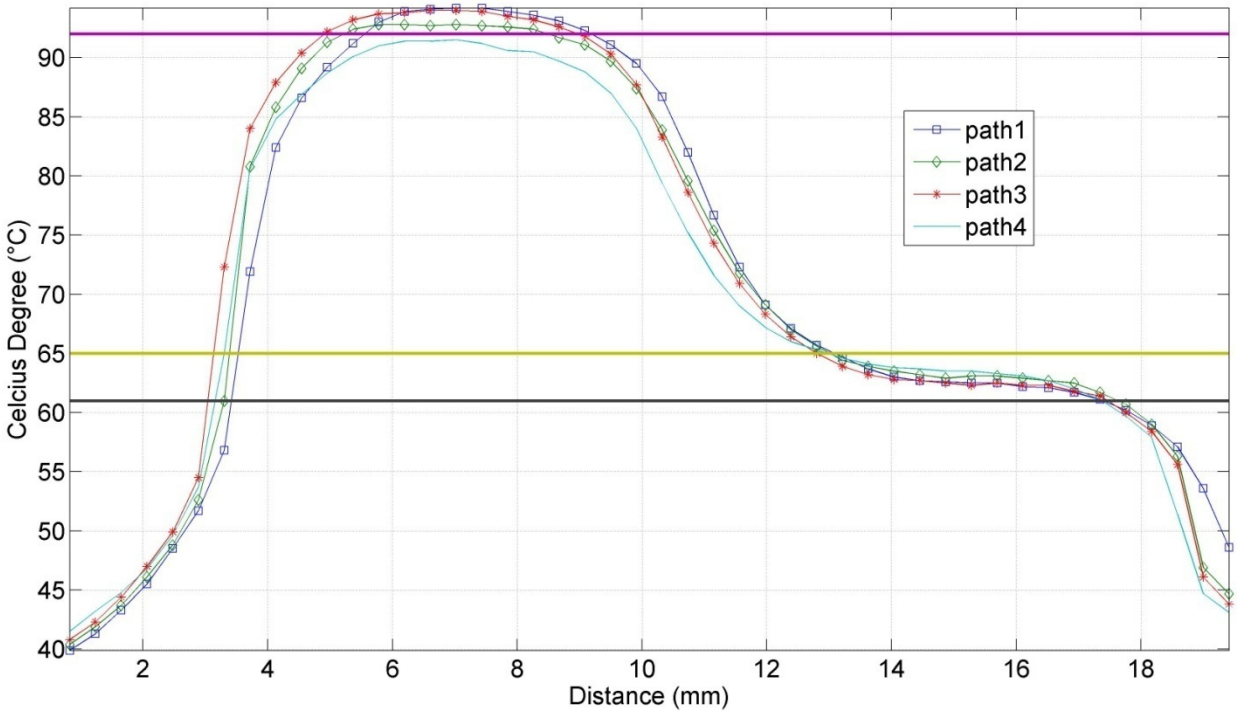

Figure 4.18: Temperature distribution of the four paths defined from denaturation to renaturation shown in Figure 4.15.

4.6.2. IR Camera Experiment on A 96 CFPCR Array

From the previous IR camera experiment results, the multiple temperature zones of a column device including eight CFPCRs could be achieved precisely and simultaneously. Another experiment was extended from the previous results to understand the temperature distribution of a polycarbonate 96 CFPCR array on the multi-zone thermal system. A polycarbonate 96 CFPCR array was attached to the eighteen copper strips of the multi-zone thermal system using thermal double-sided tape and the 96 CFPCR device holder, and its temperature distribution was investigated by an IR camera. Figure 4.19 (a) shows the IR camera image of the polycarbonate 96 CFPCR array and Figure 4.19 (b) shows the converted thermal contours using Matlab. The temperature distribution was not uniform during the experiment and the lowest renaturation temperature achieved was 68°C, 5°C higher than the target temperature. The reasons behind the nonuniform temperature distribution in the 96 CFPCR array might be due to poor attachment

between the copper strips and the polycarbonate devices, warm air accumulated around the copper strips lowering the cooling capability, and the high thermal capacitance of the copper strips. Although thermal double-sided tape and the 96 CFPCR array holder were used to ensure the attachment, but a large area device like a 96 CFPCR array was difficult to have perfect attachment with eighteen solid copper strips. The warm air was accumulated around the copper strips, which lowered the cooling capability due to the lower natural convection and became a source of thermal cross-talk from high temperature zone to low temperature zone. The large thermal capacitance of the copper strips required significant amount of energy to be pumped from the heaters and made the heaters another path for heat to warm the air around the copper strips.

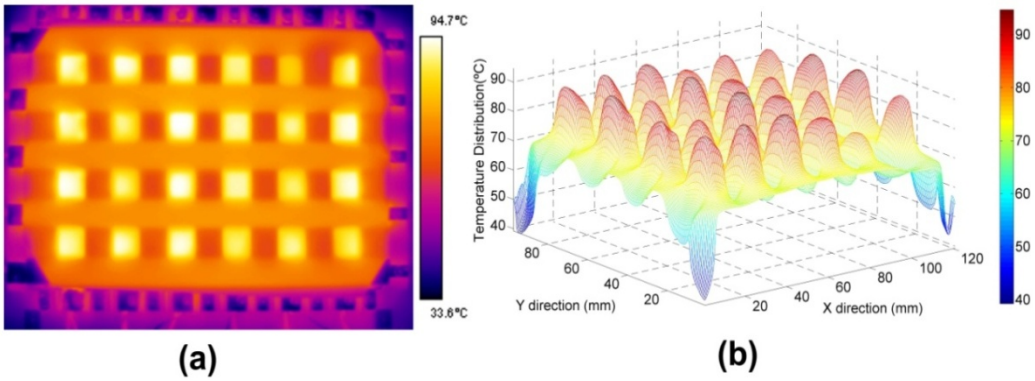

Figure 4.19: (a) The IR image of a polycarbonate 96 CFPCR array (b) The temperature distribution of a 96 CFPCR array converted from the IR image.

4.7. Biochemical Experiments

4.7.1. Chemical Sample Preparation

The DNA template was a 48 kbp λ-DNA c1857Sam7 (USB, Cleveland, OH) target and six different DNA fragments from 99 bp, 125 bp, 150 bp, 200 bp, 500 bp, and 997 bp were designed to be amplified. To generate the six different DNA fragments from the same source template, a common forward primer and six different reverse primers were designed (Integrated

DNA Technologies, Coralville, IA). Table 2 lists the size of the amplicon, corresponding renaturation temperature, and the primer sequence for each fragment.

Table 4.2: The renaturation temperature and primer sequence for six different amplicons.

Forward primer sequence: 5- GAT GAGTTC GTGTCC GTA CAA CTG G -3		
Amplicon Size	Renaturation Temperature (°C)	Primer Sequence
99	63	5- GAC GGG CAATCA GTT CAT CTT TCG -3
125	65	5- GTT CAGTTG TTC ACC CAG CGA GCG G -3
150	69	5- TCG TCC CCGTCA GGCTGA CAT CAC G -3
200	62	5- GTC ATC AAG CTC CTC TTT CAG CTC T -3
500	55	5- GGTTAT CGA AAT CAG CCA CAG CGC C -3
997	68	5- GTA CCT TTG TCT CAC GGG CAA CCT G -3

The PCR cocktail contained 10 mM Tris-HCl (PH 8.3), 1.5 mM $MgCl_2$, 50 mM KCl (USB, Cleveland, OH); the concentrations of nucleotides was 200 μM (USB, Cleveland, OH), the template was 4.6 ng/μL, each forward and reverse primer was 0.2 μM, bovine serum albumin (BSA) was 0.5 μg/μL, and *Taq* DNA Polymerase was 0.1 units/μL (USB, Cleveland, OH). This DNA cocktail was amplified in a bench top thermal cycler to validate the composition and temperature. The cycling conditions were 2 min at 94°C for preheating, 7 min at 72°C for a final extension, and 20 cycles consisting of denaturation for 30 s at 95°C, renaturation for 30 s at specific temperature for different size DNA fragment (Table 2), and extension for 40 s at 72°C. The total time for this amplification process on a benchtop PCR thermal cycler was 1.5 h.

4.7.2. Multiple CFPCR Experiments Using a Column of Devices

A column of devices composed of eight CFPCRs was used to demonstrate the potential for multiple amplifications. Before attaching the column of devices to the multi-zone thermal

system, capillaries (1543, Nature Peek Tubing, Upchurch, Oak Harbor, WA) were inserted into the reservoirs as inlet and outlets for DNA cocktail with Epoxy (Devcon, Danvers, MA) as shown in Figure 4.20. Then the column of devices was attached to the seven copper strips using thermal double-sided tape as shown in Figure 4.13. A syringe pump (PHD 22/2000, Harvard Apparatus, Holliston, MA) with a multiple syringe rack was used to inject multiple DNA cocktails into the devices with a flow velocity of 1 mm/s. The amplicons were collected from the outlet capillaries, mixed with 1X Blue/Orange Dye (Promega, Madison. WI), and injected into an agarose gel (Bio-Rad, Herculus, CA) for electrophoresis. The product was imaged using a Gel Logic 200 Imaging System (Kodak, New Haven, CT) with UV light. Each resultant band was evaluated with the ImageQuant software (Amersham Biosciences, Piscataway, NJ). Only five different DNA fragments were successfully amplified and the results are shown in Figure 4.21. The M in the Figure 4.21 is the marker to show the amplicons in correct size and channel 1 to channel 8 show the amplification results from eight different CFPCRs in the column of devices. The failure of the 997 bp DNA amplification might be due to insufficient time for successful amplification at a flow velocity of 1 mm/s or the resolution of the amplicon detection technology was not high enough. In Figure 4.21, the amplification efficiency of each of the CFPCRs was different, which might be attributed to many factors like microfabrication variation, DNA cocktail variation, pipetting process, or the analysis.

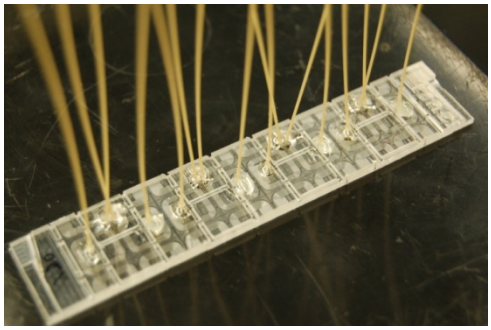

Figure 4.20: A column of devices with eight CFPCRs with capillaries inserted and glued.

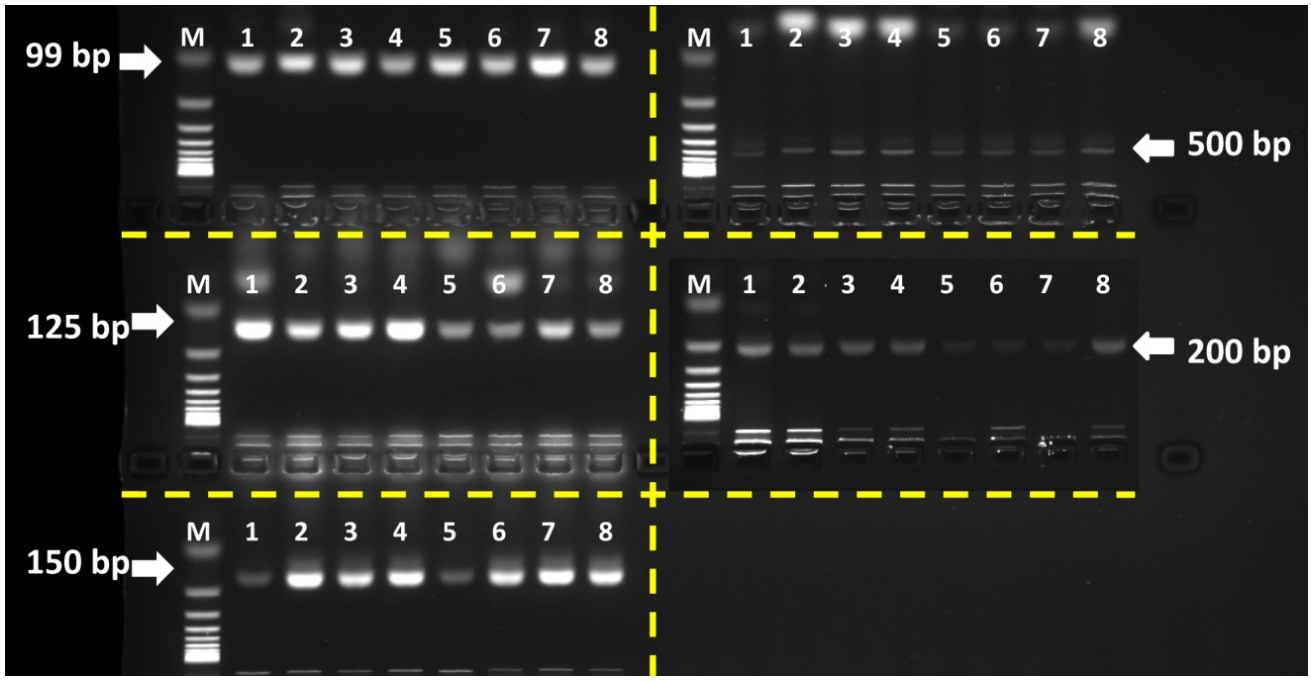

Figure 4.21: The experimental results of five different amplicons from a column of devices, the amplicons included 99 bp, 125 bp, 150 bp, 200 bp, and 500 bp.

4.7.3. Multiple CFPCR Experiments Using a Row of Devices

The previous experiments demonstrated the parallel amplifications of identical DNA fragments. To amplify different DNA fragments simultaneously, a row device included twelve CFPCRs, six for twenty cycles and six for twenty five cycles, was used. In this experiment, six 25-cycle CFPCRs were used and each of them amplified one size DNA fragment. Figure 4.22 shows the row of devices with glued capillaries for the input and output of the PCR cocktail. The row of devices was attached to the copper strips by using thermal double-sided tape and thirteen copper strips including one copper strip for extension, six copper strips for denaturation, and six for renaturation (Figure 4.23) were used in the experiments.

The same DNA cocktail composition and preparation described in Section 4.7.1 was used. A syringe pump with a multiple syringe rack was used to inject the DNA cocktail into the CFPCRs simultaneously at a flow velocity of 1 mm/s. After going through 25 cycles of

microchannels, the amplicons were collected and analyzed. The experimental result are shown in Figure 4.24, with six different amplicons successfully amplified.

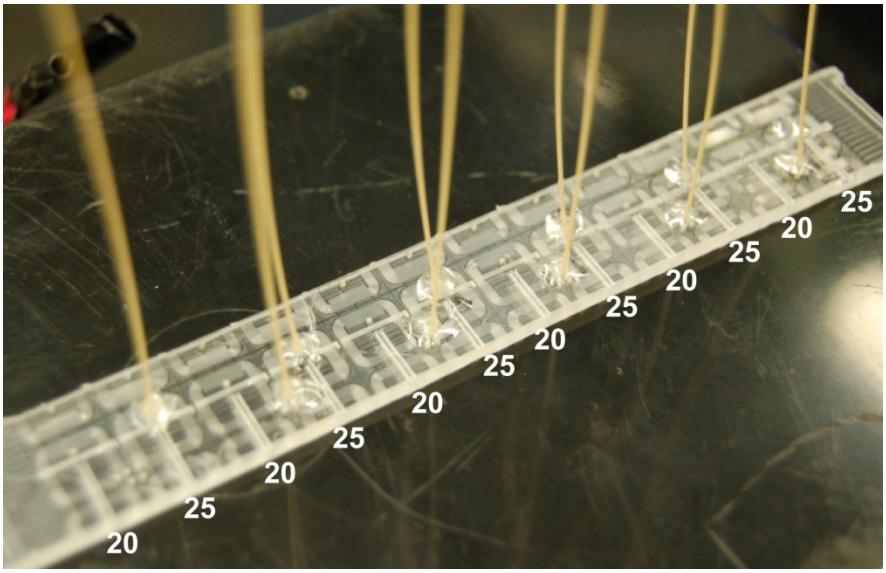

Figure 4.22: A row of devices including twelve CFPCRs, six with 20 cycles and six with 25 cycles, was used to demonstrate multiple amplifications in different DNA fragments simultaneously.

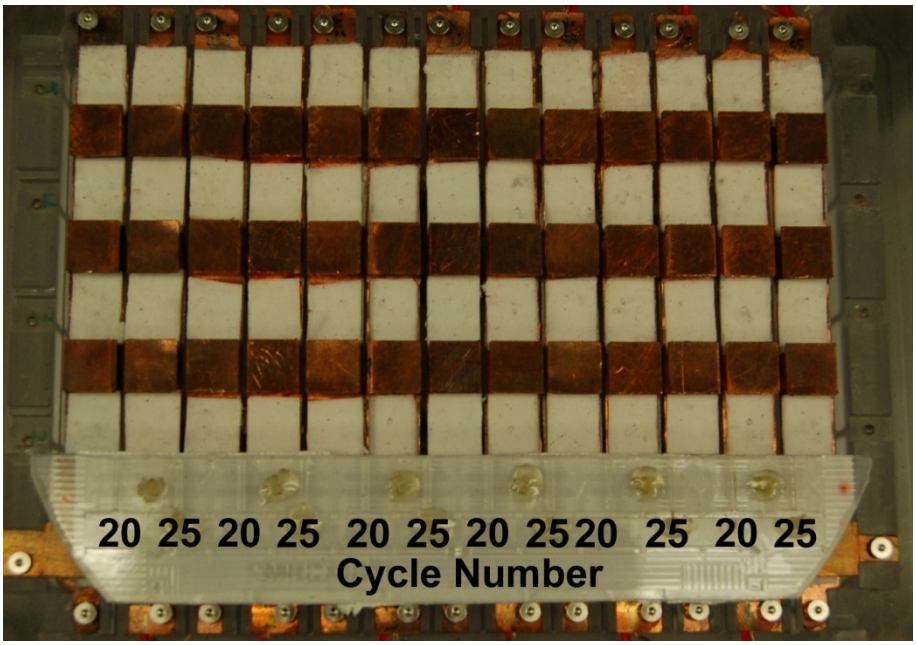

Figure 4.23: A row device with twelve CFPCRs was attached on the multi-zone thermal system for experiment.

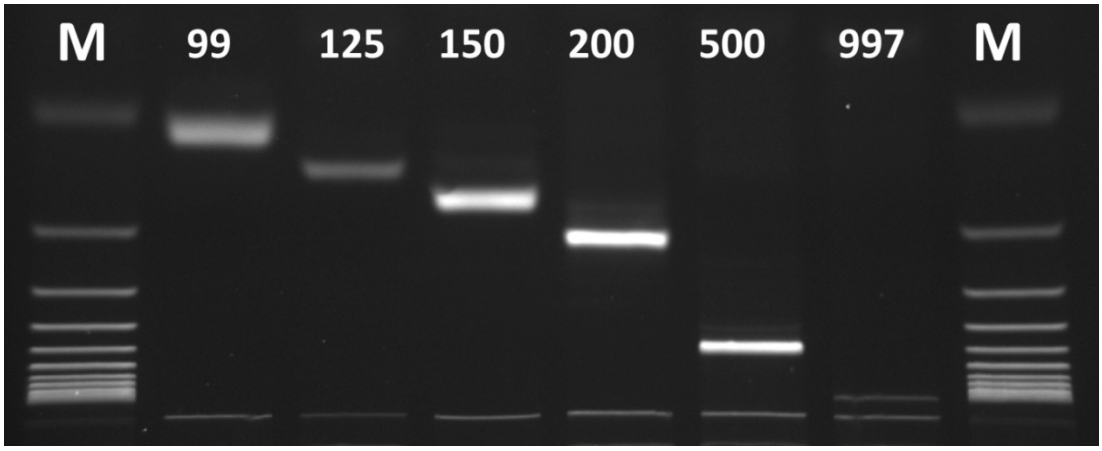

Figure 4.24: The experiment results of six different amplicons from a row device.

4.8. Conclusions

A multi-zone thermal system was designed and developed to support the requirement for multiple temperature zones in a microfluidic device for chemical reactions either in parallel or in sequence. A 96 CFPCR array was designed, fabricated, and described in Chapter 3 and 288 distinct steady-state temperature zones were needed. To realize the thermal requirement of a polycarbonate 96 CFPCR array, eighteen copper strips were used including seven copper strips for the renaturation zone, six copper strips for the denaturation zone, and five copper strips for extension. Finite element analysis (FEA) was used to analyze the thermal cross-talk between temperature zones and the lowest renaturation temperature achievable was 62°C. To demonstrate the capability for multiple amplifications, both a column of devices including eight CFPCRs and a row of devices including twelve CFPCRs, were used. An infrared camera was used to investigate the temperature distribution of a column of devices with denaturation at 95°C, renaturation at 63°C, and extension at 72°C. Three discrete and uniform temperature zones were defined for each CFPCR on a column of devices with ±1°C in renaturation and extension and ±2°C in denaturation. Biochemical experiments were realized on a column of devices and successfully amplified five different DNA fragments from 99 bp to 500 bp. Another multiple

amplification experiment was realized on a row of devices to amplify six different DNA fragments with six 25-cycle CFPCRs, simultaneously.

An infrared camera was used to investigate the temperature distribution of the 96 CFPCR array on the multi-zone thermal system. These was a nonuniform temperature distribution due to thermal cross-talk between the temperature zones. The lowest temperature achievable in the renaturation zone was 62°C in the simulations, but the actual temperature was 68°C since the constant convection coefficient in the simulation did not account for the actual smaller convection coefficient when the warm air was accumulated around the copper strips. Poor attachment between the copper strips and the polycarbonate device, warm air accumulated around the copper strips, and the flow of heat from the copper strips into the ambient air might be responsible for the nonuniform temperature distribution.

CHAPTER 5: DESIGN CONSIDERATION FOR A POLYCARBONATE REAGENT DISTRIBUTION DEVICE

5.1 Motivation

The 96 well CFPCR array described in Chapter 3 was designed to amplify 96 DNA fragments simultaneously. Although commercial reagent distribution equipment is available (Figure 1.5), it is incompatible with this 96 well CFPCR array. A new reagent distribution module is required. The reagent distribution module should evenly distribute the chemicals into each CFPCR in the array and customize the number of inputs from 1 to 96 depending on the array requirements. This reagent delivery device will act as an interface between the operator and the 96 CFPCR array. A typical example was the matrix micro PCR developed by using multiple layers of PDMS to reduce the number of pipetting steps; with 41 pipetting steps used for 400 micro reactors [Liu et al., 2003]. Furthermore the reagent delivery module can incorporate sample preparation functions, like cell capture from the blood, call lysis to extract the required DNA templates, and mixing with other chemicals as a fully functional device for sample preparation before the 96 CFPCR array.

A passive alignment structure and thermal management will be studied. The purpose of the passive alignment structure is to align two plates in a vertical modular approach. The thermal management is used to ensure that the distance between two plates is sufficient to avoid disturbing the thermal performance of the 96 CFPCR array in the lower layer.

5.2 Passive Alignment Structures

5.2.1 Motivation

To successfully integrate a reagent delivery module with a 96 CFPCR array in a modular approach, alignment between the two plates is critical to prevent significant leakage of biochemical sample. If the mismatch between two connecting channels is larger than 13% of the

diameter of the connecting channel [Rani et al., 2006], dead volume with recirculation might cause a problem such as cross contamination. A passive alignment structure was developed to answer this demand and ensure that the path for reagent transportation was smooth.

5.2.2 Review of Passive Alignment and Interconnectors

Passive alignment structures were developed for polymer microfluidic microsystems [You et al., 2006]. Screw theory, a kinematic approach, was used to ensure that the design of the passive alignment structures appropriately constrained all of the degrees of freedom except movement between the two plates without generating any unnecessary internal stress once assembled. The passive alignment structures included three kinematic pairs of passive alignment features, a v-groove and a hemispherical post. Two mold inserts were fabricated containing either the v-groove or the hemispherical post, by micromilling. The passive alignment structures on the mold inserts were transferred to the polymer substrate by hot embossing. The accuracy of the alignment of the two assembled plates was estimated by measuring the offset of three alignment standards embedded in the two plates. The relative offset of the alignment marks was measured using optical microscopy, and mismatches between 28-70 μm were observed.

A passive alignment structure was designed based on the principles of elastic averaging [Slocum et al., 2003]. Elastic averaging requires a large number of contact points spread out over a broad region when two surfaces must be assembled accurately under a large load, instead of the rigid body assumption used in screw theory. The alignment structure included a groove and a pyramid (convex) and both alignment features were fabricated in silicon wafers by Potassium Hydroxide (KOH) etching. Experiments using three sets of passive alignment structures between the plates demonstrated that the passive alignment structures could reliably and repeatedly achieve submicro accuracy between multiple plates.

A long assembly loop for assembling multiple layers of poly-dimethylsiloxane (PDMS) in a stack was used by establishing a kinematic coupling system between an alignment plate and a base [Trinkle et al., 2006]. The PDMS mold was fixed on a stationary base plate while the alignment plate was assembled with the stationary base plate via v-grooves and sphere-tipped posts. PDMS was poured into the enclosed space between the mold and two plates to encase the microdevice. The alignment accuracy for the PDMS system was determined by the macro kinematic coupling and a mismatch of less than 5 μm was achieved.

Gonzalez et al. [Gonzalez et al., 1998] used compression seal fittings to supply self-alignment and interlocking functions between two silicon wafers. Micro-finger joints were realized by fabricating a set of periodic, vertical grooves in one substrate while grooves with the opposite polarity were made in the other. The two substrates were assembled and the friction between two sets of micro-finger joints created a locking mechanism to hold the two pieces together. A 110-oriented silicon wafer was etched by KOH to make the interlocking alignment structures between the two silicon wafers. An O-ring was used as a gasket to prevent leakage. An extensive study using a similar approach for passive alignment structures, assembly, and interconnection was also reported [Gray et al., 2004]. The shape of the passive alignment structures was redesigned from finger-like to notched cylinders. The fabrication process was still based on silicon etching and the assembly force between the layers was the friction force between the contact surfaces.

A microfluidic interconnect was developed for glass and plastic substrates [Puntambekar et al., 2002]. A vertical guide tube was embedded in the glass or polymer layers during fabrication. The sample-carrying capillary was inserted into the guide tube and had good alignment with reservoirs or microchannels on the substrate. Two types of interconnects were

studied; the first one was a series assembly, with a interconnect between a capillary and a microchannel. The second was a parallel assembly, consisting of two series assemblies, with two interconnects on the same substrate, one on the top of the substrate and the other on the bottom of the substrate, and a microchannel to connect two interconnectors. A numerical simulation was used to estimate the pressure drop and the dead volume due to the mismatch.

An interconnect was fabricated by using a metal guide wire and a Teflon tube [Pattekar et al., 2003]. The microfluidic device was fabricated on a silicon substrate and covered by glass. The inlet and outlet were drilled through the glass before anodic bonding to enclose the microchannel. A metal wire and Teflon tube were inserted into the inlet/outlet after enclosing the microchannel and the bottom end of the Teflon tube was melted and deformed, to form an undercut shape in the microchannel due to the high temperature applied on the silicon substrate, 380 ºC. The metal wire and Teflon tube were pulled and the deformed Teflon tube would block the inlet/outlet from the inside of the microchannel. A high temperature epoxy was applied on the top outside surface of the inlet/outlet to seal the gap between the Teflon tube and the inlet/outlet without flow into the microchannel. A sleeve was applied over the dried epoxy to tighten the interconnect. A leakage experiment was carried out in a water bath, and pull-out testing was used to estimate the failure force for the interconnect at room temperature and 275ºC.

Other work on passive alignment structures and interconnects, using similar ideas to the examples described above have been described by several groups [Gray et al., 1999, Nittis et al., 2001, Igata et al., 2002, Friedrich et al., 2005, Brecher et al. 2006].

5.2.3 The Original Passive Alignment Structure Prototype

To realize a modular microfluidic system using polymer substrates for mass production, the requirements for a passive alignment structure were for simple geometry, a simple fabrication

process, acceptable accuracy, and transferability to any substrate. Screw theory, was used to design a passive alignment structure to achieve an acceptable alignment accuracy between multiple plates. Screw theory uses wrench and twist matrices to represent the constraining forces/moments and instantaneous motions to analyze the state of constraint of modules with assembly features. A v-groove and a hemisphere-tipped post were selected as the passive alignment structure and characterized mathematically using screw theory [You et al., 2006].

Figure 5.1 shows the configuration of the passive alignment structures which included a triad of v-grooves and a hemisphere-tipped posts. Three pairs of passive alignment structures were required to assemble two layers with exact constraint. One layer of the test bed had three v-grooves and the other had three complementary hemisphere-tipped posts. Each pair of passive alignment structures had two point contacts between the v-groove and hemisphere-tipped post; the alignment would be affected if the hemisphere-tipped post was deformed resulting in a line or surface contact. The dimensions of the v-grooves were designed of 2 mm wide, 3 mm long, and 1 mm deep with a 45º angle reverse pyramid shape in the substrate. The hemisphere-tipped posts were designed of 1 mm in diameter and 925 μm high from the surface of the substrate. Figure 5.2 shows the configuration of the three pairs of passive alignment structures. Passive alignment structure 1 and passive alignment structure 2 were on the same line and both were designed to constrain the X direction. The axis of passive alignment structure 3 was normal to the line passing through the axes of passive alignment structures 1 and 2. Passive alignment structure 3 was designed to constrain motion in the Y direction. The Z direction was assumed constrained by the assumption of contact between all three pairs. And the rotations along the three axes are constrained by three pairs of passive alignment structures.

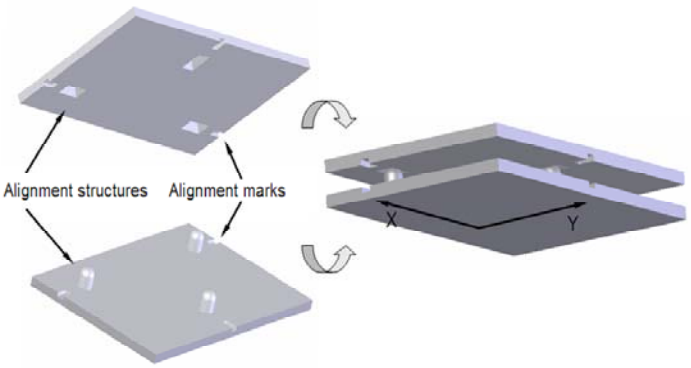

Figure 5.1: Passive alignment of two modules, using a v-groove and a hemisphere-tipped posts.

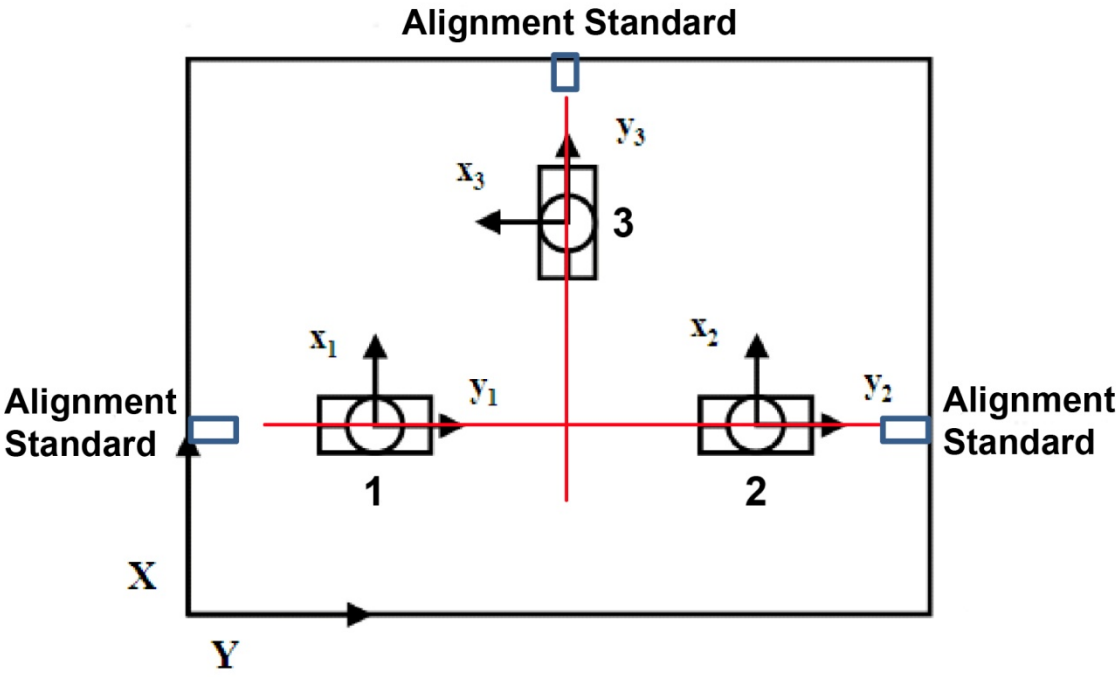

Figure 5.2: The configuration of three pairs of passive alignment structures and three alignment standards on a substrate.

To fabricate the v-grooves and hemisphere-tipped posts on a polymer substrate, micromilling (Kern MMP – Microtechnic, Murnau-Westried, Germany) and hot embossing (Jenoptik HEX 02,Jena, Germany) were used. A ball-end milling bit was used to fabricate the hemispherical recesses and a milling bit with a 90º cutting angle was used for a standing

pyramidal structure on a brass substrate. Figure 5.3 shows SEM images of the standing pyramidal structure and the hemispherical recess on the brass mold insert.

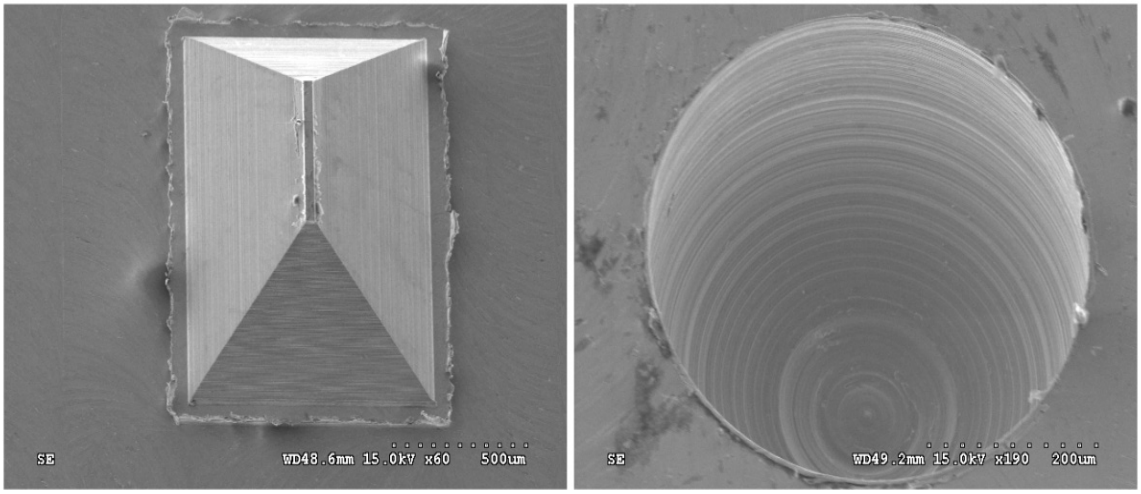

Figure 5.3: (a) The standing pyramid structure on the brass mold insert for the v-groove on the polymer; (b) The hemispherical recess on the brass mold insert for the hemisphere-tipped post on the polymer substrate.

5.2.4 Experimental Results with the Original Prototype Passive Alignment Structures and Motivation

A test bed was designed and fabricated to assess the accuracy of alignment with the polymer alignment structures (Figure 5.2). There were three pairs of passive alignment structures and three pairs of alignment standards on the two substrates. One plate had three v-grooves and three alignment standards and the other plate had three hemisphere-tipped posts and three alignment standards. When the two plates were brought together and glued using Epoxy, the misalignment between the two plates was estimated from the mismatch between the two alignment standards on the upper and lower plates using an optical microscope (MM-22, Nikon Corp., Kawasaki, Japan). The mean mismatch between the two plates was between 28 μm to 70 μm; each polycarbonate sample had two plates assembled together and measurements were repeated three times for each set of alignment standards [You et al., 2006].

This misalignment was primarily contributed by incomplete filling of the polymer into the hemispherical recesses on the brass mold insert. Hemisphere-tipped posts with a height of 798 μm was reported [You et al., 2006]. Figure 5.4 shows a hemisphere-tipped post with a non-uniform radius which degraded the alignment accuracy. When one of the hemisphere-tipped posts was shorter, longer, or deformed, there were more or less than the designed six-point contacts between the two plates, leading to a mismatch of the assembly. To achieve a mismatch less than 65 μm, 13 % of a 500μm diameter reservoir, better polymer filling during hot embossing was needed. This could be achieved by either improving the hot embossing process or a better design of the hemispherical recess.

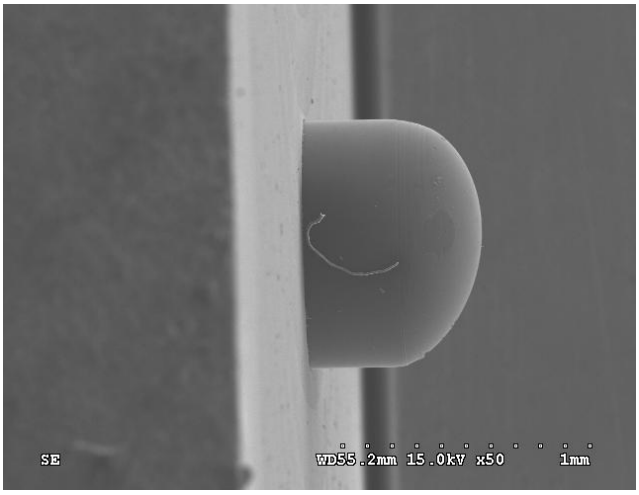

Figure 5.4: The shorter hemisphere-tipped post due to the incomplete filling of the polymer [You et al., 2006].

5.3 Modified Passive Alignment Structures

5.3.1 Ideas and Theoretical Background behind the Modified Passive Alignment Structure

To improve the filling of the hemispherical recess and the alignment accuracy between upper and lower plates, a convex annular ring was added around the hemispherical recess on the mold insert (Figure 5.5). A concave annular ring was also used (Figure 5.5) as an opposite

experiment for comparison and is described in Appendix B. The original hemispherical recess and the hemispherical recess with the convex annular ring are the main focus in this section.

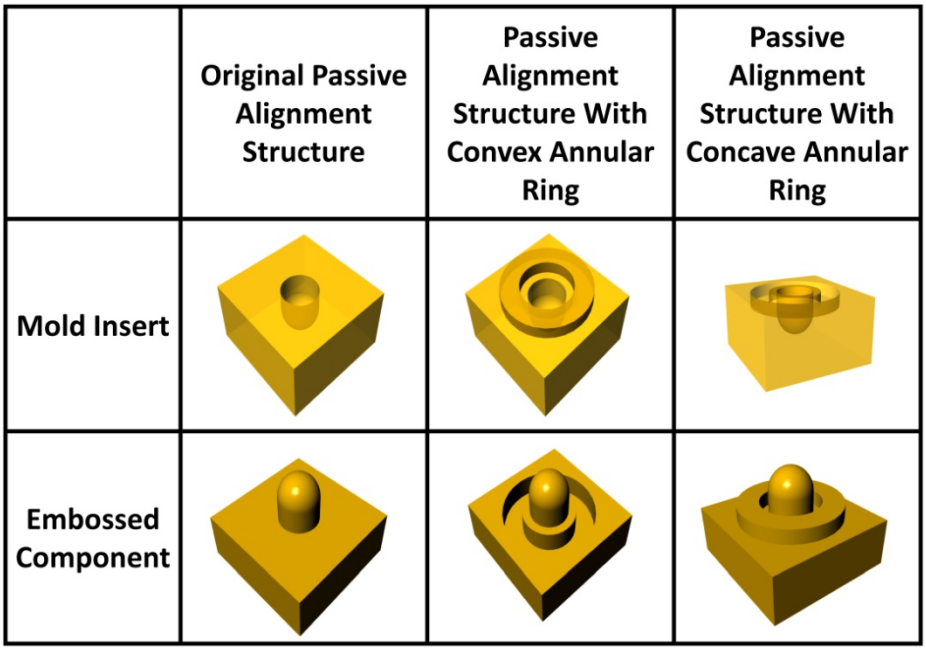

Figure 5.5: The shapes of original hemispherical recess, hemispherical recess with convex annular ring, and hemispherical recess with concave annular ring on the mold insert and after hot embossing.

During the hot embossing process, the polymer was heated above its glass transition temperature where it behaved as a viscoelastic/viscous flow depending on the excess temperature above its glass transition temperature. The melted polymer came from the surrounding volume to fill the recess and the final filling result depended on the embossing temperature, embossing pressure, embossing time, and the design of the microstructures. The original hemispherical recess was a simple negative pattern and they are difficult to fill completely [Scheer et al., 2001, Scheer et al., 1998] because the melted polymer has to travel a long distance from the surrounding area. A configuration used to estimate the time to completely fill the cavity on a mold insert is shown in Figure 5.5 and Equations 5.1 and 5.2 were used to estimate the filling time. The configuration is a two-dimensional model but it can simply demonstrate the

relationship between the polymer filling time and a simple geometry [Torres, 2003]. The assumptions are that the melted polymer is an ideal viscous liquid, the polymer melt is incompressible, the width of the mold insert is much larger than the thickness of the polymer, no air is trapped in the cavity, and there is no stick-slip effect at the interface between the polymer and mold insert.

$$t_f = \frac{\eta_0 s^2}{2p}\left(\frac{1}{{h_f}^2} - \frac{1}{{h_0}^2}\right) \quad 5.1$$

$$h_f = h_0 - \frac{W \times D}{s} \quad 5.2$$

In Equation 5.1, t_f is the time required to replace a given amount of polymer of height h(t), η_0 is the polymer viscosity, s is the width of the mold insert, p is the embossing pressure, h_f is the final thickness of the polymer, and h_0 is the initial thickness of the polymer. In Equation 5.2, W is the width of the cavity, and D is the depth of the cavity.

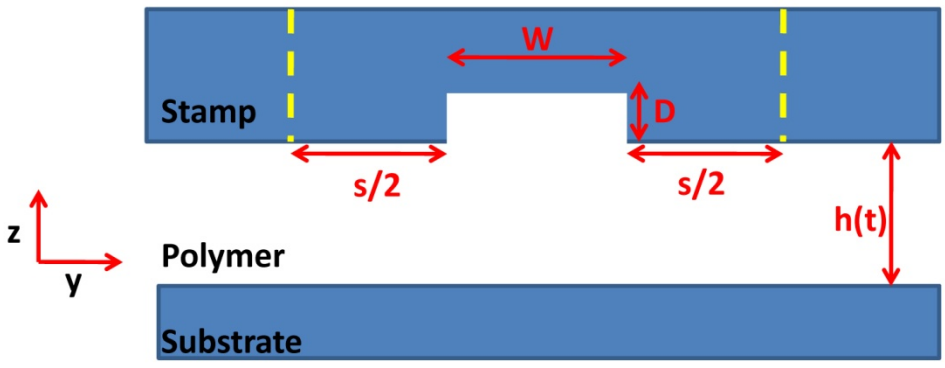

Figure 5.6: The configuration of the model used for Equation 5.1.

Equation 5.1 helped estimate the time required for the melted polymer to completely fill the cavity on the mold insert. The time was used as an index to determine the difficulty of polymer filling for different layouts. Figure 5.7 (a) shows the cross-section of the original hemispherical recess on a mold insert; the width of the recess was 1 mm, the depth was 1 mm,

and the melted polymer flowed from the surrounding area as shown by the arrow. The width of the mold insert was assumed to be 100 mm and the initial thickness of the polymer was 5 mm. The final thickness was calculated using Equation 5.2 and the final thickness was used in the Equation 5.1. Since the model in Figure 5.7 (a) was symmetric, only half the pattern was considered. The final thickness of the original recess was 4.989 mm from Equation 5.2 and the distance the melted polymer flowed from the edge of the plate to the center of the recess. The estimated time was 1.103×10^{-4} seconds if the viscosity was assumed to be 2648 Pa-s and the pressure was assumed to be 3×10^{6} Pa.

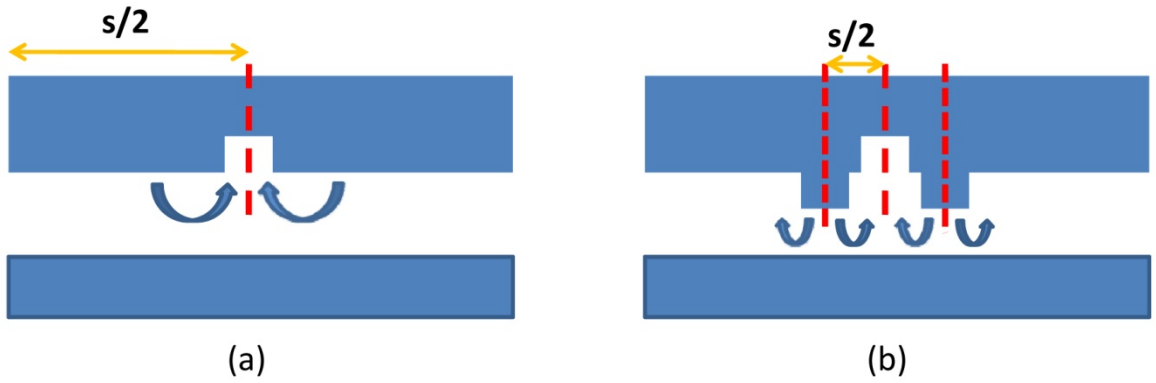

Figure 5.7: (a) The cross section view of the recess (b) The cross section view of the recess with a convex annular ring.

To reduce the time required to completely fill the cavity, several approaches could be used, such as reducing the viscosity of the melted polymer by increasing the temperature, increasing the embossing pressure, increasing the film thickness, decreasing the ratio of cavity volume to stamp width, and decreasing the flow distance of the melted polymer [Heyderman et al., 2000]. From Equation 5.1, the polymer flow distance strongly influences the required time for filling the cavity ($t_f \propto s^2$); shorter flow distances could significantly reduce the filling time. A convex annular ring was added around the hemispherical recess to produce a shorter flow

distance for the melted polymer and its cross-sectional view is shown in Figure 5.7 (b). The flow distance of the melted polymer, the top surface of the convex structure to the bottom of the recess, was much shorter in Figure 5.7 (b). In the case of a hemispherical recess with a convex annular structure, the final thickness was 3.667 mm from Equation 5.2 and the estimated time was 5.459×10^{-6} seconds when the flow distance was 0.6 mm from the center of the convex structure to the center of the recess. From the simple 2-D model, the time to completely fill the hemispherical recess required 1.103×10^{-4} seconds and the required time for the recess with a convex annular structure was 5.459×10^{-6} seconds, a factor of 20 less. This simple estimate supported the idea of adding a convex annular ring around the hemispherical recesses to yield better filling performance.

5.3.2 Comparison between the Original and Modified Convex Passive Alignment Structures

5.3.2.1 Comparison of the Polymer Filling Phenomena between The Original and Modified Prototypes of Passive Alignment Structures

Before the alignment accuracy experiments with using the modified hemisphere-tipped posts, a hot embossing experiment was used to validate the idea of using the convex annular structures to improve polymer filling. A brass mold insert was designed with 6 different layouts of hemispherical posts on it (Figure 5.8 (a)). This mold insert had one original post pattern and five different modified post patterns, in order to assess the impact of the convex annular structure on embossing hemisphere-tipped posts. The five alternative modified post designs incorporated different distances (100 μm, 200 μm, 300 μm, 400 μm, and 500 μm) between the inner walls of the convex annular structure and the edge of the hemispherical structures, shown in the area with red color in Figure 5.8 (b). The alignment structures were located at three radial locations (12

mm, 24 mm, and 36 mm) from the substrate center to evaluate whether the distance affected polymer filling.

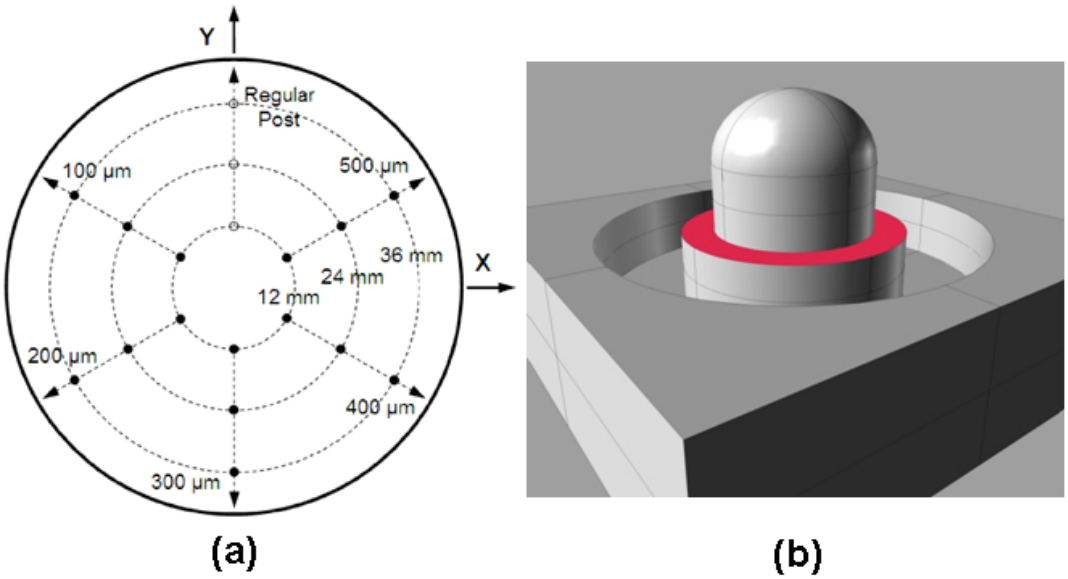

Figure 5.8: (a) A mold insert with 6 rows of hemispherical recesses with different gap distances between the hemispherical recess and the inner wall of the standing annular wall (b) The hot embossed hemispherical post and the area in red color corresponded to the different gap distance between hemispherical recess and the inner wall of the standing annular wall.

Table 5.1 lists the hot embossing conditions for the mold insert. The polymer filling of the hemispherical recess was evaluated by measuring the heights of the embossed posts with a Microscope (MM-22, Nikon Corp., Kawasaki, Japan). Height was measured by focusing alternately on the top of the posts and the adjacent substrate surface. Ten samples were used to compare the different layouts. Figure 5.9 shows the images of the top surface of the hemisphere-tipped posts observed from the microscope. Since the hemispherical recess was micro milled on the brass substrate, circular machining marks were left in the recess (Figure 5.3 (b)). The observation of the tool marks on the polymer hemispherical post was used as an indicator of the complete filling of those posts.

Table 5.1: The hot embossing conditions used for hemisphere-tipped post study.

	Molding Temp (°C)	**Embossing Force (kN)**	**Holding Time (s)**	**Demolding Temp (°C)**	**Embossing Velocity (mm/min)**
Post	190	24	120	140	0.5

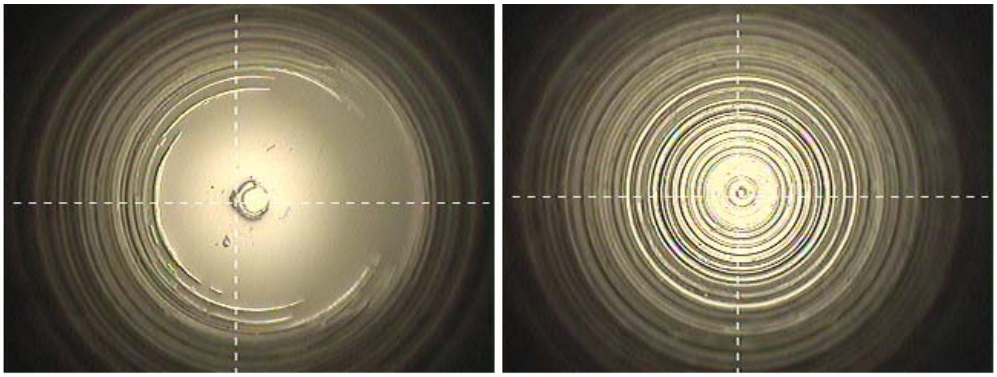

Figure 5.9: Images of top surface of hemisphere-tipped post after hot embossing. The circular patterns were the tool marks from the milling bit. (a) Incomplete filling was shown in complete circular tool marks (b) Complete filling with complete tool marks.

Figure 5.10 shows SEM images of the hemisphere-tipped posts with different gap distances from 0 to 500 µm. There was no significant difference between the five configurations for the modified posts. The average height of the five modified configurations were 922.9 µm, 925.2µm, 925.6 µm, 925 µm, 923.9µm with variances of ±1.46 µm, ±0.8 µm, ±1.4 µm, and ±2.3 µm, and ±0.8 µm corresponding to gap distances of 100 µm, 200 µm, 300 µm, 400 µm, and 500 µm respectively (Table 5.2). Figure 5.11 shows the mean heights of the original posts and the modified posts with gaps of 100 µm based on the same hot embossing conditions. The unmodified posts had 879, 867.1, and 907.1 µm mean heights with variances of ±13.3, ±18.7, and ±29.0 µm as the distances of the posts from the center increased from 12 to 36 mm. The modified posts with gaps of 100 µm had mean heights of 922.3 ~ 923.9 µm with variances of

±0.9 ~ ±1.9 μm. A 100 μm gap between the inner wall of the dummy annular structure to the edge of the hemispherical recess was chosen as the alignment posts for the alignment accuracy test. The hemisphere-tipped posts with convex annular ring had better filling than the original posts and validated the ideas of adding a convex annular ring to improve the probability of complete filling.

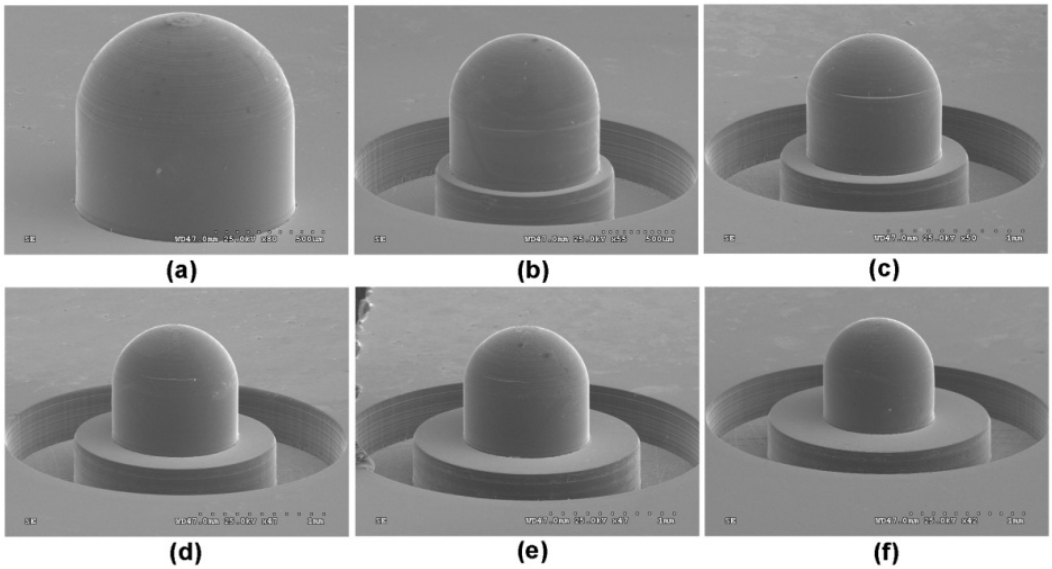

Figure 5.10: SEM images of the hemispherical posts with different gap distances between hemispherical post and the inner walls of the annular rings (a) original post (b) gap distance : 100 μm (c) gap distance : 200 μm (d) gap distance : 300 μm (e) gap distance : 400 μm (f) gap distance : 500 μm

Table 5.2: The average height of the hemispherical posts in terms of either the distance from the center of the substrate or the overall measurements based on 10 samples.

Radical Locations (mm)	**Original**	**100**	**200**	**300**	**400**	**500**
12	879	922.3	924.2	924.7	924.4	923.6
24	867.1	923.9	924.5	925.7	924.3	923.7
36	907.1	922.5	923.7	926.4	926.3	924.3
Mean Height (μm)	884.4	922.9	924.2	925.6	925	923.9

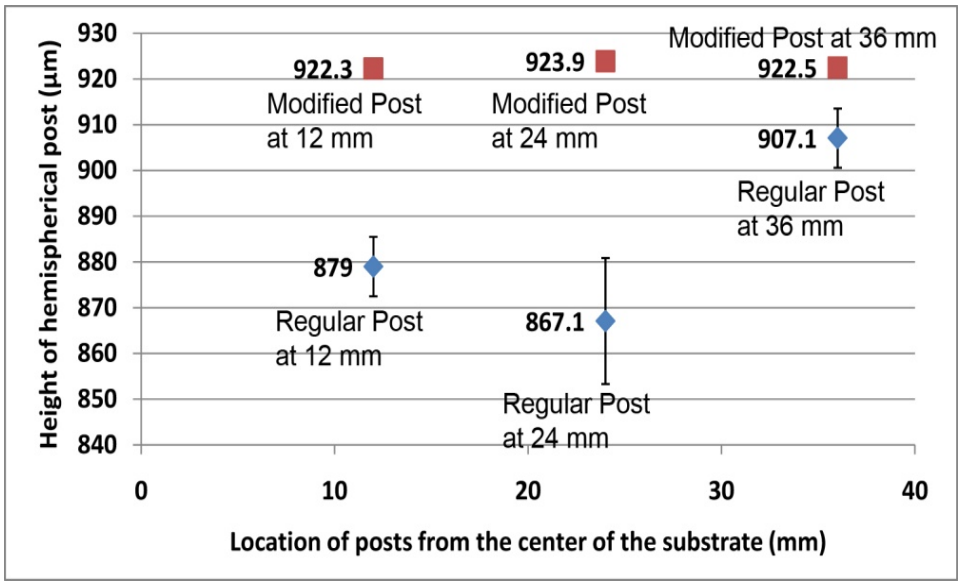

Figure 5.11: The mean heights of the regular posts and the modified posts with gaps of 100 µm at different distances from the center of the embossed parts.

5.3.3 Passive Alignment Structure Accuracy Measurement Using Modified Passive Alignment Structures

5.3.3.1 Accuracy Experiment Preparation

The following experiment was used to demonstrate the improved alignment accuracy between two plates with the modified passive alignment structures. Figure 5.12 shows the standard layout of the two mold inserts used for the alignment accuracy experiment, one had hemispherical recesses with alignment standards and the other one had v-groove structures with alignment standards. Each mold insert had four sets of passive alignment features located at 12 mm, 24 mm, and 36 mm from the center of the substrate; they also had four sets of alignment standards which were located at 18 mm, 30 mm, and 42 mm. The hot embossing conditions for the hemisphere-tipped posts are listed in Table 5.1 and the hot embossing conditions for the v-grooves are shown in Table 5.3. Figure 5.13 shows the SEM images of a v-groove after hot embossing, Figure 5.13 (a) is a top view and Figure 5.13 (b) an oblique view.

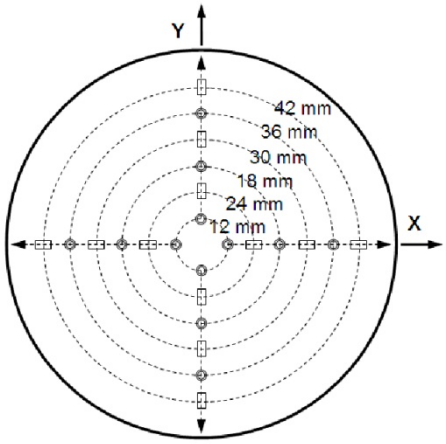

Figure 5.12: The configuration of the mold inserts used for alignment accuracy experiment.

Table 5.3: The hot embossing conditions used for v-groove.

	Molding Temp (°C)	**Embossing Force (kN)**	**Holding Time (s)**	**Demolding Temp (°C)**	**Embossing Velocity (mm/min)**
Post	190	17	90	140	0.5

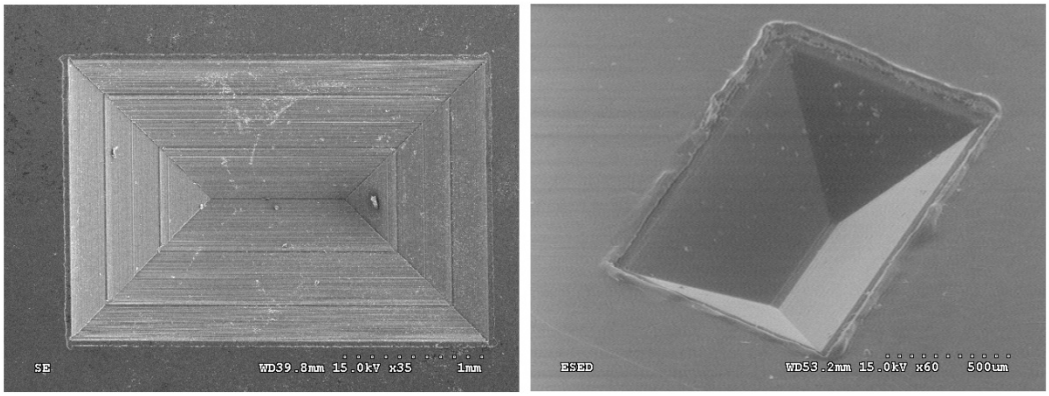

Figure 5.13: SEM images of the v-groove (a) top view, the dimension of the v-groove was 2 mm × 3 mm from the scale bar (b) the oblique view.

Only three passive alignment features, either v-groove or hemispherical post, were selected for the passive alignment accuracy experiment, otherwise there would be over constraint.

Once three hemisphere-tipped posts at the radial locations were selected for an accuracy experiment, the other hemisphere-tipped posts were removed with a razor blade. The assembly of the two plates was easily realized by bringing the two plates together and epoxying them. Before binding, the embossed plates were washed with isopropyl alcohol (IPA) and deionized water (DI), followed by drying with nitrogen gas and baking in an oven at 70ºC for 1-2 hours, to remove any residual dust which might affect the assembly accuracy. After gluing, the device was cut into a square and made the alignment standards exposed for measurement, as shown in Figure 5.14. The cutting surface was polished using different sand papers to make the surface smooth and remove any excess material. Figure 5.15 (a) shows a cross-sectional view of an assembled hemisphere-tipped post and v-groove. Figure 5.15 (b) shows the point contacts between the two passive alignment features after assembly.

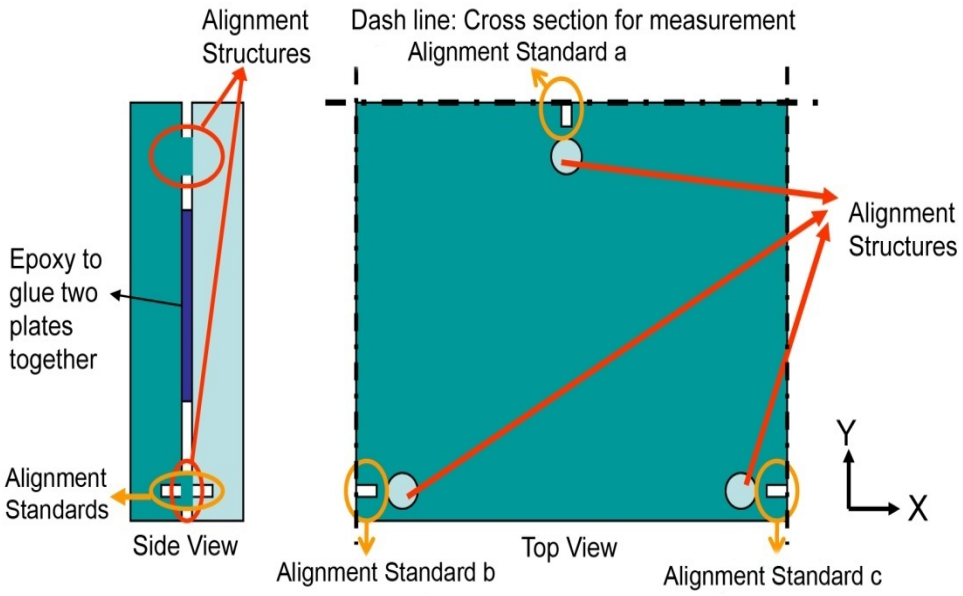

Figure 5.14: The configuration of the alignment structures, for assembling two plates with epoxy. Alignment standards, for precision measurement of the resulting assembly, are also shown.

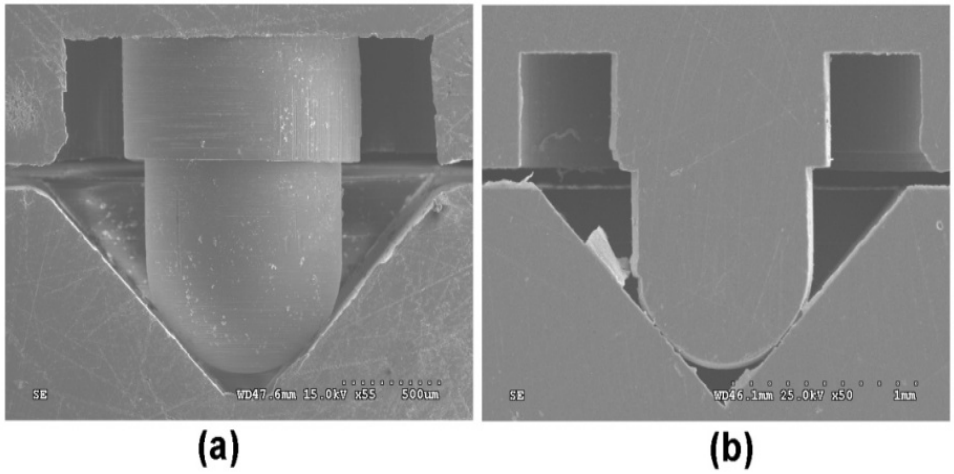

Figure 5.15: (a) Cross-section of the passive alignment structures after assembly (b) Cross-section of the passive alignment structure after assembly and polishing to show the contact points between two passive alignment features.

5.3.3.2 Experiment Results

After assembly, a Microscope (MM-22, Nikon, Japan) with a 10X lens was used to measure the mismatch between the two plates. Nine samples were measured in this experiment. They were categorized into three groups based on the radial location from the substrate center. Three measurements were used for each sample because of the three alignment standards a, b, and c corresponding to three passive alignment features as shown in Figure 5.14. Figure 5.16 shows the images of the alignment standards captured from the microscope. Figure 5.16 (a) shows the worst case in this experiment, a 20 μm mismatch, and Figure 5.16 (b) shows the best case, a 2 μm mismatch. Figure 5.17 shows the measured results of the 9 samples.

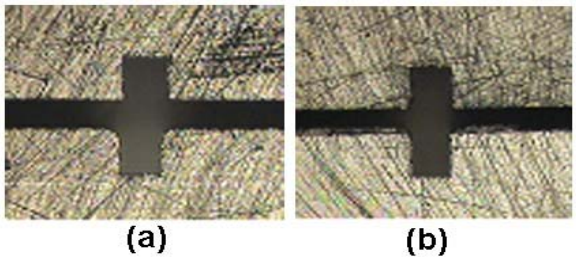

Figure 5.16: (a) The 20 μm misalignment between two polycarbonate plates, and (b) The 2 μm misalignment between two polycarbonate plates.

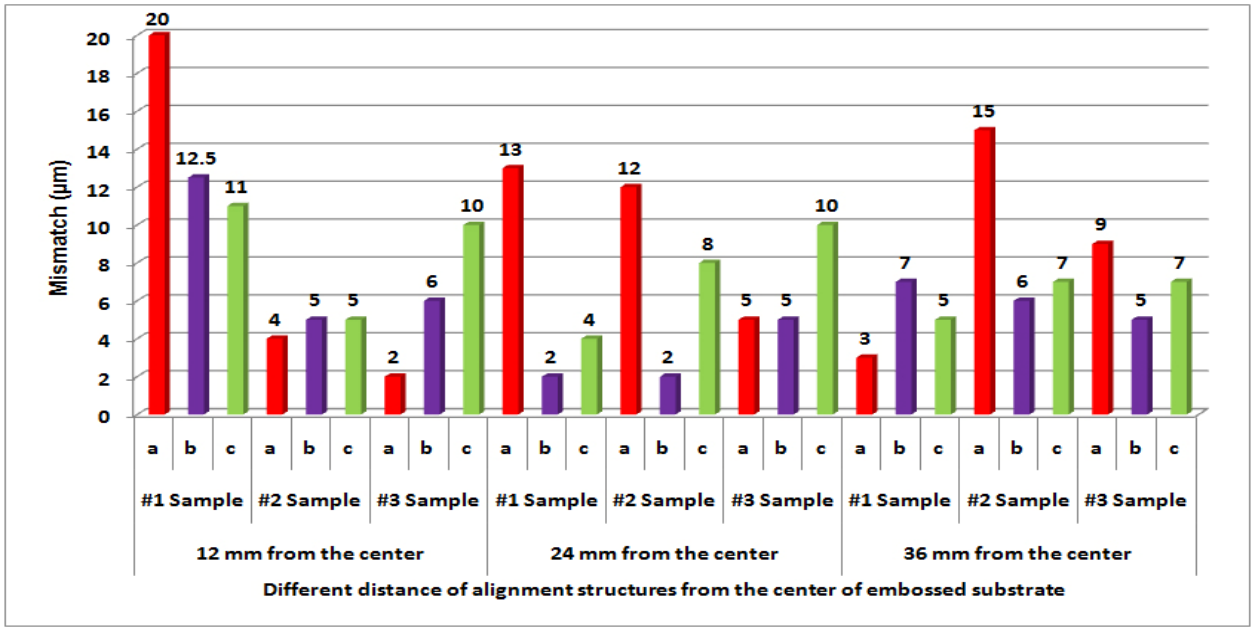

Figure 5.17: Mismatches for three pairs of v-grooves and posts; the results were categorized as three groups based on the radical location of structures, 12 mm, 24mm, and 36mm.

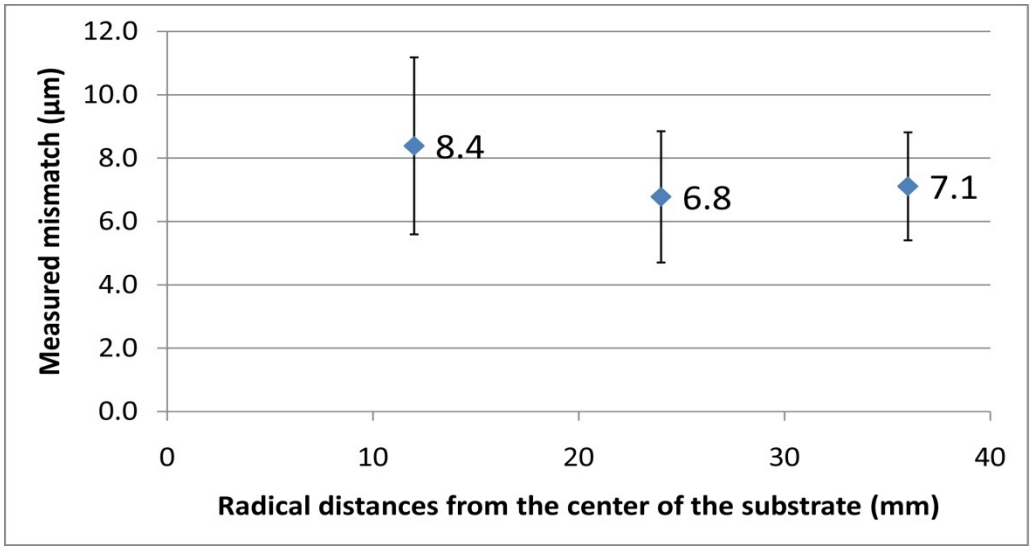

Figure 5.18: The mean mismatch between two plates using three pairs of v-groove and hemispherical posts with annular structures as a function of the radial distance from the center of the plates.

Figure 5.18 shows the mean mismatch between two plates using the modified passive alignment features. There was no significant difference of the measured mismatch for different

locations. The mean mismatch between the two plates, 6.8 µm to 8.4 µm, were much smaller than the results in the previous study, 28 µm to 75µm. This was a consequence of the complete filling of the hemisphere-tipped post by adding the convex annular ring around the hemispherical recess.

5.4 A Reagent Distribution Device for a 96 CFPCR Array

After developing passive alignment features to assemble two microfluidic plates in a modular approach, a reagent distribution device is designed and fabricated to efficiently inject the sample into the 96 CFPCR array. In addition the reagent distribution device can be also used as an interface between an operator and a 96 CFPCR array by reducing the frequencies of sample loading.

5.4.1 Review of Modular Devices

Two individually modular microfluidic systems were realized as sensors to detect the concentration of chromium metal in ground water and as a dialysis unit for desalination of DNA samples [Martin et al., 1999]. Both microfluidic systems included several different functional layers made of polymers like polyimide, PMMA, and polycarbonate. The main microfabrication technique used was layer lamination to directly write the microchannel layout on the polymer substrates. Rubber gaskets were used between layers to prevent leakage and the adhesives were used to bond the different functional layers. Both experiments were realized on the modular microfluidic system, but did not have any further results like comparison of experiment results between a planar device and a modular device.

A modular microfluidic system was developed to perform the cell preparation on a chip including mixing with magnetic beads, incubation, and capturing of *E. Coli* cells in either PBS buffer or blood [Grodzinski et al., 2003, Grodzinski et al., 2004]. Polycarbonate substrates were

used as the materials for the microfluidic devices and the microchannels were made by using either milling or laser writing. To combine those functional microfluidic devices together, a universal docking board was built with many parallel slots on it. The parallel slots were connected to wires as passages of electrical signals and also used as mechanism supports for microfluidic devices in a vertical position. A position barrel fluidic interconnect, including a customized interconnect and a O-ring, was used between each functional layer to prevent leakage. To demonstrate the success of this modular microfluidic system, 2 micro mixers, 1 incubation, and a cell capturing microfluidic device were assembled and the target cells, *E. Coli*, were mixed with either PBS buffer or blood and pumped through the modular microsystem. The cells were successfully captured with a capture efficiency of 53 % in PBS solution and 37 % in blood.

Several groups used modular microfluidic systems to realize different research tasks on different substrate materials including glass, PDMS, and polymers [Blake et al., 2007, Flachsbart et al., 2006, Hofmann et al., 2001, Kikutani et al., 2002]. The idea behind these microfluidic systems was to fabricate different functional layers individually, seal them either using adhesive materials or by applying surface treatments like plasma for PDMS layers, assemble the multiple layers together, and inject the biochemical reagents from the top layer and distribute them to the lower layers through interconnects. The leakage between layers was prevented by O-rings, adhesive material, or the plasma-activated PDMS bonding. The reservoirs in those devices were all on the millimeter-scale, which made the alignment and reagent transportation between multiple layers easier. All of the demonstrated results could be realized at room temperature to avoid thermal management issues in the three-dimensional microfluidic architecture. The benefits of using a modular approach to a microfluidic system not only included the flexible selection of different substrate materials or different functional devices, but also the effective

distribution of the chemical reagents to different microchannels from the top layer to the lower layers.

5.4.2 Introduction and Design Idea of a Reagent Distribution Device

The idea of building a microfluidic system using a modular approach is shown in Figure 5.19 which has three layers including a reagent distribution device, a 96 CFPCR array, and a multizone thermal system. The design, fabrication, and performance of a 96 CFPCR array was described in Chapter 3 and Chapter 4 shows the thermal characterization of the multizone thermal system, and this Section focuses on the realization of a reagent distribution device. A reagent delivery device is useful and necessary for a high throughput microfluidic device like a 96 CFPCR array and it can reduce the frequency of sample loading and make the analyte distribution more efficient. To combine a reagent distribution device with a 96 CFPCR array, the developed passive alignment structures described in Section 5.3 was applied to achieve an aligned passage for chemical reagent transportation from layer to layer. Furthermore the thermal management issue in a modular approach has to be considered to prevent lowering the natural convection cooling capability to a 96 CFPCR array. The layout of the reagent distribution device can be customized designed depending on the requirement for the microfluidic system, different types of sample analyzed, and the layout of the 96 CFPCR array.

5.4.3 Layout of a Reagent Distribution Device

A simple microchannel layout was used to distribute the chemical reagent in this research, which included T-junctions to divide major microchannels into sub-microchannels. The substrate material for a reagent distribution device is polycarbonate but other materials could be used as well. A polycarbonate reagent distribution device is proposed to fabricate by double-sided hot embossing technique with two mold inserts, one for top pattern and one for bottom pattern of a

reagent distribution device. The layout of the top mold insert is shown in Figure 5.20 and the pattern of the bottom mold insert is shown in Figure 5.21. In the design of the top mold insert, four different functional microstructures were designed, which composed dummy structures for cutting after embossing, alignment structures for double-sided hot embossing, alignment structures for thermal bonding the cover sheet, and microchannels for reagent distribution. In the design of the bottom mold insert, five functional structures were designed including dummy structures for cutting after embossing, alignment structures for double-sided hot embossing, alignment structures for assembling with a 96 CFPCR array, alignment standards for mismatch measurement, and structures for thermal management.

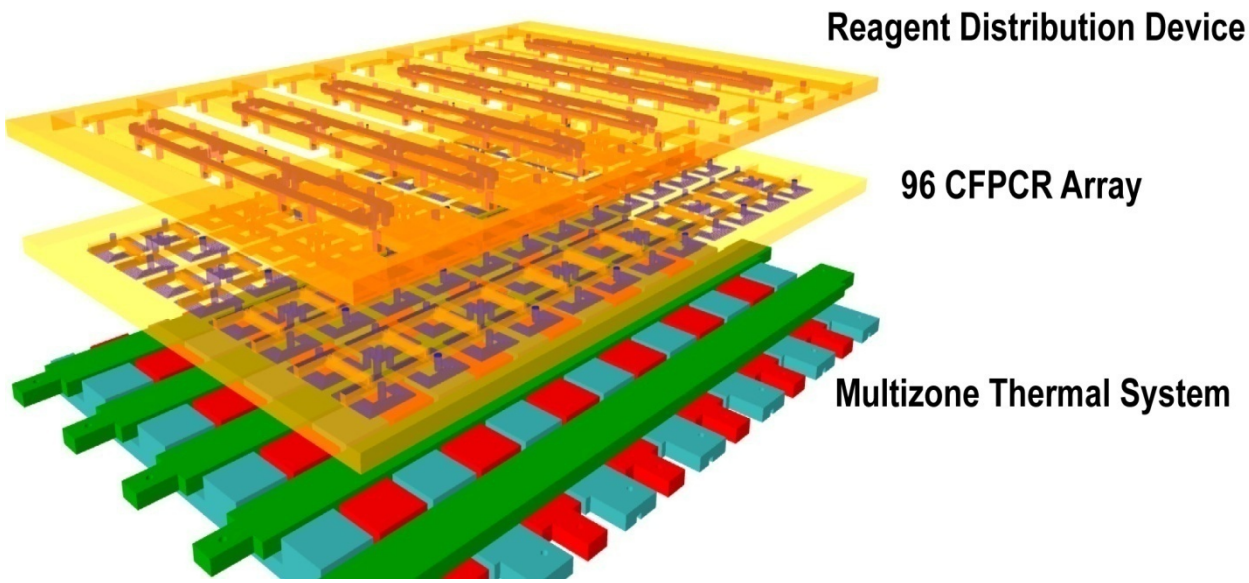

Figure 5.19: Configuration of a microfluidic system in a modular approach. The top layer is a reagent distribution device for efficient sample loading, the middle layer is a 96 CFPCR array for amplification, and the lower layer is a multizone thermal system to support the desired thermal performance of a 96 CFPCR array.

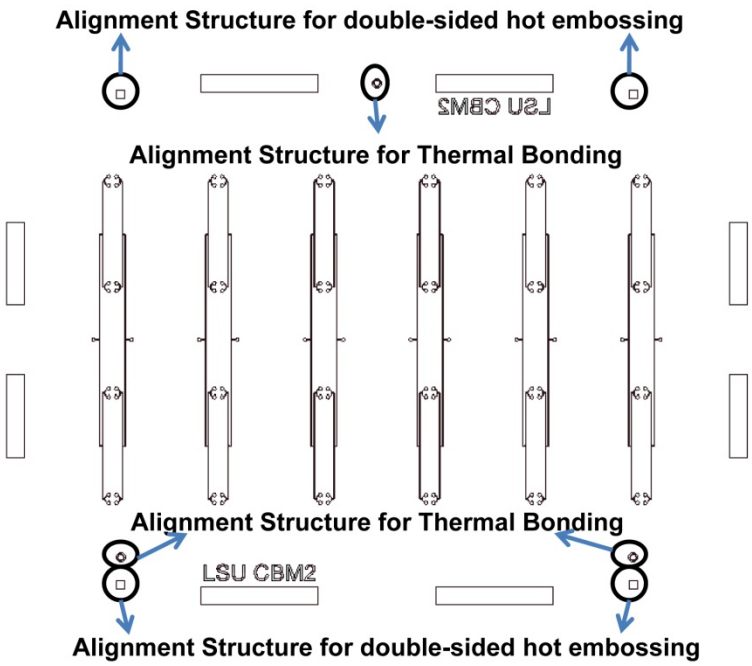

Figure 5.20: The layout of the top mold insert for a reagent distribution device which included four functional components including alignment structures for double-sided hot embossing, alignment structures for thermal bonding, dummy structures (the rectangles) for cutting, and the microchannels for reagent distribution.

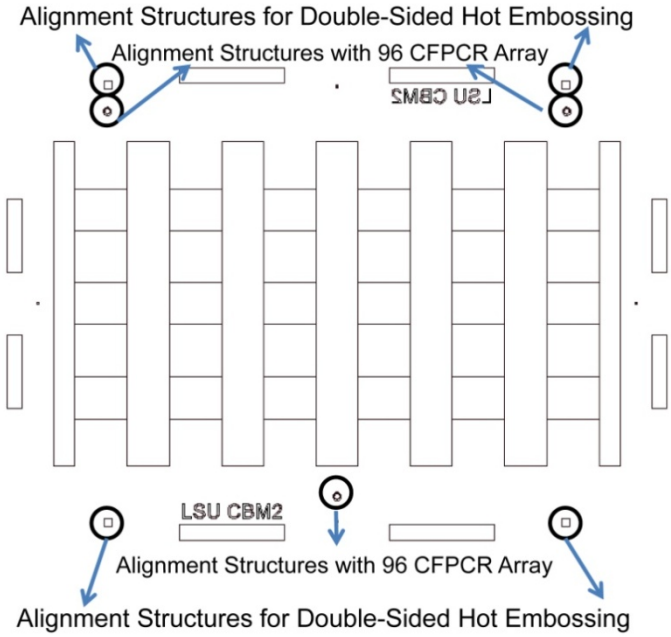

Figure 5.21: The layout of the bottom mold insert for a reagent distribution device which included five functional components including alignment structures for double-sided hot embossing, alignment structures for assembling with a 96 CFPCR array, dummy structures (the rectangles) for cutting, alignment standards (small squares) for mismatch measurement, and structures for thermal management.

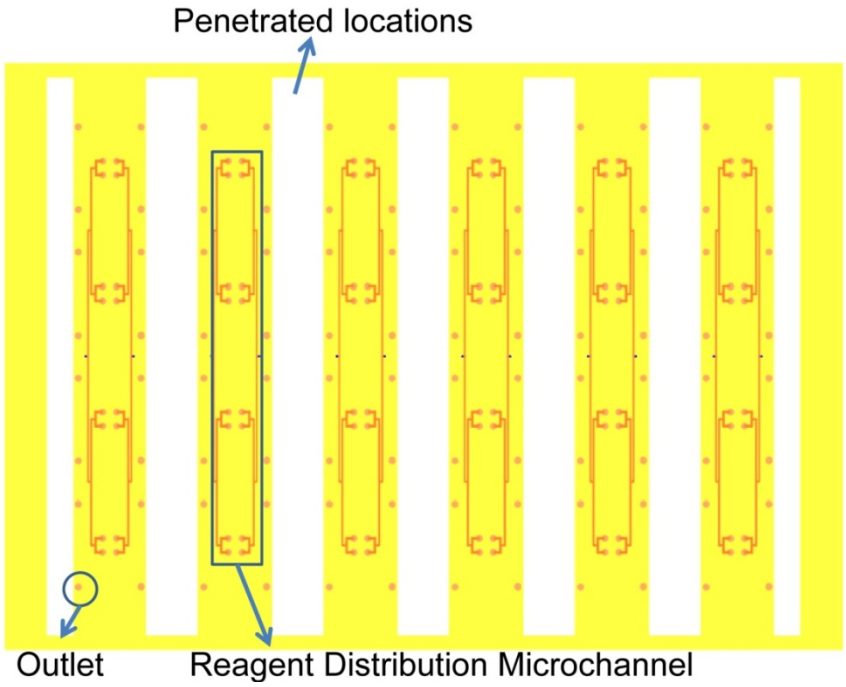

Figure 5.22: The configuration of the reagent distribution device from the top view.

Since the cooling of the 96 CFPCR array depends on the natural convection, so a reagent distribution device in modular approach might lower the cooling capability resulting in a nonuniform temperature distribution. To ensure no accumulated warm air between the reagent distribution and the 96 CFPCR array, certain locations of the reagent distribution device were open to the ambient air and those locations were corresponded to the renaturation zones on the 96 CFPCR array. Figure 5.22 also shows the locations of outlets and the reagent distribution microchannels. The reagent distribution microchannel is based on the idea of T-junctions to divide the chemical reagents from an universal inlet into 8 outlets, and the reagents flow to the 8 CFPCRs and flow back to the outlets on the reagent distribution device after either 20 or 25 cycle amplifications on the 96 CFPCR array.

5.4.4 Conclusions

A polycarbonate reagent distribution device was designed to efficiently load the analyte into a 96 CFPCR array, moreover as a friendly interface between the operator and the high

throughput microsystem. The reagent distribution device was proposed to stack on the 96 CFPCR array, so the design concerns included the design of reagent distribution channels, interfacing techniques between the reagent distribution device and a 96 CFPCR array, and avoiding disturbance to the thermal performance of a 96 CFPCR array. Several functional components were designed to realize a reagent distribution device including passive alignment structure, reagent distribution microchannels, and thermal management structures.

To integrate with a 96 CFPCR array as a high throughput microsystem, a passive alignment structure was studied and designed [You et al., 2006]. The first generation passive alignment structure showed a mismatch between 28-75 μm due to the incomplete polymer filling leading to a short hemisphere-tipped post. A modification was realized using an idea of adding convex annular structure around the hemispherical recess to reduce the flowing distance of melted polymer during hot embossing, and the experiment results showed a mismatch less than 15 μm.

The distribution microchannel was designed using T-junctions and it had a universal inlet, used for connecting an injection syringe, and eight outlets, used to distribute the chemical reagents into eight CFPCRs. The thermal management structures were designed on the backside of the reagent distribution device to prevent air from accumulating between a reagent distribution device and a 96 CFPCR array leading to a lower cooling efficiency.

CHAPTER 6: CONCLUSIONS AND FUTURE WORK

6.1 Conclusions

Infectious diseases have threatened human health for centuries, currently there are no promising methodologies to completely eliminate the fear of them. A best defense against infectious disease is to rapidly and correctly pinpoint a pathogen or virus and give the patients the best medical treatment. To achieve this efficient detection, multiple tests have to be realized simultaneously like the high throughput robot systems used for the Human Genome Project. To further accelerate the detection time or more correctly identify a pathogen or virus, micro/nano technology and nucleic acid analysis have to be used. A modular, high throughput microfluidic system against infectious disease is proposed and its advantages includes parallel sample analysis, accelerated process time, reliability, accuracy, self-powered, friendly interface, and the flexibility to use different combinations of microfluidic systems.

The ultimate goal of this research is to develop a microfluidic system for use against acute infectious disease. Several steps toward the final goal, including thermal management for a microfluidic device, protein adsorption phenomena in a continuous flow environment, passive alignment structure, a reagent distribution device, a 96 CFPCR array, and a multizone thermal system were addressed.

6.1.1 Thermal Management for a Polycarbonate Microfluidic Device

Using nucleic acid analysis to detect acute infectious disease, several steps may require sequence of specific temperatures for biochemical reactions, so precise temperature control is critical. Finite element analysis (FEA) and an infrared camera were used to investigate the temperature distribution of a polycarbonate microfluidic device, a continuous flow polymerase chain reactor (CFPCR). The simulations and experimental results showed that using copper

plates was the key factor in obtaining uniform, discrete temperature distributions. In addition using grooves to separate each temperature zone on the substrate could reduce the required heating power, increase the heating/cooling rates, and make each temperature zone more independent. Using a thinner polycarbonate device reduced the temperature gradient between the heaters and the microchannels, which was beneficial for the precise temperature inside the microchannel. Good thermal management boosted the biochemical performance due to the well-controlled temperature, and the amplification efficiency for the DNA fragments of interest increased 363%.

6.1.2 Protein Adsorption in a Microchannel

Microfluidic devices have become a major experimental platform for biochemistry and biology, due to the size advantage, small sample requirements, and improved sensitivity. However there is also a disadvantage due to the high surface-to-volume ratio of the devices which leads to huge protein adsorption. Since many biochemical reactions like polymerase chain reaction depend on active proteins or enzymes in the solutions, protein adsorption is a critical issue for the success of polymer microfluidic systems. Protein adsorption was a result of the combination of surface chemistry and flow dynamics. Surface chemistry accounted for the interaction between the protein molecules and the microchannel walls and the flow dynamics accounted for the probability of contact between the suspended molecules and the microchannel walls.

Many researchers use different methods to passivate the microchannel walls to reduce protein adsorption. The methods can be categorized into two groups, dynamic coating and static coating. Dynamic coating uses dummy proteins to compete with the active protein for the adsorption sites in the microchannel in real-time. Static coating uses the dummy proteins to

block the adsorption sites before injecting the active proteins into the microchannel. Microchannels with different geometries such as different cross-sectional areas or different lengths were fabricated for a series of experiments. Longer microchannels adsorbed more proteins from the solution and the adsorption rate was not uniform along the all microchannel. Adsorption saturation of microchannels with smaller cross-sectional areas took much longer. Only a small portion of the blocking protein had a chance to contact the microchannel walls due to the laminar flow behavior and neither dynamic or static coating was very efficient, especially in smaller microchannels.

6.1.3 A High Throughput Microfluidic System in a Modular Approach

A modular high throughput microfluidic system was proposed that included three major components, a reagent distribution device, a 96 CFPCR array, and a multizone thermal system. Each device has individual concerns, but there are also interface issues that challenge working as a system.

The reagent distribution device was fabricated on a polycarbonate substrate, but could be fabricated from other materials as long as they are compatible with the other functional devices. The main purpose of the reagent distribution device is to divide the chemical reagents from one universal inlet to eight outlets using a T-junction design of the microchannel, which efficiently delivers the chemical reagents to the 96 CFPCR array and reduces the necessity for frequent pipetting of analytes. The reagent distribution device was fabricated by double-sided hot embossing with two mold inserts and the microchannels were sealed with a 0.25 mm thick polycarbonate sheet.

A 96 CFPCR array was designed and fabricated using the UV-LIGA process on a polycarbonate substrate and 96 CFPCRs were distributed in 12 columns and 8 rows in an area of

120 mm × 96 mm. Each CFPCR was limited in an area of 8 mm × 8 mm devices for either 20 cycles or 25 cycles were built inside this area to demonstrate the concept. To achieve the desired temperature distribution within each CFPCR, numerical simulations were used to select the dimensions for cooling mechanisms, to understand the temperature distribution, and to optimize its thermal performance. Several biochemical experiments were realized on 20-cycle CFPCRs to validate the design of each CFPCR and to understand the limiting performance of this nanoliter CFPCR. Six different DNA fragments from 99 bp to 997 bp corresponding to different renaturation temperatures were successfully amplified individually on the 20 cycle CFPCR. Another experiment estimated the limiting number of starting copies of DNA template for a successful amplification. A staring copy number of 8000 produced a successful amplification.

To realize a microfluidic system for deletion of acute infectious disease using nucleic acid analysis, multiple temperature zones were required to support the different functional components on a single substrate, which led to a demand for a multizone thermal system. Since each CFPCR required three discrete and uniform temperature zones for amplification, a 96 CFPCR array needed 288 steady-state temperature zones. A multizone thermal system using eighteen copper strips to realize 288 steady-state temperature zones was developed based on the idea of CFPCRs sharing temperature zones. A columnar device composed of eight CFPCRs was used on the multizone thermal system to evaluate the thermal performance. A ±1°C variation in the renaturation and extension zones and a ±2°C variation in the denaturation zone were obtained. An extended experiment was carried out to estimate the thermal performance of a 96 CFPCR array on the multizone thermal system. A nonuniform temperature distribution was produced in the polycarbonate 96 CFPCR array. Several factors contributed to the nonuniformity such as the large thermal capacitance of the copper strips, poor attachment between the copper strips and the

96 CFPCR array, and air accumulating around the copper strips to lower the cooling capability. Several biochemical experiments were realized on the multizone thermal system using either a columnar device composing with eight CFPCRs or a row device composed of twelve CFPCRs. The column device demonstrated the parallel amplification of identical DNA fragments from 99 bp to 500 bp individually and the row device demonstrated the parallel amplification of different DNA fragments from 99 bp to 997 bp.

6.2 Future Work

The ultimate goal of this research is to develop a modular high throughput microfluidic system. The achievements described in Section 6.1 include the three fundamental components, a reagent distribution device, a 96 CFPCR array, and a multizone thermal system. Several sub-topics have been addressed including thermal management, protein adsorption, and passive alignment structure. To upgrade the current microfluidic system toward a practical tool for use against acute infectious disease, more advanced research have to be realized to improve the current performance.

6.2.1 Thermal Management

Precise temperature control is critical for many biochemical reactions. This was validated in Chapter 2, with the improvement of thermal management in a microfluidic device to the amplification result in a CFPCR. Researchers are still working toward the goal of real-time and insitu temperature monitoring in the micro/nano channels, which not only can accurately controls the temperature distribution of the analytes in the micro/nano channel but also can help understand the change of biological targets as a function of small changes in temperature. Except for the temperature control in a micro/nano channel, thermal management in a complicated microfluidic system should be developed as well to improve the systematic performance. The 3-

D thermal management has not been addressed since the current microfluidic devices are primarily on planar substrates. To maximize the power of microfluidic systems, modularity is an approach but it also generates other issue like thermal management in microfluidic systems fully packed with various microfluidic thermal reactors.

6.2.2 Protein Adsorption

Biological molecules are the most interesting targets in Bio-MEMS and control of the biological molecules is one of the critical factors in the success of the micro/nano fluidic devices. A technique for controlling the biological molecules well that can be applied in many applications such as point-of-care system, drug delivery system, and fundamental studies of biology, is needed. Protein adsorption is an issue of surface chemistry and fluid dynamics. Control of protein adsorption might be the direction or hint for those researches to well control biological molecules in a micro/nano device. Simulation will be an appropriate tool to deliver more insight while accounting for different sizes of molecules, different geometries of microchannels, different flow velocities, and different surface properties, to validate the experimental results and help design the micro/nano channels.

6.2.3 Interface Technology

In a microfluidic system, interface technology is another critical factor for achieving a better system level performance, in addition to well developed functional devices. In the modular microfluidic systems, interface technology is more important and critical to the success of the system, since the factors include mechanical assembly, thermal interaction, and fluid transport. Several interface techniques were developed including passive alignment structures between two plates, thermal management to avoid thermal interference either between two microfluidic devices or between two microfluidic plates, using a thermal conductivity pad between the

multizone thermal system and the 96 CFPCR array to have a good thermal transfer, and using the design of the reagent distribution to reduce the frequency of pipetting between the operator and the 96 CFPCR array. Besides those interface technology achievements, several techniques are also required to enhance the performance of the microfluidic system like interconnector, a sample loading system and packaging. To ensure the smooth transportation of mass, momentum, and energy between microfluidic devices, passive alignment structures are not sufficient; an interconnection technology is required to prevent leakage. Smoother transportation can improve the success rate of detecting the acute infectious disease or cancer cells in the early stages since the rare targets in the micro/nano channels will not be lost in poor interconnection. The reagent distribution device can play a role as an interface between the operator and the 96 CFPCR array, but the loading process is still inconvenient. A loading system is required for simple loading of samples by the operator. Packaging will be the last task for the modular high throughput microfluidic system and it means majorly two techniques, firstly a technique to hold all microfluidic devices after assembly and second a technique to protect the microfluidic system against ambient environment with portability function. A passive alignment structure and an interconnect can ensure smooth transport of analytes without leakage but a holding technique is also mandatory to have a steady structure during operation. Packaging of the microfluidic system can ensure a steady-state environment for the biochemical reactions without being affected by the harsh external environment, which guarantees accurate function.

REFERENCES

Becker, H., Gartner, C., "Polymer microfabrication methods for microfluidic analytical applications", *Electrophoresis*, Vol. 21, 12-26, 2000.

Becker, H., Locascio, L. E., "Polymer microfluidic devices", *Talanta*, Vol. 56, 267-287, 2002.

Beebe, D. J., Moore, J. S., Yu, Q., Liu, R. H., Kraft, M. L., Jo, B. H., Devadoss, C., "Microfluidic techtonics: A comprehensive construction platform for microfluidic systems", *PNAS*, Vol. 97, No. 25, 13488-13493, 2000.

Belgrader, P., Young, S., Yuan, B., Primeau, M., Christel, L. A., Pourahmadi, F., Northrup, M. A., "A battery-powered notebook thermal cycler for rapid multiplex real time PCR analysis", *Anal. Chem*., Vol. 73, 286-289, 2001.

Blake, A. J., Pearce, T. M., Rao, N. S., Johnson, S. M., Williams, J. C., "Multilayer PDMS microfluidic chamber for controlling brain slice microenvironment", *Lab on a chip*, Vol. 7, 842-849, 2007.

Boone, T. D., Ricco, A. J., Fan, Z. H., Tan, H., Hooper, H. H., Williams, S. J., "Plastic advances microfluidic devices", *Anal. Chem*., Vol. 74, No.3, 78-86A, Feb. 2002.

Brecher, C., Lange, S., Peschke, C., Weinzierl, M., Spanier, G., Mokwa, W., "Production processes and applications for the passive alignment of microcomponents", *Microsyst technol*, Vol. 12, 611-615, 2006.

Brenan, C., Morrison, T., "High throughput, nanoliter, quantitative PCR", *Drug Discovery Today: Technologies"*, Vol. 2, No. 3, 247-253, 2005.

Cameron, N. S., Roberge, H., Veres, T., Jakeway, S. C., Crabtree, H. J., "High fidelity, high yield production of microfluidic devices by hot embossing lithography: rheology and stiction", *Lab on a chip*, Vol. 6, 936-941, 2006.

Chen, H. J. H., Chen, T. F., Huang, S. R. S., Gong, J., Li, J. C., Chen, W. C., Hseu, T. H., Hsu, I. C., "A novel micro-well array chip for liquid phase biomaterial processing and detection", *Sensors and Actuators A*, Vol. 108, 193-200, 2003.

Chen, P.-C., "Accelerating micro-scale PCR for Modular Lab-on-a-Chip system", *Mastes's Thesis*, Louisiana State University, Baton Rouge, LA 70803, 2006.

Chen, P.-C., You, B.-H., Park, D. S., Park, S.-G., Guy, J., Nikitopoulos, D. E., Soper, S. A., Murphy, M. C., "Replication of reliable assembly features for polymer modular microfluidic systems", *2007 ASME International Mechanical Engineering Congress & Expo (IMECE)-16100, Seattle, WA,* 2007a.

Chen, P.-C., Nikitopoulos, D. E., Soper, S. A., Murphy, M. C., "Assessment and improvement of the thermal performance of pa polycarbonate micro continuous flow polymerase chain reactor (CFPCR)", *2007 ASME International Package-33330, Vancouver,* BC , 2007b.

Chen, P.-C., Nikitopoulos, D. E., Soper, S. A., Murphy, M. C., "Temperature distribution effects on micro-CFPCR performance", *Biomed. Microdevices*, Vol. 10, 141-152, 2008.

Chaudhari, A. M., Woudenberg, T. M., Albin, M., Goodson, K. E., " Transient liquid crystal thermometry of microfabricated PCR vessel arrays", *Journal of Microelectromechanical Systems*, Vol. 7, No. 4, 345-355, 1998.

Chou, C. F., Changrani, R., Roberts, P., Sadler, D., Burdon, J., Zenhausern, F., Lin, S., Mulholland, A., Swami, N., Terbrueggen, R., "A miniaturized cyclic PCR device-modeling and experiments", *Microelectronic Engineering*, Vol. 61-62, 921-625, 2002.

Chou, H. P., Unger, M. A., Quake, S. R., "A microfabricated rotary pump", *Biomedical Microdevices*, Vol. 3, No. 4, 323-330, 2001.

College of American Pathologists, "Point-of-care testing, section 30. Northfield, IL", *College of American Pathologists*, 2001.

Collins, F. S., Morgan, M., Patrinos, A., "The Human Genome Project: Lessons from large-scale biology", *Science*, Vol. 300, 286-290, 2003.

Crews, N., Wittwer, C., Palais, R., Gale, B., "Product differentiation during continuous flow thermal gradient PCR", *Lab-on-a-Chip*, Vol. 8, 919-924, 2008.

Csako G., "Present and future of rapid and/or high throughput methods for nucleic acid testing", *Clinica Chimica Acta*, Vol. 363, 6-31, 2006.

Cui, D., Tian, F., Kong, Y., Titushikin, I., Gao, H., "Effects of single-walled carbon nanotubes on the polymerase chain reaction", *Nanotechnology*, Vol. 15, No. 1, 154-157, 2004.

DeVoe, D. L., "Thermal Issues in MEMS and Microscale Systems", *IEEE Transactions on components and packaging technologies*, Vol. 25, No. 4, 576-583, 2003.

de Mello, A. J., Habgood, M., Lancaster, N. L., Welton, T., Wootton, R. C. R., "Precise temperature control in microfluidic devices using joule heating of ionic liquids", *Lab on a Chip*, Vol. 4, 417-419, 2004.

Desta, Y. M., "Fabrication of High aspect ratio vibrating cylinder microgyroscope structures by use of the LIGA process", Doctor of Philosophy's Dissertation, Louisiana State University, Baton Rouge, LA 70803.

El-Ali, J., Perch-Nielsen, I. R., Poulsen, C. R., Bang, D. D., Telleman, P., Wolff, A., "Simulation and experimental validation of a SU-8 based PCR thermocycler chip with integrated heaters and temperature sensor", *Sensors and Actuators A*, Vol. 110, 3-10 2004.

Elnifro, E. M., Ashshi, A. M., Cooper, R. J., Klapper, P. E., "Multiplex PCR: Optimization and application in diagnostic virology", *Clinical Microbiology Reviews*, Vol. 13, No. 4, 559-570, 2000.

Emrich, C. A., Tian, Huijun, Medintz, I. L., Mathies, R. A., "Microfabricated 384-lane capillary array electrophoresis bioanalyzer for ultrahigh-throughput genetic analysis", *Anal. Chem*., Vol. 74, 5076-5083, 2002.

Erill, I., Campoy, S., Erill, N., Jordi B., Aguilo J., "Biochemical analysis and optimization and adsorption phenomena in glass-silicon PCR-chips", *Sensors and Actuators B*, Vol. 96, 685-692, 2003.

Flachsbart, B. R., Wong, K., Iannacone, J. M., Abante, E. N., Vlach, R. L., Rauchfuss, P. A., Bohn, P. W., Sweedler, J. V., Shannon, M. A., "Design and fabrication of a multilayered polymer microfluidic chip with nanofluidic interconnects via adhesive contact printing", *Lab on a chip*, Vol. 6, 667-674, 2006.

Frey, O., Bonneick, S., Hierlemann, A., Lichtenberg, J., "Autonomous microfluidic multi-channel chip for real-time PCR with integrated liquid handling", *Biomed. Microdevices*, Vol. 9, 711-718, 2007.

Friedrich, C. R., Avula, R. R. K., Gugale, S., "A fluid microconnector seal for packaging applications", *J. Micromech. Microeng*., Vol. 15, 1115-1124, 2005.

Gerlach, A., Knebel, G., Guber, A. E., Heckele, M., Herrmann, D., Muslija, A., Schaller, Th., "Microfabrication of single-use plastic microfluidic devices for high throughput screening and DNA analysis", *Microsystem Technologies*, Vol. 7, 265-268, 2002.

Gervais, T., El-Ali, J., Gunther, A., Jensen, K. F., "Flow-induced deformation of shallow microfluidic channels", Lab on a chip, Vol. 6, 500-507, 2006.

Gong, H., Ramalinggam, N., Chen, L., Che, J., Wang, Q., Wang, Y., Yang, X., Yap, P. H. E., Neo, C. H., "Microfluidic handling of PCR solution and DNA amplification on a reaction chamber array biochip", *Biomed. Microdevices*, Vol. 8, 167-176, 2006.

Gonzalez, A., Grimes, R., Walsh, E. J., Dalton, T., Davies, M., "Interaction of quantitative PCR components with polymeric surfaces", *Biomed. Microdevices*, Vol. 9, 261-266, 2007.

Gonzalez, C., Collins, S. D., Smith, R. L., "Fluidic interconnects for modular assembly of chemical Microsystems", *Sensors and Actuators B*, Vol. 49, 40-45, 1998.

Gray, B. L., Collins, S. D., Smith, R. L., "Interlocking mechanical and fluidic interconnections for microfluidic circuit boards", *Sensors and Actuators A*, Vol. 112, 18-24, 2004.

Gray, B. L., Jaeggi, D., Mourlas, N. J., van Drieenhuizen, B. P., Williams, K. R., Maluf, N. I., Kovacs, G. T. A., "Novel interconnection technologies for integrated microfluidic systems" *Sensors and Actuators*, Vol. 77, 57-65, 1999.

Grodzinski, P., Yang, J., Liu, R. H., Ward, M. D., "A modular microfluidic system for cell pre-concentration and genetic sample preparation", *Biomedical Microdevices*, Vol. 5, No. 4, 303-310, 2003.

Grodzinski, P., Yang, J., Liu, R. H., Ward, M. D., "Microfluidic system integration in sample preparation chip sets – a summary", *Proceedings of the 26th Annual International Confernece of the IEEE EMBS*, 2615-2618, 2004.

Guber, A. E., Heckele, M., Herrmann, D., Muslija, A., Saile, V., Eichhorn, L., Gietzelt, T., Hoffman, W., Hauser, P. C., Tanyanyiwa, J., Gerlach, A., Gottschlich, N., Knebel, G., "Microfluidic lab-on-a-chip systems based on polymers-fabrication and application", *Chemical Engineering Journal*, Vol. 101, 447-453, 2004.

Guijt, R. M., Dodge, A., van dedem, G. W. K., de Rooij, N. F., Verpoorte, E., "Chemical and physical processes for integrated temperature control in microfluidic devices", *Lab on a Chip*, Vol. 3, 1-4, 2003.

Han, A., Wang, O., Graff, M., Mohanty, S. K., Edwards, T. L., Han, K. H., Frazier, A. B., "Multi-layer plastic/glass microfluidic systems containing electrical and mechanical functionality", *Lab on a chip*, Vol. 3, 150-157, 2003.

Hashimoto, M., Chen, P. C., Mitchell, M. W., Nikitopoulos, D. E., Soper, S. A., and Murphy, M. C.," Rapid PCR in a continuous flow device" *Lab on a Chip*, vol. 4, p638-645, 2004.

Heckele, M., Guber, A. E., Truckenmuller, R., "Replication and bonding techniques for integrated microfluidic systems", *Microsyst Technol*, Vol. 12, 1031-1035, 2006.

Hay, J. L., Hollingsworth, D. K., "A comparison of trichrome systems for use in the calibration of polymer-dispersed thermochromic liquid crystals", *Experimental Thermal and Fluid Science*, Vol. 12, 1-12, 1996.

He, Y., Fu, J. Z., Chen, Z. C., "Research on optimization of the hot embossing process", *J. Micromech. Microeng.*, Vol. 17, 2420-2425, 2007.

Heckele, M., Schomburg, W. K., "Review on micro molding of thermoplastic polymers", *J. Micromech. Microeng.*, Vol. 14, R1-R14, 2004.

Heyderman, L. J., Schift, H., David, C., Gobrecht, J., Schweizer, T., "Flow behavior of thin polymer films used for hot embossing lithography", *Microelectronic Engineering*, Vol. 54, 229-245, 2000.

Hofmann, O., Niedermann, P., Manz, A., "Modular approach to fabrication of three-dimensional microchannel systems in PDMS-application to sheath flow microchips", *Lab on a chip*, Vol. 1, 108-114, 2001.

Holland, C. A., Kiechle, F. L., "Point-of-care molecular diagnostic systems – past, present, and future", *Current Opinion in Microbiology*, Vol. 8, 504-509, 2005.

Hong, J. W., Studer, V., Hang, G., Anderson, W. F., Quake, S R., "A nanoliter-scale nucleic acid processor with parallel architecture", *Nature Biotechnology*, Vol. 22, No. 4, 435-439, 2004.

Huang, Y., Mather, E. L., Bell, J. L., Madou, M., "MEMs-based sample preparation for molecular diagnostics", *Anal. Bioanal. Chem.*,Vol. 372, 49-65, 2002.

Hupert, M. L., Guy, W. J., Llopis, S. D., Situma, C., Rani, S., Nikitopoulos, D. E., Soper, S. A., "High-precision micromilling for low-cost fabrication of metal mold masters", *Microfluidic, BioMEMS, and Medical Microsystems IV, Proc. Of SPIE*, 6112, 61120B-1, 2005.

Hupert, M. L., Guy, W. J., Llopis, S. D., Shadpour, H., Rani, S., Nikitopoulos, D. E., Soper, S. A., "Evaluation of micromilled metal mold masters for the replication of microchip electrophoresis devices", *Microfluid Nanofluid*, Vol. 3, 1-11, 2007.

Igata, E., Arundell, M., Morgan, H., Cooper, J. M., "Interconnector reversible lab-on-a-chip technology", *Lab on a chip*, Vol. 2, 65-69, 2002.

Incropera, F. P., Dewitt, D. P., "*Fundamentals of heat and mass transfer 5th edition*", John Wiley & Sons, Inc., 2002.

International Human Genome Sequencing Consortium, "Initial sequencing and analysis of the human genome", *Nature*, Vol. 15, 860-921, 2001.

Janasek, D., Franzke, J., Manz, A., "Scaling and the design of miniaturized chemical-analysis systems", *Nature*, Vol. 442, 374-380.

Jendrejack, R. M., Dimalanta, E. T., Schwartz, D. C., Graham, N. D., Pablo, J. J., "DNA dynamics in a microchannel", *Physical Review Letters*, Vol. 91, No.3, 038102-1 – 038102-4, 2003.

Johnson, N. P. A. S., Mueller, J., "Updating the accounts: global mortality of the 1918-1920 "Spanish" influenza pandemic", *Bull. Hist. Med*., Vol. 76, 105-115, 2002.

Juang, Y.-J., Lee, L. J., Koelling, K. W., "Hot embossing in microfabrication. Part I: Experimental", Vol. 42, No. 3, 539-550, 2002.

Juang, Y.-J., Lee, L. J., Koelling, K. W., "Hot embossing in microfabrication. Part II: Rheological characterization and process analysis", Vol. 42, No. 3, 551-566, 2002.

Kikutani, Y., Horiuchi, T., Uchiyama, K., Hisamoto, H., Tokeshi, M., Kitamori, T., "Glass microchip with three-dimensional microchnanel network for 2×2 parallel synthesis", *Lab on a chip*, Vol. 2, 188-192, 2002.

Kim, J. A., Lee, J. Y., Seong, S., Cha, S. H., Kim, J. J., Park, T. H., "fabrication and characterization of a PDMS-glass hybrid continuous flow PCR chip", *Biochemical Engineering Journal*, Vol. 29, 91-97, 2006.

Koc, C., de Mello, A. J., McHale, G., Newton, M. I., Roach, P., Shirtcliffe, N. J., "Nnao-scale superhydrophobicity : suppression of protein adsorption and promotion of flow-induced detachment", *Lab Chip*, Vol. 8, 582-586, 2008.

Kohn, G. C., "The Wordsworth Encyclopedia of Plague and Pestilence", *Wordsworth editions Ltd*, 1998.

Kricka, L. J., Fortina, P., Panaro, N. J., Wilding, P., Alonso-Amigo, G., Becker, H., "Fabrication of plastic microchips by hot embossing", *Lab on a Chip*, Vol. 2, 1-4, 2002.

Krishnan, M., Burke, D. T., Burns, M. A., "Polymerase chain reaction in high surface-to-volume ratio SiO_2 microstructures", Anal. Chem., Vol. 76, 6588-6593, 2004.

Lagally E. T., Mathies R. A., "Integrated genetic analysis Microsystems", *J. Phys. D: Appl. Phys.*, Vol. 37, R245-261, 2004.

Leamon, J. H., Lee, W. L., Tartaro, K. R., Lanza, J. R., Sarkis, G. J., deWinter, A. D., Berka, Jan, Lohman, K. L., "A massively parallel PicoLiterPlate based platform for discrete picoliter-scale polymerase chain reactions", *Electrophoresis*, Vol. 24, 3769-3777, 2003.

Liao, C. –S., Lee, G. B., Wu, J. J., Chang, C. C., Hsieh, T. M., Huang, F. C., Luo, C. H., "Micromachined polymerase chain reaction system for multiple DNA amplification of upper respiratory tract infectious diseases", *Biosensors and Bioelectronics*, Vol. 20, 1341-1348, 2005.

Lin, Y. C., Yang, C. C., Huang, M. Y., " Simulation and experimental validation of micro polymerase chain reaction chips", *Sensors and Actuators B*, Vol. 71, 127-133, 2000.

Liu, C. N., Toriello, N. M., Mathies, R. A., "Multichannel PCR-CE microdevice for genetic analysis", *Anal. Chem.*, Vol. 78, 5474-5479, 2006.

Liu, R. H., Yang, J., Lenigk, R., Bonanno J., Grodzinski, P., "Self-Contained, Fully Integrated Biochip for Sample Preparation, Polymerase Chain Reaction Amplification, and DNA Microarray Detection", *Analytical Chemistry*, Vol. 76, 1824-1831, 2004.

Liu, J., Hanson, C., Quake, S. R., "Solving the "World-to-chip" interface problem with a microfluidic matrix", *Anal. Chem*., Vol. 75, 4718-4723, 2003.

Iles, A., Fortt, R., Mello, A. J. d., " Thermal optimization of the Reimer-Tiemann reaction using thermochromic liquid crystals on a microfluidic reactor", *Lab on a Chip*, Vol. 5, 540-544, 2005.

Louie, M., Louie, L., Simor, A. E., "The role of DNA amplification technology in the diagnosis of infectious diseases", *Canadian Medical Association Journal*, Vol. 163, No. 3, 301-309, 2000.

Madou, M. J., "Fundamentals of Microfabrication and Nanotechnology, Third Edition: The Science of Miniaturization, Second Edition", CRC, 2009.

Marcus, J. S., Anderson, W. F., Quake, S. R., “Parallel picoliter RT-PCR assays using microfluidics”, *Anal. Chem*., Vol. 78, 956-958, 2006.

Martin, P. M., Matson, D. W., Bennett, W. D., Lin, Y., Hammerstrom, D. J., “Laminated plastic microfluidic components for biological and chemical systems”, *J. Vac. Sci. Technol. A.,* Vol. 17, No. 4, 2264-2269, 1999.

Matsubara, Y., Kerman, K., Kobayashi, M., Yamamura, S., Morita, Y., Tamiya, E., “Microchamber array based DNA quantification and specific sequence detection from a single copy via PCR in nanoliter volumes”, *Biosensors and Bioelectronics*, Vol. 20, 1482-1490, 2005.

Mecomber, J. S., Stalcup, A. M., Hurd, D., Halsall, H. B., Heineman, W. R., Seliskar, C. J., Wehmeyer, K. R., Limbach, P. A., “Analytical performance of polymer-based microfluidic devices fabricated by computer numerical controlled machining”, *Anal. Chem*., Vol. 78, 936-941, 2006.

Mecomber, J. S., Hurd, D., Limbach, P. A., ”Enhanced machining of micro-scale features in microchip molding masters by CNC milling”, *International Journal of machine tools & manufacture*, Vol. 45, 1542-1550, 2005.

Mitchell, M., “Design and microfabrication of a molded polymerase continuous flow polymerase chain reaction device”, *Master’s Thesis*, Louisiana State University, Baton Rouge, 2002.

Mitchell, M., Liu, X., W., Bejat, Y., Ford M.S., Nikitopoulos, D .E., Soper, S .A., Murphy, M. C., “Modeling and Validation of a Molded Polycarbonate Continuous Flow Polymerase Chain Reaction Device”, in *MicroFluidics, BioMEMS, and Medical Microsystems*, ed. H. Becker and P. Wolas, *Society of Photo-optical Instrumentation Engineers (SPIE)*, vol. 4982, p83-98, 2002.

Mohr, S., Zhang, Y. H., Macaskill, A., Day, P. J. R., Barber, R. W., Goddard, N. J., Emerson, D. R., Fielden, P. R., “Numerical and experimental study of a droplet-based PCR chip”, Microfluid Nanofluid, Vol. 3, 611-621, 2007.

Morens, D. M., Folkers, G. K., Fauci, A. S., “The challenge of emerging and re-emerging infectious diseases”, *Nature*, Vol. 430, No. 8, 242-249, 2004.

Morrison, T., Hurley, J., Garcia, J., Yoder, K., Katz, A., Roberts, D., Cho, J., Kanigan, T., Ilyin, S. E., Horowitz, D., Dixon, J. M., Brenan, C. J. H., “Nnaoliter high throughput quantitative PCR”, *Nucleic Acids Research*, Vol. 34, No. 18, 2006.

Nagai, H., Murakami, Y., Morita, Y., Yokoyama, K., Tamiya, E., “Development of a microchamber array for picoliter PCR”, *Anal. Chem*., Vol. 73, 1043-1047, 2001.

Nagai, H., Murakami, Y., Yokoyama, K., Tamiya, “High-throughput PCR in silicon based microchamber array”, *Biosensors & Bioelectronics*, Vol. 16, 1015-1019, 2001.

Nittis, V., Fortt, R., Legga, C. H., de Mello, A. J., “A high-pressure interconnector for chemical microsystem applications”, *Lab on a chip*, Vol. 1, 148-152, 2001.

Noh, J., Sung, S. W., Jeon, M. K., Kim, S. H., Lee, L. P., Woo, S. I., "In situ thermal diagnostics of the micro-PCR system using liquid crystals" *Sensors and Actuators A*, Vol. 122, 196-202, 2005.

Paegel, B. M., Emrich, C. A., Wedemayer, G. J., Scherer, J. R., Mathies, R. A., "High throughput DNA sequencing with a microfabricated 96-lane capillary array electroresis bioprocessor", *PNAS*, Vol. 99, No. 2, 574-579, 2002.

Park, D. S.-W., Hupert, M. L., Witek, M. A., You, B. H., Datta, P., Guy, J., Lee, J. B., Soper, S. A., Nikitopoulos, D. E., Murphy, M. C., "A titer-plate polymer microfluidic platform for high throughput nucleic acid purification", *Biomed. Microdevices*, Vol. 10, 21-33, 2008.

Park, D. S, Chen, P. C., You, B. H., Kim, N., Park, T., Datta, P., Desta, Y., Soper, S. A., D. E. Nikitopoulos, Murphy, M. C., "Optimization of the geometry for continuous flow PCR devices in a titer plate-based PCR multi-reactor platform", *2007 ASME International Mechanical Engineering Congress & Expo (IMECE)-42135*, Seattle, WA, 2007.

Park, D. S, Chen, P. C., You, B. H., Kim, N., Park, T., Lee, T. Y., Datta, P., Desta, Y., Soper, S. A., D. E. Nikitopoulos, Murphy, M. C., "Small footprint continuous flow PCR devices for a 96-well CFPCR multi-reactor platfrom", *2008 Hilton Head 0175*, Hilton Head Island, SC, 2008.

Prakash, A. R., Amrein, M., Kaler, K. V. I. S., "Characteristics and impact of Taq enzyme adsorption on surfaces in microfluidic devices", *Microfluid Nanofluid*, Vol. 4, No 4, 295-305, 2008.

Prakash, A. R., Adamia, S., Sieben, V., Pilarski, P., Pilarski, L. M., Backhouse, C. J., "Small volume PCR in PDMS biochips with integrated fluid control and vapour barrier", *Sensors and Actuators B*, Vol. 113, 398-409, 2006.

Panaro, N. J., Lou, X. J., Fortina, P., kricka, L. J., Wilding, P., "Surface effects on PCR reactions in multichip microfluidic platforms", *Biomed. Microdevices*, Vol. 6, No 1, 75-80, 2004.

Pattekar, A. V., Kothare, M. V., "Novel microfluidic interconnectors for high temperature and pressure applications", *J. Micromech. Microeng*., Vol. 13, 337-345, 2003.

Poon, L. L. M., Wong, O. K., Luk W., Yuen, K. Y., Peiris, J. S. M., Guan, Y, "Rapid diagnosis of a coronavirus associated with severe acute respiratory syndrome (SARS)", *Clinical Chemistry*, Vol. 49, No. 6, 953-955, 2003.

Puntambekar, A., Ahn, C. H., "Self-aligning microfluidic interconnects for glass- and plastic-based microfluidic systems", *J. Micromech. Microeng*., Vol. 12, 35-40, 2002.

Rani S. D., Soper S. A., Nikitopoulos D. E., Murphy M. C., "Simulation of Electroosmosis and Pressure Driven Flows In Microfluidic Interconnects", *2006 ASME International Mechanical Engineering Congress & Expo (IMECE)-15388, Chicago, IL, 2006.*

Robertson, B. H., Nicholson, K. A., "New microbiology tools for public health and their implications", *Annu. Rev. Public Health*, Vol. 26, 281-302, 2005.

Ross, D., Gaitan, M., Locascio, L. E., "Temperature measurement in microfluidic systems using a temperature-dependent fluorescent dye", *Anal. Chem.*, Vol. 73, 4117-4123, 2001.

Sadler, D. J., Changrani, R., Roberts, P., Chou, C. F., Zenhausern, F., "Thermal management of BioMEMS: Temperature control for ceramic-based PCR and DNA detection devices", *IEEE Transactions on Components and Packaging Technologies*, Vol. 26, No. 2, 309-316, 2003.

Secretariat Society for Biomolecular Screening (SBS), Microplate Standards Development Committee For MicroPlates- FootPrint Dimensions-ANSI/SBS 1-2004, eds., Danbury , CT, 2004.

Schaller, Th., Bohn, L., Mayer, J., Schubert, K., "Microstructure grooves with a width of less than 50 µm cut with ground hard metal micro end mills", *Precision Engineering*, Vol. 23, 229-235, 1999.

Scheer, H. C., Schulz, H., "A contribution to the flow behavior of thin polymer films during hot embossing lithography", *Microelectronic Engineering*, Vol. 56, 311-332, 2001.

Scheer, H. C., Schulz, H., Hoffmann, T., Sotomayor Torres, C. M., "Problems of the nanoimprinting technique for nanometer scale pattern definition", *J. Vac. Sci. Technol. B*, Vol. 16, No. 6, 3917-3921, 1998.

Schift, H., Heyderman, L. J., der Maur, M. A., Gobrecht, J., "Pattern formation in hot embossing of thin polymer films", *Nanotechnology*, Vol. 12, 173-177, 2001.

SE, C., Y., Carmeli, "The impact of antimicrobial resistance on health and economic outcomes", *Clin. Infect Dis*., Vol. 36, 1433-1437, 2003.

Shaikh, K. A., Ryu, K. S., Goluch, E. D., Nam, J. M., Liu, J., Thaxton, C. S., Chiesl, T. N., Barron, A. E., Lu, Y., Mirkin, C. A., Liu, C., "A modular microfluidic architecture for integrated biochemical analysis", *PNAS*, Vol. 102, No. 28, 9745-9750, 2005.

Shoffner, M. A., Cheng, J., Hvichia, G E., Kricka, L. J., Wilding, P., "Chip PCR. I. Surface passivation of microfabricated silicon-glass chips for PCR", *Nucleic Acids Research*, Vol. 24, No. 2, 375-379, 1996.

Slocum, A. H., Weber, A. C., "Precision passive mechanical alignment of wafers", *Journal of microelectromechanical systems*, Vol. 12, No. 6, 826-834, 2003.

Soc. Biomolecular Screening (SBS), *ANSI/SBS 1-2004*, SBS Microplate Stds Development Comm., Danbury, CT, 2004.

Song, Z., Choi, J., You, B. H., Lee, J., Park, S., "Simulation study on stress and deformation of polymeric patterns during the demolding process in thermal imprint lithography", *J. Vac. Sci. Technol. B*, Vol. 26, No. 2, 598-605, 2008.

Soper, S. A., Ford, S. M., Qi, S., McCarley, R. L., Kelly, K., Murphy, M. C., "Polymetric microelectromechanical systems", *Anal. Chem*., 643-651A, Oct. 2000.

Sotomayor Torres, C. M., "Alternative Lithography, Nanostructure Science and Technology", Kluwer Academic/Plenum Publishers, New York, 2003.

Sun, Y., Kwok, Y. C., "Polymeric microfluidic system for DNA analysis", *Analytica Chimica Acta*, Vol. 556, 80-96, 2006.

Taylor, T. B., Winn-Deen, E. S., Picozza, E., Woudenberg, T. M., Albin, M., "Optimization of the performance of the polymerase chain reaction in silicon-based microstructures", *Nucleic Acids Research*, Vol. 25, No 15, 3164-3168, 1997.

Toriello, N. M., Liu, C. N., Mathies, R. A., "Multichannel reverse transcription-polymerase chain reactrion microdevice for rapid gene expression and biomarker analysis", *Anal. Chem*., Vol. 78, 7997-8003, 2006.

Trinkle, C. A., Morgan, C. J., lee, L. P., "High precision assembly of soft-polymer microfluidic circuits", *2006 ASME International Mechanical Engineering Congress & Expo (IMECE)-14631, Chicago, IL,* 2006.

Unger, M. A., Chou, H. P., Thorsen, T., Scherer, A., Quake, S. R., "Monolithic microfabricated valves and pumps by multilayer soft lithography", *Science*, Vol. 288, 113-116, 2000.

http://genomics.energy.gov/

Wang, W., Wang, H. B., Li, Z. X., Guo, Z. Y., "Silicon inhibition effects on the polymerase chain reaction: A real time detection approach", *Journal of Biomedical Materials Research Part A*, Vol 77A, Issue 1, 28-34, 2005.

Wang, K., Gan, L., Boysen, C., Hood, L., "A microtiter plate-based high-throughput DNA purification method", *Analytical Biochemistry*, Vol. 226, 85-90, 1995.

Waters, L. C., Jacobson, S. C., Kroutchinina, N., Khandurina, J., Foote, R. S., Ramsey, J. M., "Multiple sample PCR amplification and electrophoretic analysis on a microchip", *Anal. Chem*., Vol. 70, 5172-5176, 1998.

Wei, C. W., Cheng, J. Y., Huang, C. T., Yen, M. H., Young, T. H., "Using a microfluidic device for 1 µl DNA microarray hybridization in 500 s", *Nucleic Acids Research*, Vol. 33, No. 8, e78, 2005.

Whitesides, G. M., Ostuni, E., Takayama, S., Jiang, X., Ingber, D. E., "Soft lithography in biology and biochemistry", *Annu. Rev. Biomed. Eng*., Vol. 3, 335-373, 2001.

Wittwer, C.T. Fillmore, G.C., and Garling, D.J. "Minimizing the time required for DNA amplification by efficient heat transfer to small samples," *Anal. Biochem.* , Vol. 186, no. 2, p. 328-331, 1990.

Witek, M. A., Hupert, M. L., Park, D. S.-W., Fears, K., Murphy, M. C., Soper, S. A., "96-well polycarbonate-based microfluidic titer plate for high throughput purification of DNA and RNA", *Anal. Chem.*, Vol. 80, No. 9, 3483-3491, 2008.

Worgull, M., Heckele, M., Schomburg, W. K., "Large-scale hot embossing", *Microsyst Technol*, Vol. 12, 110-115, 2005.

Wu, M. H., Huang, S. B., Cui, Z., Cui, Z., Lee, G. B., "A high throughput perfusion-based microbioreactor platform integrated with pneumatic micropumps for three-dimensional cell culture", *Biomed Microdevices*, Vol. 10, 309-319, 2008.

www.matrixtechcorp.com

www.ansys.com

www.intellisensesoftware.com

www.coventor.com

www.cfdrc.com

Yager, P., Edwards, T., Fu, E., Helton, K., Nelson, K., Tam, M., Weigi, B. H., "Microfluidic diagnostic technologies for global public health", *Nature*, Vol. 442, 412-418, 2006.

Yang, S., Rothman, R. E., "PCR-based diagnostics for infectious diseases: uses, limitations, and future applications in acute-care settings", *THE LANCET Infectious Diseases*, Vol. 4, 337-348, 2004.

Yang, M., Pal, R., Burns, M. A., "Cost-effective thermal isolation techniques for use on microfabricated DNA amplification and analysis devices", *J. Micromech. Microeng.*, Vol. 15, 221-230, 2005.

Yao, D., Virupaksha, V. L., Kim, B., "Study on squeezing flow during nonisothermal embossing of polymer microstructures", *Polymer Engineering And Science*, Vol. 45, 652-660, 2005.

Yoon, D. S., Lee, Y. S., Lee, Y., Cho, H. J., Sung, S. W., Oh, K. W., Cha, J., Lim, G., "Precise temperature control and rapid thermal cycling in a micromachined DNA polymerase chain reaction chip", *J. Micromech. Microeng.*, Vol. 12, 813-823, 2002.

You, B.-H., Chen, P.-C., Guy, J., Datta, P., Nikitopoulos, D. E., Soper, S. A., Murphy, M. C., "Passive alignment structures in modular, polymer microfluidic devices", *2006 ASME International Mechanical Engineering Congress & Expo (IMECE)-16100, Chicago, IL*, 2006.

You, B.-H., Chen, P.-C., Park, D. S., Park. S., Nikitopoulos, D. E., Soper, S. A., Murphy, M. C.," Microassembly of modular, polymer microfluidic devices using kinematic design and hot embossing", Journal of Micromechanics and Microengineering, in preparation.

Yu, X., Zhang, D., Li, T., Hao, L., Li, X., "3-D microarrays biochip for DNA amplification in polydimethylsiloxane (PDMS) elastomer", *Sensors and Actuators A*, Vol. 108, 103-107, 2003.

Zhang, Q., Wang, W., Zhang, H., Wang, Y., “Temperature analysis of continuous-flow micro-PCR based on FEA”, *Sensors and Actuators B*, Vol. 82, 75-81, 2002.

Zhang, J., das, C., Fan, Z. H., “Dynamic coating for protein separation in cyclic olefin copolymer microfluidic devices”, Microfluid Nanofluid, DOI 10.1007/s10404-007-0253-5, 2008.

Zou, Z. Q., Chen, X., Jin, Q. H., Yang, M. S., Zhao, J. L., “A novel miniaturized PCR multi-reactor array fabricated using flip-chip bonding techniques”, *J. Micromech. Microeng*., Vol. 15, 1476-1481, 2005.

Zou, Q., Miao, Y., Chen, Y., Sridhar, U., Chong, C. S., Chai, T., Tie, Y., Teh, C. H. L., Lim, T. M., Heng, C. K., “Micro-assembled multi-chamber thermal cycler for low-cost reaction chip thermal multiplexing”, *Sensors and Actuators A*, Vol. 102, 114-121, 2002.

APPENDIX A: MICROFABRICATION PROCESS FOR A POLYMER MICROFLUIDIC DEVICE

Polymers such as polycarbonate or PMMA were used as the substrates and this Appendix describes the fabrication process from a blank polymer substrate to a ready-to-use microfluidic device. The mold inserts were fabricated by micromilling machine (KERN MMP 2522, KERN Micro- und Feinwerktechnik GmbH & Co.KG, Germany) except the mold insert for the 96 well CFPCR array, which was using the UV-LIGA technique [Park et al., 2007, Park et al., 2008]. Hot embossing, thermal bonding, and capillary assembly were used after completing a mold insert to make the microfluidic device ready. A continuous flow polymerase chain reactor (CFPCR) microfluidic device was used as an example to illustrate each step of the fabrication process.

A.1 Polymer Microfluidic Device

Silicon and glass were two initial substrate materials in early Bio-MEMS application and the fabrication techniques were based on standard photolithography technology. The cost of silicon or glass microfabrication system drives the researchers and commercial companies to explore other novel and affordable materials. Disposable products are also in demand, especially in biomedical/medical field [Sun et al., 2006]. Wet etching, a standard method in silicon and glass manufacturing, is time-consuming and uses harmful solvent such as HF. The isotropic etching process can only fabricate shallow, low aspect ratio microchannels, with elliptical shape limits the geometry design [Becker et al., 2000]; silicon dry etching like reactive-ion etching (RIE) or deep reactive-ion etching (DRIE) can fabricate a high aspect ratio micro structure but it is costy, time-consuming, and not suitable for disposable medical device.

Polymers are promising materials for mass production via hot embossing or injection molding. They are bulk materials due to their long polymer chains and can be classified in three

different categories; thermoplastic polymers, elastomeric polymers, and thermoset polymers. Thermoplastic polymers can be pressed into specific shapes above the glass transition temperature, since the elevated temperature made the solid polymer behave as viscoelastic or a viscous flow [Becker et al., 2000]. Thermoplastic polymers like polycarbonate, polymethylmethacrylate (PMMA), cyclic olefin copolymer (COC) are popular polymer choices in Bio-MEMS.

An elastomeric polymer, Poly(dimethylsiloxane) (PDMS), is very attractive in the academic field due to its quick and simple fabrication process with nanometer resolution [Whitesides et al., 2001]. Its use has been demonstrated in micro devices [Beebe et al., 2000], micro valves [Liu et al, 2003], and micro pumps [Chou et al., 2001]. A research was carried out to study the performance of a microfluidic device affected by deformation of shallow PDMS microchannel due to its soft material property [Gervais et al., 2006]. A dimensionless parameter, taking the microchannel dimensions and material properties into account, was introduced to determine whether deformation was critical. Both simulation and experiment results indicated that deformed microchannel had a nonlinear pressure drop and had orders difference of magnitude in flow rate due to the deformed cross-section of the microchannel. This result was critical for specific applications which are sensitive to flow rate, flow profile, shear stress, and residence time. The authors suggested curing PDMS for longer times with more curing agent at higher temperature (120^{o}C) to obtain a higher modulus of elasticity PDMS micro device. Hybrid devices made of PDMS and glass enclosed small chambers for a micro-chamber PCR [Prakash et al., 2006]. Due to the high operating temperature of PCR, the cocktail in the enclosed chamber evaporated through the upper PDMS layer and made the performance of the PCR unreliable. A thin polyethylene film was inserted and located on the right top of the micro chamber during the

PDMS casting to prevent cocktail evaporation. A continuous flow PCR was fabricated by using a PDMS substrate and showed that the enzyme adsorption in a hydrophobic environment needed to be solved to demonstrate a successful PCR [Kim et al., 2006]. PDMS is a good choice for demonstrating concepts in a microfluidic device, and it is also a good candidate for use as a micro pump or micro valve because of its physical flexibility. To make PDMS a mainstream polymer in Bio-MEMS, more efforts are required to overcome its softness, vapour diffusion, enzyme adsorption, and difficult mass production when it was used as a substrate for microfluidic devices.

Some thermoplastic polymers are machinable to allow variety of shapes and sizes of microstructures, transparency to allow on-chip optical detection, acceptable thermal and electrical properties for Bio-MEMS applications, modifiable surface to suit individual requirement, lower annealing and bonding temperature requirements for microfabrication, and inexpensive mass production. In addition, a biocompatibility of polymers with many chemical or biochemical reagents is another critical advantage for becoming a mainstream material in Bio-MEMS. Background fluorescence of polymers is another potential drawback for optical applications in Bio-MEMS since it the background signal will increase the noise and lower the detection resolution [Sun et al., 2006, Soper et al., 2000, Boone et al., 2002].

Various microfabrication techniques for polymer substrates have been discussed and separated into three groups; replication, direct technique, and additional manufacturing technology [Becker et al., 2000, Becker et al., 2002]. The example of replication is LIGA (an acronym from the German words that mean lithography, electroplating, and molding). The designed patterns are fabricated on a mold insert and those patterns are transferred from mold master to thermoplastic polymers by using hot embossing and injection molding at a temperature

higher than the glass transition temperature. The direct techniques use laser-based technologies, optical lithography in deep resist, stereolithography, and layering techniques. Additional manufacturing technologies includes other fabrication processes such as bonding, gluing, and laser welding which assist previous two fabrication techniques, replication and direct technique.

Replication is the approach for mass production and mold inserts are required in this technique. Instead of using LIGA microfabrication for a mold insert, a micromilling machine (Kern MMP – Microtechnic, Murnau-Westried, Germany) was used to fabricate the mold insert on a brass substrate and the micromilled pattern on the brass mold insert was transferred into the polymer substrates by hot embossing.

A.2 Layout

The first step in fabricating a microfluidic device was to layout the design. Understanding the requirements, constraints, and fabrication process before drawing the chosen layouts using CAD software. Care had to be taken to understand the compatibility between the layout drawing and the fabrication equipment including the software and more detailed such as line type, output file, and line connections.

A micromilling machine is a convenient fabrication tool to make mold inserts on a brass substrate for replication. The required file type is the dxf file and the line type should be polyline. Any microstructures in the .dxf file should be an enclosed layout meaning the starting point is the ending point. The connection between microchannels and reservoirs should be a continuous polyline. A layout in a .dxf file only shows the 2-D layout so the thickness of each layer should be marked on your design either on a paper or in the dxf file. If a multilayer microstructures are required in the same file, each layer better uses different color to distinguish with each other, which also makes the communication between designer and operator clear. Figure 1 shows the

layout of the continuous flow polymerase chain reactor (CFPCR) in AutoCAD 2008 (AutoCad 2008, San Rafael, CA). Two colors are shown in Figure A.1, green identities the layout of the microchnanel and it is an enclosed loop; blue color shows the dummy structures surrounding the main micro structures to enhance the results of hot embossing and thermal bonding.

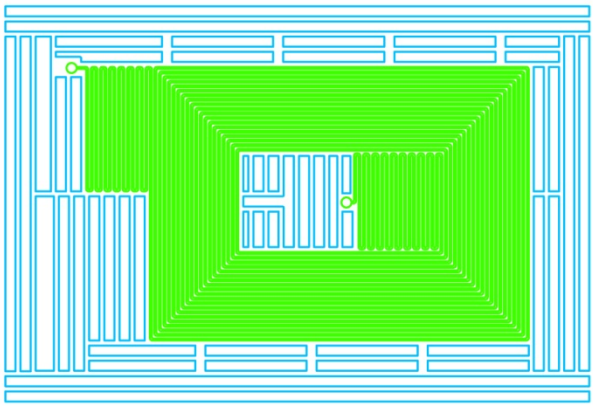

Figure A.1: The layout of a continuous flow polymerase chain reactor (CFPCR) in AutoCad (AutoCad 2008, San Rafael, CA).

A.3 Micromilling Machine for a Brass Mold Insert

A.3.1 Review

Replication is a good approach for medical devices due to its disposability and mold inserts are necessary components in this fabrication process. A LIGA mold insert is costy and time-consuming, and also its high resolution sometimes is not necessary for specific applications. Micro milling [Hupert et al., 2007, Hupert et al., 2005] or a conventional CNC machine have been developed as alternatives for metal mold master [Mecomber et al., 2005, Mecomber et al, 2006]. Using machining instead of photolithography for mold inserts can be time-effective, cost-effective, and competitive performance in certain applications. Furthermore using micromilling can easily pattern multi-layer micro structures or directly milled the micro structures on a polymer substrate.

A micromilling machine (KERN MMP 2522, KERN Micro- und Feinwerktechnik GmbH & Co.KG, Germany) was used to make a mold insert used for single sided hot embossing (Figure A.2) [Hupert et al., 2005, Hupert et al., 2007]. The micro milling bit was carried on a spindle at a maximum rpm of 40,000 and the resolution of position and repetition was ± 1μm. The substrate material was 0.25 " thick brass (Alloy 353 Engravers Brass, McMaster-Carr, Atlanta, GA) since the brass substrate had low tool wear and the strength was strong enough for hot embossing [Schaller et al., 1999]. A multi level micro structure could be easily done by using a micromilling but the disadvantages compared to a LIGA mold insert was the curvature in corners (Figure A.1 (b) and roughness (Figure A.1 (c)). The maximum average roughness of the side wall (Figure A.1 (c)) of the brass mold insert was measured to be 100 nm and larger than a reported roughness of 20 nm of a LIGA mold insert. To evaluate the performance difference between micromilled and LIGA mold inserts, electrophoresis flow (EOF) measurement and electrophoresis sample separation were realized for comparison. The results of EOF measurements did not show a significant difference between the two microfluidic devices and the measured values were $3.60\pm0.15 \times 10^{-4}$ $cm^2/ V s$ for embossed PMMA from a micromilled mold insert and $3.76\pm0.15 \times 10^{-4}$ cm^2/ V for embossed PMMA from a LIGA mold insert. From the electrophoresis separation experiment, three peaks corresponding to 105 bp, 341 bp, and 955 bp were shown in both microfluidic devices. The only difference was the plate number, the signal intensity, between the two microfluidic devices. They were 1.8×10^6/m from the device embossed from a LIGA mold insert and 1.3×10^6/m from the device embossed from a micro milled mold insert.

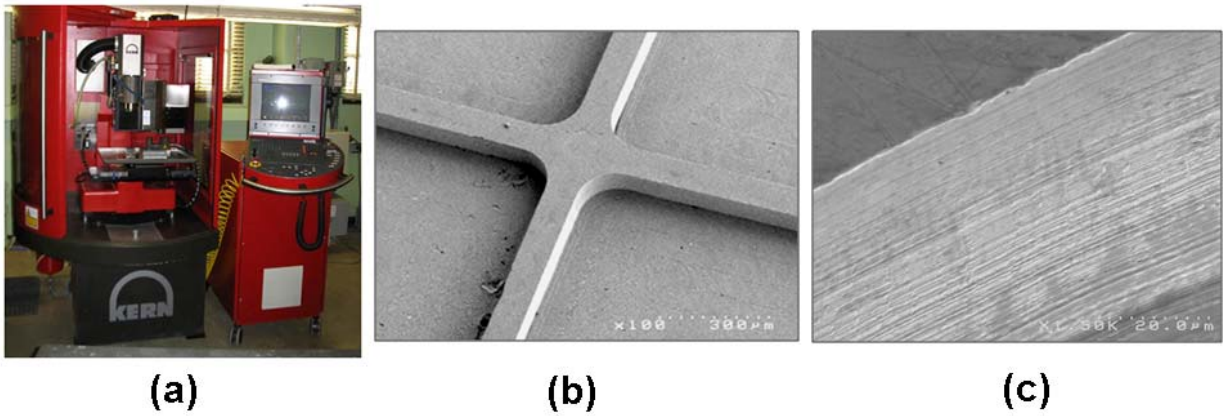

Figure A.2: (a) The micro milling machine in Center for Bio-Modular Multi-Scale systems (CBM^2) of Louisiana State University (b) The round corner from the curvature of the micro milled bit [Hupert et al., 2007] (c) The roughness and the machining pattern of a side wall on a micro milled mold insert [Hupert et al., 2007].

Another group used conventional CNC machine to fabricate three mold inserts for electrophoretic separation. The experimental results devices made from the three mold inserts were used to understand the separation resolution in terms of microchannel size and compare the separation performance to other commercial microfluidic devices. [Mecomber et al., 2005, Mecomber et al., 2006]. The substrate used was Type 7075 aluminum which had high hardness, high yield strength, low corrosion, and low surface roughness. The repetition and position resolution of the CNC machine was 25.4 μm with a variation of ±4 μm. Three mold inserts with different dimension microchannels were fabricated using a 51-μm-radus milling bit. Each had a T-junction microchannel for electrophoretic separation. The microfluidic device was fabricated by hot embossing PMMA substrates with the aluminum mold inserts. The smallest microchannel had the sharpest peak in the electropherogram compared to the two larger microchannels. Four commercial microchannels were used to compare the separation results with the results from the three micromilled mold inserts. (1) fabricated by wire-imprinting, (2) LIGA mold insert, (3) a commercial PMMA device, and (4) a commercial glass device. The separation performance of the smallest microchannel was better than the other three microchannels, wire-imprinted,

commercial PMMA microchannel, and commercial glass microchannel, and very close to the performance of LIGA hot embossed microchannel.

A.3.2 Micromilling Machine for a Mold Insert

Using micro milling machine is convenient and fast prototyping for a mold insert used for hot embossing or injection molding. The smallest diameter of the milling bit used in Center for BioModular Multi-Scale Systems is 50 μm but normally the milling bit used is either 100 μm or 200 μm, which means that the smallest distance between two microchannels is about 220 μm or 110 μm in practical design. After milling a brass mold insert, the mold insert is slightly polished on polishing papers to remove the burrs on the microstructures. Polishing can't be used on a mold insert with multi-layer structures, but hot embossing can be used to remove those burrs after several times hot embossing. The last step for preparing a mold insert for hot embossing is cleaning using isopropyl alcohol (IPA), deionized water (DI water), and air blowing. Figure A.3 shows the 4" brass mold insert for a CFPCR microfluidic device which is described in Figure A.1.

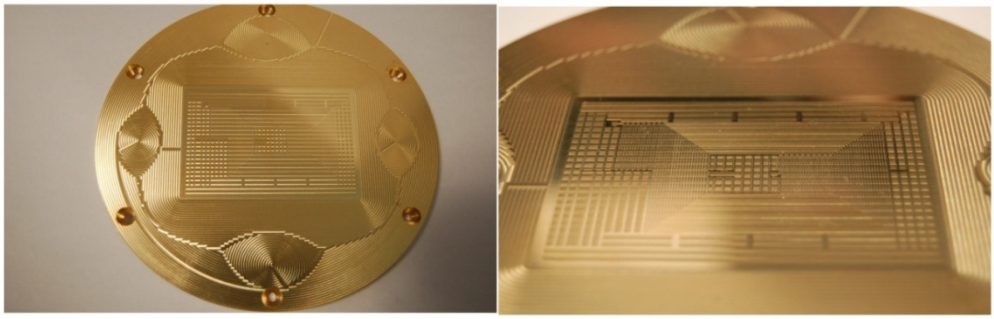

Figure A.3: (a) A micro milled mold insert on a brass substrate (b) A close view of the microstructures on a micro milled mold insert.

A.4 Hot embossing

Hot embossing, also called thermoforming, is a replication technique for mass production and its replication resolution can be as small as tens of nanometers [Scheer et al., 1998]. The

basic principle of hot embossing is to transfer the micro/nano patterns on a metal mold insert to a polymer substrate by heating the polymer above its glass transition temperature. The fundamental three steps in hot embossing process are embossing, cooling, and demolding. The basic parameters are the embossing temperature, the embossing pressure, the embossing time, and the demolding temperature.

In the embossing step, both the metal mold insert and polymer are initially heated to a temperature, which is above glass transition temperature, and pressure is applied to bring the metal mold insert and polymer in contact. At this stage, the surface of the polymer substrate is melted since the temperature was above the glass transition temperature. The polymer melt behaved as a viscoelastic or viscous fluid. The polymer flowed into the pattern of the mold insert and filled the cavities during the embossing stage at the embossing temperature. The temperature is decreased to the demolding temperature during the cooling stage and the applied pressure reduced as well. The final step was to pull the mold insert vertically away from the polymer, completing the hot embossed, pattern transfer from the mold insert to the polymer.

A.4.1 Review

Hot embossing has been studied since late 90s' or early 2000 and different groups focused on different perspectives such as hot embossing results on different geometries [Schift et al., 2001, Juang et al., 2002, Kricka et al., 2002, Heckele et al., 2004, Heckele et al., 2006], large format embossing [Worgull et al., 2005], and optimization of the embossing process [Heyderman et al., 2000, Scheer et al., 2001, Juang et al., 2002, Yao et al., 2005, Cameron et al., 2006, Guo et al., 2007, He et al., 2007, Zong et al., 2008].

Simulations were used to visualize the reasons behind the damage because the three steps of hot embossing including embossing, cooling, and demolding, with two numerical simulation

software packages, ANSYS and DEFORM-2D [He et al., 2007]. In the simulations of the embossing stage, two sets of micro geometries with opposite structures, one concave and the other convex, were modeled to understand the difference in polymer filling phenomena for these two geometries. The simulations showed that the concave geometry was more difficult to completely fill. Several concave microstructures were arranged from the center to the edge in the simulation of the substrate. The cavity closest to the center of the substrate had the highest rate of filling. In the cooling stage, there was residual stress due to the difference in thermal expansion of the metal and the polymer. This model used convex patterns as the microstructures in the mold insert and the results showed that the top corner of a convex microstructure had the highest stress and the highest chance of being damaged during the cooling process. The third model showed that during the demolding process, the embossed microstructure or the mold insert might be damaged due to the stress accumulated from the cooling stage, friction between the polymer and the mold insert, and the adhesion between the polymer and the mold insert. The bottom of the embossed parts had concentrated stresses and that failure might have higher chance of beginning from these points.

A model was carried out to study the cooling and demolding processes since most of the damage happening during the demolding process [Song et al., 2008]. Demolding is a process to overcome all levels of chemical (adhesion) and mechanical interactions (residual stress) between mold and substrate formed by the process history and properties of the materials involved. A simple numerical model including a silicon wafer mold and a PMMA substrate was used to understand the stress distribution based on different demolding rates, demolding angle, and the stamp aspect ratio. The demolding failure could happen both at the beginning and the end of the demolding process since the residual stress was concentrated at the corner of the initial

separation interface and at the final contact point between the stamp and the substrate right before the separation. A higher aspect ratio microstructure or misalignment between the stamp and substrate would increase the stress concentration followed by failure of the stamp or embossed parts.

Another hot embossing research was based on empirical observations [Cameron et al., 2006]. Different embossing temperatures, embossing times, and embossing forces were used. The demolding temperature was constant. The microstructure was embossed from a silicon wafer to a Zeonor 750R polymer plate. Different combinations of temperature, force, and time were used from 80ºC to 110ºC, 2 kN to 8 kN, and 1 minute to 4 minute. The replication results were investigated using a SEM. Good embossing was observed with 110ºC, 6 kN, and 3 minutes. To gain insight information about polymer behavior and the different temperature, dynamic mechanical thermal analysis (DMTA) was used. The DMTA experiments yielded storage moduli, loss moduli, and the loss tangent, all parameters that we present the hardness of the polymer. Above 72.2ºC, the glass transition temperature of a Zeonor 750R polymer, the storage modulus decreased as the loss modulus increased, and the loss tangent reached the peak at about 81ºC meaning the slope of the storage modulus was the most negative. The empirically determined embossing temperature was 110ºC which was 38 ºC higher than the glass transition temperature and the polymer behavior was purely viscous at that value from the DMTA data. A viscous polymer flow could minimize the residual stress built up inside the polymer, have the shortest relaxation time, and greater capability to completely fill the cavity. The conditions were validated from SEM images of the embossed structures.

Simulation was used to understand the filling phenomena in different size cavities and focus on the filling behavior based on the localized temperature distribution [Yao et al., 2005].

The stamp was assumed to be 200 ºC and the PMMA substrate was assumed to be at room temperature initially. Once the stamp and the PMMA substrate were brought together, heat transfer dominated the filling phenomena. Different cavity sizes from 6 μm to 200 μm with a fixed width/thickness ratio of 8:1 were modeled and the behavior of the flowing polymer was tracked at times from 0.1 s to 0.8 s. The first phenomena observed was the polymer flow behavior between the large and small cavities. In the 200 μm wide cavity, the polymer flowed along the stamp walls and reached to top surface of the stamp, then pushed the polymer toward the center of the cavity. But the flowing polymer in a 6 μm cavity filled the cavity from the center out instead of creeping along the wall. A 25 μm wide cavity showed a combination of filling phenomena, which had partial polymer flow along the stamp wall and partial polymer flow from the center. The temperature distribution in a 200 μm wide cavity was more nonuniform, a 80ºC variation from the edge to the center of the PMMA substrate, than a 6 μm wide cavity, which had less than 1 ºC variation, after 1 second of embossing. Since the large cavity had a larger distance to evenly distribute the heat from the stamp to the polymer, the local temperature dominated the behavior of the flowing polymer. A stamp was fabricated to validate the simulation result with 5 grooves with a fixed width/thickness ratio of 8:1, the widths were 25 μm, 50 μm, 100 μm, 200 μm, and 400 μm. The same patterns observed in the simulation were observed repeated experimentally, the large cavity, 200 μm wide, had polymer flow along the stamp wall while the small cavity, 25 μm wide, had more uniform filling from the center.

A.4.2 Hot Embossing

Hot embossing was done using the Hex 02 hot embossing machine (HEX-02, Jenoptik, Jena, Germany) in the Center for Advanced Microstructures and Devices (CAMD). Substrates were either polycarbonate or PMMA (McMaster, Robbinsville, NJ 08691). Different polymers

had different glass transition temperatures and hardness, so different embossing conditions were used to obtain good replication results. Several things should be considered to obtain good hot embossing results when the layout is still in the design stage. A negative microstructure, a recess like the hemispherical recess described in Chapter 4, is more difficult to emboss well compared to a positive microstructure, unless there is some dummy positive structure around it to increase the embossing pressure, or to reduce the polymer flow distance, to have more polymer flow into the recess. A thicker polymer substrate could deliver better replication results, especially for high aspect ratio structures since more polymer could flow during the hot embossing process [Scheer et al., 2001].

In the CFPCR layout, double-sided hot embossing was used to make thermal isolation grooves on the backside of the device to achieve the desired thermal performance. Double sided hot embossing used two mold inserts to sandwich a polymer substrate (Figure A.4 (a)). The two mold inserts had distinct microstructure patterns. Three pairs of alignment structures were added to both mold inserts for alignment during hot embossing (Figure A.4 (b) and Figure A.4 (c)). The alignment marks should have the same distance and orientation from the center of the mold insert because they are necessary for good alignment between the upper and lower mold inserts. The double0-sided hot embossing using the HEX 02 in CAMD was an empirical trial-and–error process, with the alignment between the upper and lower mold inserts based on manual adjustment of the jig holding the lower mold insert. The accuracy was between 50 μm to 100 μm. Figure A.5 shows the two mold inserts used to make CFPCR device. The upper mold insert was for the microfluidic channels and the lower mold insert was for the grooves on the backside of the device to achieve the desired thermal performance. A 2.3 mm thick polycarbonate (McMaster, Robbinsville, NJ 08691) was cut into a blank plate with a 6” square dimension. The

polycarbonate plate was put in the oven at 70ºC overnight to remove the residual water molecules before hot embossing. The upper mold insert in Figure A.5 was mounted to the upper jig of the HEX 02 embossing machine while the lower mold insert in Figure A.5 was screwed down on a lower jig. The polycarbonate was placed between the two mold inserts and embossed by heating up the both mold inserts and applying pressure. The alignment between the upper and lower mold insert was achieved by observing the alignment marks under a microscope to adjust the jig, which held the lower mold insert.

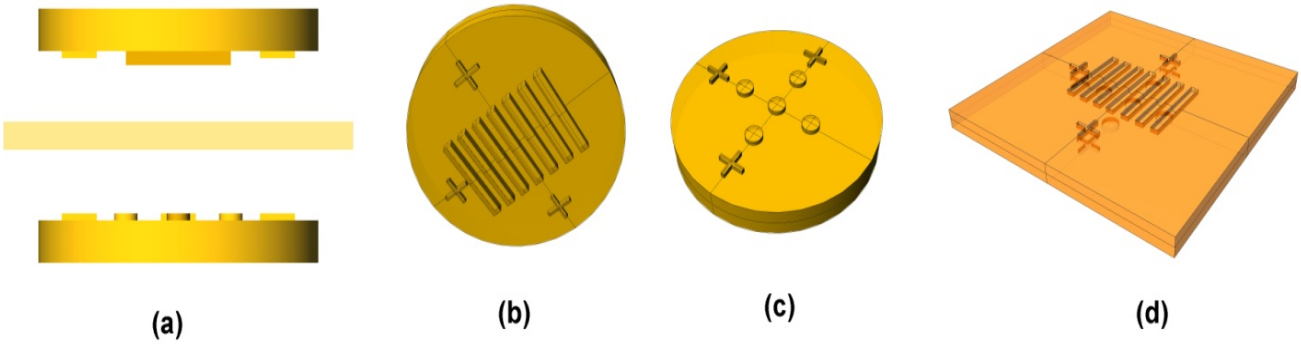

Figure A.4: (a) Double-sided hot embossing (b) Upper mold insert with three alignment structures (c) lower mold insert with three alignment structure (d) the hot embossed polymer device.

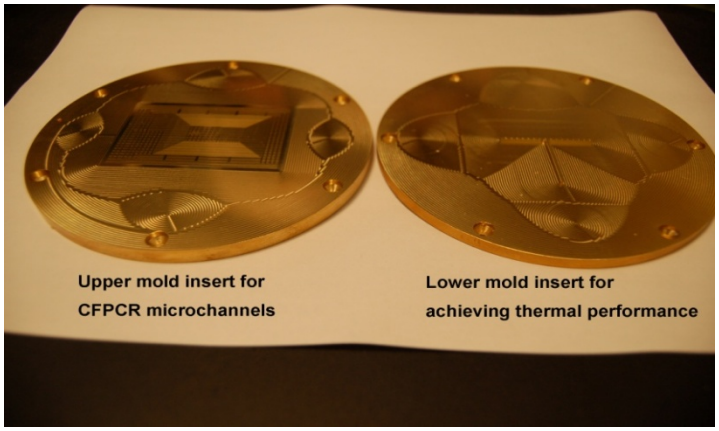

Figure A.5: Two mold inserts used to fabricate CFPCR device, the left one was for microfluidic microchannels and the right one was used to make grooves on the backside of the device to achieve the desired thermal performance.

A.5 Thermal Bonding

Thermal bonding, also called thermal fusion bonding, was used to enclose the microchannels on the surface of the hot embossed device. A thin cover sheet, the same material used for the embossed substrate, 0.25 mm thick, was used to cover the microchannel side of the substrate. Two pieces of borosilicate glass (McMaster, Robbinsville, NJ 08691) with a thickness tolerance of -0.002” to 0.014” from the manufacturer were used to sandwich the polymeric device and the cover sheet. Several paper clamps were used to hold the borosilicate glass, substrate, and cover sheet together and put in the conventional oven (Figure A.6). The temperature required for thermal bonding was a little above the glass transition temperature, which made the surface of the substrate and cover sheet melt and bond together.

Before thermal bonding, holes for reservoirs were drilled by using a drill press [MicroLux, MicroMark, NJ]. Figure A.6 (a) shows the components used for the thermal bonding of a CFPCR microfluidic device, which included two borosilicate glasses, 4 paper clamps, a 0.25 mm thick cover sheet, and a 2.3 mm thick CFPCR device. Figure A.6 (b) shows the polymer device and the polymer sheet sandwiched by two borosilicate glasses and two paper clamps and Figure A.6 (c) shows the assembly after combining every component together. The temperature used for CFPCR device was 164ºC for 20 minutes. Figure A.7 shows the cross-sectional view of the microchannels after thermal bonding, the line in Figure A.7 (b) indicates the boundary between a cover sheet and the substrate.

A.6 Capillary Assembly

After thermal bonding, capillaries or tubing were inserted into the reservoirs by applying epoxy (5 minute Epoxy, ITWDevcon, Danvers, MA) on the connection spot. Commercial connectors sometimes did not fit the specification for the microfluidic device and most of the

them are expensive. A home-made epoxy connector was a good solution for different sizes of the reservoir and the capillary without worrying about the contamination to the samples. Figure A.8 shows the ready-to-use CFPCR device after capillary assembly, which had two PEEK tubes (1577-12X, Upchurch Scientific, Oak Harbor, WA) connected to the inlet and the outlet by epoxy.

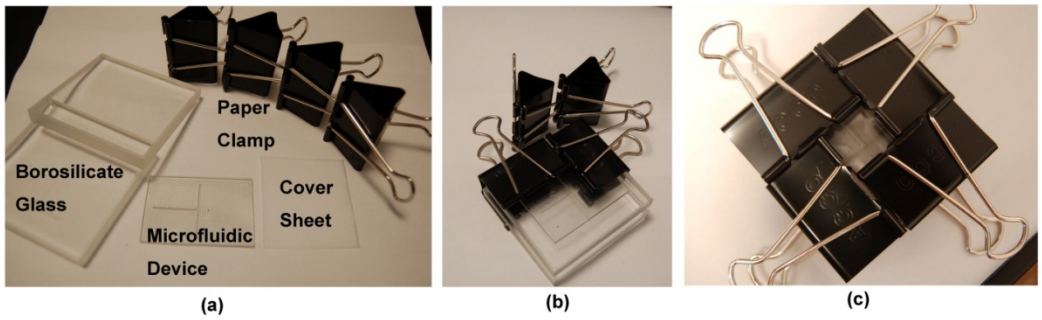

Figure A.6: (a) The components for thermal bonding, 2 borosilicate glasses, polymeric device, a polymer cover sheet, and 4 paper clamps (b) The polymeric device and the polymer cover sheet were sandwiched by two borosilicate glasses and paper clamps (d) After assembly.

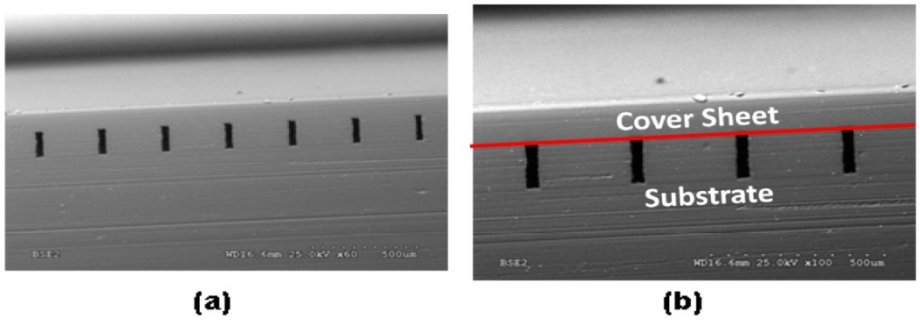

Figure A.7: (a) Cross-sectional view of the enclosed microchannels after thermal bonding (b) A close-up view of the microchannels after thermal bonding.

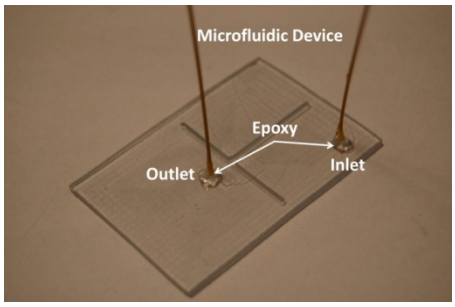

Figure A.8: Two capillaries were inserted and glued to the two reservoirs as inlet and outlet.

APPENDIX B: A HEMISPHERICAL RECESS WITH A CONCAVE ANNULAR RING

In Chapter 4, a passive alignment structure to achieve good alignment between two microfluidic plates was described. The original passive alignment structure had a mismatch of 28 µm-75 µm between the two plates. The mismatch was attributed to the incomplete filling of the polymer in the post patterns leading to shorter hemispherical posts. This shorter hemisphere-tipped post degraded the accuracy of the alignment between the two plates and required correction.

A convex annular ring was added to shorten the flow distance to the holes for the melted polymer and made the complete filling with the polymer easier. Estimates based on Equation 4.1 and 4.2 gave a 20 times faster fill time to completely fill the recess with a convex annular structure than the original hemispherical recess. To further understand the influence of the annular ring on the filling of the recesses, a concave annular ring was also fabricated and is shown in Figure B.1 (a). Figure B.1 (b) shows the embossed hemisphere-tipped post from this mold insert.

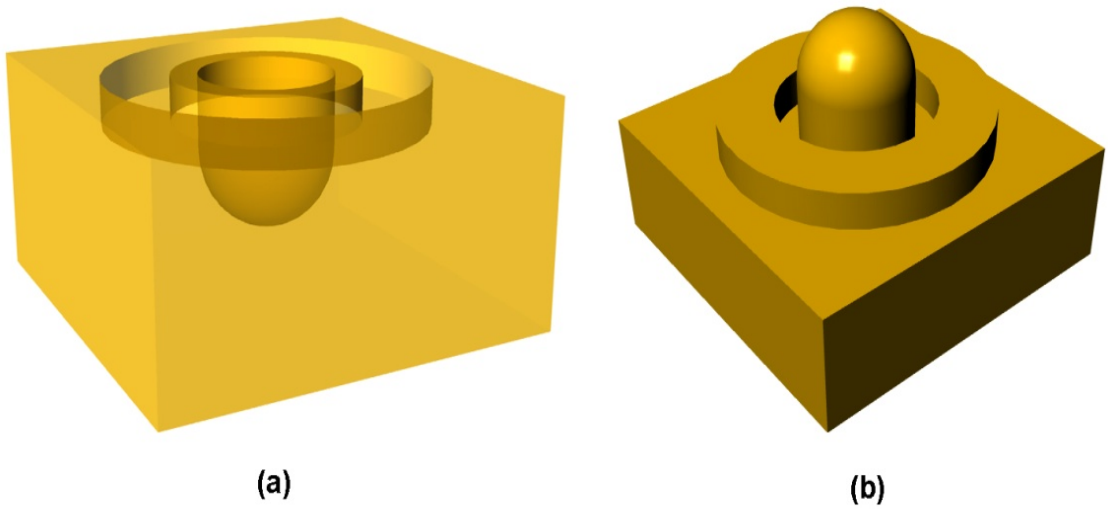

Figure B.1: (a) The hemisphere-tipped recess with a concave annular ring on a mold insert (b) a polycarbonate hemisphere-tipped post with an annular ring.

B.1 Estimated Time to Completely Fill the Recess With a Concave Annular Ring

Equations 4.1 and 4.2 described in Section 4.5.1 were simple tools for estimating the time to completely fill a recess. The estimated time could also be taken as an index to determine the difficulty of hot embossing a specific layout. Figure B.2 shows the cross-sectional view of the recess with a concave annular ring on a mold insert which was the opposite of hemispherical recess with a convex annular ring shown in Figure 4.6 (b). The diameter of the mold cavity was 100 mm, the width of the center recess in Figure B.2 was 1 mm with a depth of 1 mm, and the width of the annular ring in Figure B.2 was 1 mm with a depth of 0.5 mm. Since the diameter of the mold insert was much larger than the width of those recesses in Figure B.2, the polymer filling phenomena began from the outer recesses, the concave annular ring, and progressed to the center recess [Heyderman et al., 2000]. The time required to fill the three recesses in Figure B.2 would be a superposition of the time to fill the outermost recess and the time to fill the center recess. From Equation 4.2, the final thickness of the polymer was 4.989 mm from a initial thickness of 5 mm after filling the outermost recess and the required time was 1.819×10^{-4} seconds. The estimate was based on the assumed pressure, 3×10^{6} Pa, the assumed viscosity, 2648 Pa.s, and the flow distance of the polymer, 48.4 mm from the edge to the center of the outer recesses. After filling the outer recess, the polymer continued until the center recess was filled. The final thickness of the polymer was 4.968 mm based on Equation 4.2. The time required to fill the center recess was 3.709×10^{-4} seconds with a flow distance of 49.5 mm from the edge to the center of the center recess. The total time to fill the three recesses shown in Figure B.2 was 5.528×10^{-4} seconds which was longer than for the single recess case in Chapter 4. This implied that a hemispherical recess with a concave annular ring was more difficult to completely fill. Compared to these two cases, the original hemispherical recess and the hemispherical recess with

a concave annular ring, the initial contact surface, or initial contact level, of both cases is the same. Neither had the convex structure like Figure 4.6 (b) to reduce the polymer flow distance followed by a longer filling time from Equation 4.1. The hemispherical recess with a concave annular ring had more recesses to be filled in sequence which made the complete filling phenomena longer, or more difficult.

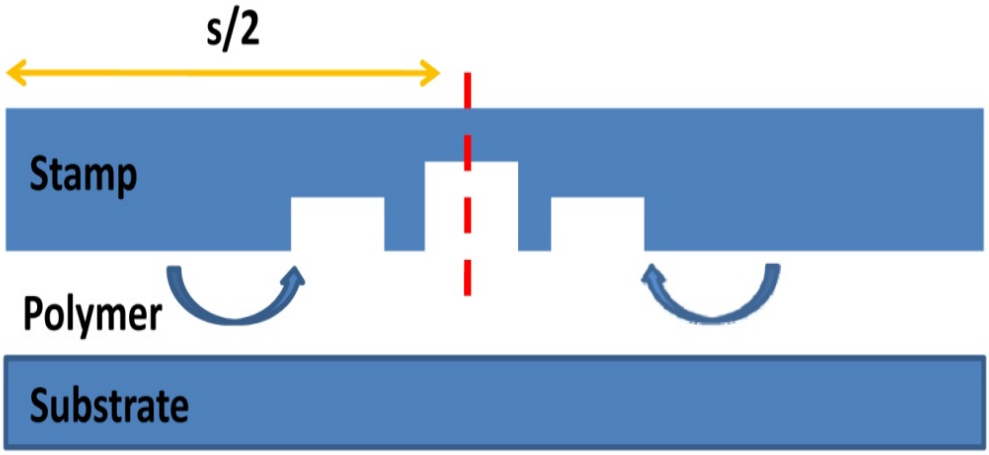

Figure B.2: The cross sectional view of the recess with a concave annular structure.

B.2: Comparison between the Original Hemispherical Recess and the Hemispherical Recess with a Concave Annular Ring

To validate the conclusions drawn from Equations 4.1 and 4.2 for a hemispherical recess with a concave annular structure, a mold insert was designed, as shown in Figure B.3 (a). The layout of the hemispherical recesses was the same as the layout used in Figure 4.6 (a), but the difference was the concave annular ring was used herein instead of convex annular ring. The original hemispherical recess in both cases was used as a reference to compare the embossing results between a hemispherical recess with a convex annular ring and a hemispherical recess with a concave annular ring.

The six layouts in Figure B.3 (a) included one original hemispherical recess design and five different hemispherical recesses, in order to assess the impact of the annular structures on post fabrication compared to the original design. Five alternative modified post designs incorporating different distances (100 µm, 200 µm, 300 µm, 400 µm, and 500 µm) between the inner walls of the concave annular structure and the edge of the hemispherical structures, shown in the area with the red color in Figure B.3 (b). Microstructures were located at three radial distances (12 mm, 24 mm, and 36 mm) to help evaluate whether the distance from the center affected polymer filling.

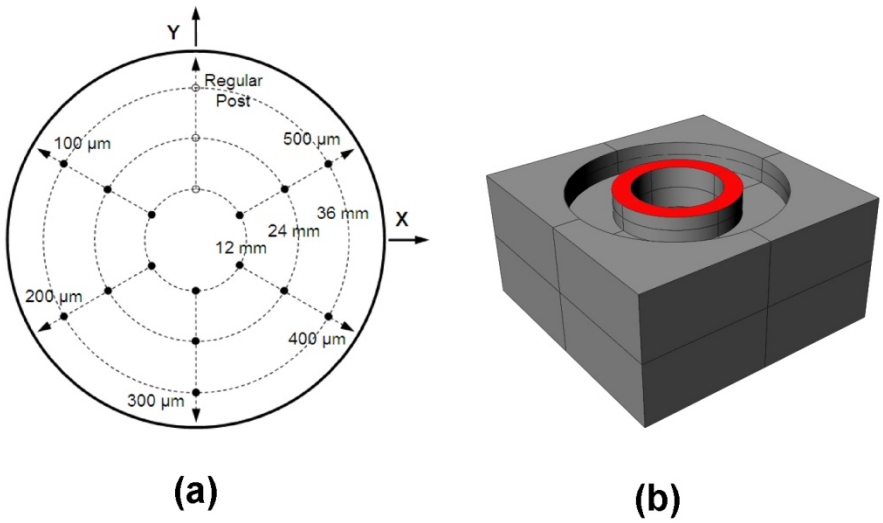

Figure B.3: (a) The layout of the mold insert with 6 different columns of recesses including one original hemispherical recess and five hemispherical recesses with concave annular structures (b) The configuration of the hemispherical recess with a concave annular structure; the area with red color was the gap distance between the hemispherical recess and annular ring.

Table B.1 listed the hot embossing conditions for the hemispherical post with the concave annular rings shown in Figure B.3 (a). The polymer filling of the hemispherical recess was evaluated by measuring the heights of the embossed posts using a Measurescope (MM-22, Nikon Corp., Kawasaki, Japan). Height was measured by focusing alternately on the top of the posts and the substrate surface. Ten samples were used to compare the different layouts.

Table B.1: The hot embossing conditions used for the hemisphere-tipped post.

	Molding Temp (°C)	**Embossing Force (kN)**	**Holding Time (s)**	**Demolding Temp (°C)**	**Embossing Velocity (mm/min)**
Post	190	24	120	140	0.5

Table B.2 shows the average height and standard deviation of the original hemisphere-tipped posts and hemispherical posts with concave annular rings. The measurement results show that the hemisphere-tipped posts with concave annular rings did not improve filling compared to the original design. From the overall average height of the hemispherical posts shown in Figure B.4, except for the hemispherical posts with a 100 μm gap which had similar measurement results, other hemispherical posts were all shorter than the original posts. The average heights of those hemisphere-tipped posts with different gap distance from 0, 100 μm, 200 μm, 300 μm, 400 μm, and 500 μm, were 874.7 μm, 876.8 μm, 870 μm, 865.5 μm, 857.4 μm, and 869.2 μm, and corresponded to 10.4 μm, 13.2 μm, 10.1 μm, 9.1 μm, 9.2 μm, and 7.6 μm in standard deviation (STD).

The measurement results show that the concave annular ring did not improve filling. The results validated the calculations, which indicated longer filling times with the addition of the concave annular rings compared to the original hemispherical recess. Compared to the polymer filling results of the hemispherical posts with convex annular ring described in Section 4.5.2, the results showed that convex structures could significantly improve filling than the concave structures for a recess micro-pattern. A shorter distance between the initial contact surface and the recess dramatically shortened the required time to completely fill the recess from the Equation 4.1 and 4.2 ($t_f \propto s^2$).

Table B.2: The average height and standard deviation (STD) of the hemisphere-tipped posts in terms of either the distance from the center of the substrate. The press diameter was 100 mm and the diameter of the hemispherical recess was 1 mm.

	Original		100		200		300		400		500	
	Ave.	STD	Ave.	STD	Ave.	STD	Ave.	STD	Ave.	STD	Ave.	STD
12	863.8	8.8	863.4	10.7	870.8	11.1	871.1	4.3	871	2.7	864.7	8.7
24	875.8	4.1	877.4	4.9	863.5	8.6	861.7	11.4	847.7	11.4	866.7	3.2
36	884.4	4.3	889.4	6.9	875.2	8.2	863.7	7	853.4	4.7	876.4	3.7

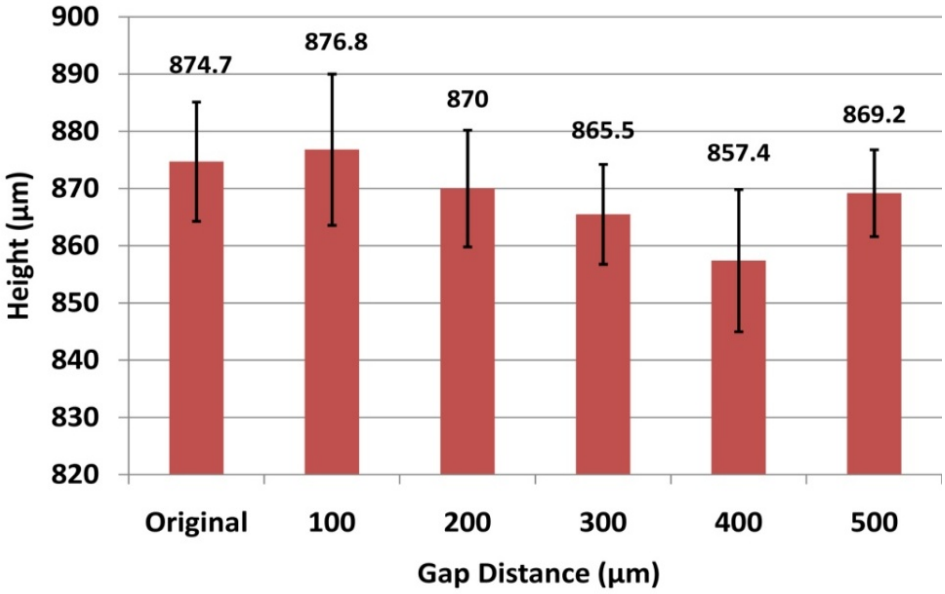

Figure B.4: The overall mean heights and the standard deviations of the original post and the modified posts with gaps from 100 µm to 500 µm.

VITA

Pin-Chuan Chen was born in March, 1978, in Taipei, Taiwan, to Hsien-Chin Chen and Ling-Ling Liao. He attended National Cheng-Kung University, Tainan, Taiwan, for his undergraduate education. He graduated with a bachelor of science degree, in mechanical engineering in May of 2000.

In 2002, he left for the United States where he entered the mechanical engineering department at Louisiana State University in Baton Rouge, Louisiana, to pursue graduate studies. He joined the mechanical engineering department and began working on microfluidic project after the first semester. He received the degree of Master of Science in Mechanical Engineering in May, 2006 and continued his doctoral program in mechanical engineering department at Louisiana State University. During his doctoral program study, his research focused on a high throughput microfluidic system in modular approach against acute infectious diseases, and he won the outstanding research assistant award in the academic year of 2007-2008 under his major advisor, Dr. Michael C. Murphy. He will receive his degree of Doctor of Philosophy in May, 2009 and work as an Assistant Research Scientist in Singapore Institute of Manufacturing Technology (SIMTech) from June, 2009.